2020

Parameter optimisation of coaxial Melt Electrowriting

Anne-Katrin Gruska

UNIVERSITY OF WOLLONGONG AUSTRALIA

Parameter optimisation of coaxial Melt Electrowriting

Anne-Katrin Gruska

Principal Supervisor: A/Prof. Stephen Beirne

Co-Supervisor: Prof. Gordon G. Wallace

External Supervisor: Prof. Paul D. Dalton

This thesis is presented as part of the requirement for the conferral of the degree:

Master of Philosophy (Biofabrication)

The University of Wollongong

Australian Institute of Innovative Materials (AIIM)

Intelligent Polymer Research Institute (IPRI)

August 2020

Certification

I, Anne-Katrin Gruska, declare that this thesis submitted in fulfilment of the requirements for the conferral of the degree Master of Philosophy, from the University of Wollongong, is wholly my own work unless otherwise referenced or acknowledged. This document has not been submitted for qualifications at any other academic institution.

Anne-Katrin Gruska

31st of August 2020

Biofabrication Master's Double Degree Statement

This section shall serve to clarify the organisation and structure within the Double Degree Masters of Biofabrication.

Appended to this document is an additional annex that represents the entirety of a six month project (Master's Thesis) undertaken at the Julius-Maximilians-Universität Würzburg (Germany) and submitted as part of the fulfilment of the Double Degree Masters of Biofabrication between the University of Wollongong (Australia) and the Julius-Maximilians-Universität Würzburg (Germany).

According to the Memorandum of Agreement between Queensland University of Technology, University of Wollongong, Julius-Maximilians-Universität Würzburg and Utrecht University, the Biofabcrication Double Degree program was started.

Students in the program will be expected to obtain a Master's degree from one European and one Australian institution. The student initiates the Biofabrication Mobility Program in a Master's degree at the home institution for two semesters (60 ECTS in Europe), as well as taking up enrolment in another Master's degree at the Australian participating institution, herein after referred to host institution for a period of ten months (60 ECTS in Europe).

More specifically, students enrolled in Würzburg as home institution undertook one semester (6 months) of studies. These studies comprised four compulsory and two elective courses (total of 30 ECTS), detailed hereinafter:

- Biofabrication
- Fundamentals of Tissue Engineering and Quality Management
- Physical Chemistry of Supramolecular Assemblies
- Polymers 2
- Organic Chemistry of Supramolecular Assemblies
- Polymer Materials 1: Technology of Polymer Modification

Students enrolled at the overseas participating institution during second and third semester for a 10-month internship, undertaking a research project documented in this thesis submitted to the University of Wollongong (60 ECTS).

At last, a Master's Thesis was written about research carried out at the Julius-Maximilians-Universität Würzburg during the final semester (30 ECTS), appended to this document and submitted to the University of Würzburg to fulfil the requirements for the home Master's Degree in Biofabrication.

Acknowledgements

First of all, I would like to thank my supervisory team: Prof. Gordon G. Wallace who welcomed me into IPRI and his research team, and offered many possibilities such as workshops that allowed me to learn and think outside the box, as well as A/Prof. Stephen Beirne who always encouraged me and raised me into becoming an independent researcher, preparing me for whatever the future holds. Also, I would like to thank Prof. Paul Dalton who gave me the chance to become part of this Master's degree and supported me during my time in Australia with his knowledge and positive attitude.

A special thanks goes to Philipp Stahlhut who took the SEM image of one of my fibres, which can be found at the end of this thesis. Thank you for helping me prove something remarkable!

I want to thank the staff and students working at IPRI as well. It has been a delight meeting all of you and having scientific and not-so-scientific discussions with you. Especially, I would like to thank Fleurine: I'm in awe of the work that you've done and glad that I chose to take over your project, resulting in me becoming part of the MEW world and us becoming close friends. Thank you for being amazing! Furthermore, a big thank you to Cormac, Zhilian, Alex, Ben, Brodie and Rhys who helped me with technical challenges and changed my way of thinking.

Finally, I would like to thank my family who supported me in all my decisions.

Abstract

Melt electrowriting (MEW) is an additive manufacturing technique that combines the advantages of both, solution electrospinning and fused filament fabrication by allowing the deposition of ultra-fine fibres in a controlled way without the necessity for dispersion of the material being prepared in toxic solvents. This approach is promising for the research field of tissue engineering that requires not only different types of materials but also different manufacturing techniques for scaffolds that are supposed to provide robust but flexible support, which facilitates cell growth without causing damage to the surrounding tissue.

Recent advances in MEW technology (Mar 2018) that allow the processing through coaxial extrusion geometries are examined in the context of composite materials and their possible application as for example drug delivery systems. In this study, poly(ε-caprolactone) (PCL) containing different percentages of different fluorophores was prepared using a precipitation process. The resulting composites were printed uniaxially as a means to investigate the effects of the added salts and the emerging additional charges on the jet. It was shown that the acceleration of the jet was increased with an increasing fluorophore loading, which could be seen in the resulting critical translation speeds.

The uniaxial investigation was also important to validate the thermal stabilities for the dyes, which were used in the coaxial process. For the latter, DiOC18 and Rhodamine B were chosen because of their stability as well as their compatibility with PCL and each other. The feasibility of core-shell structures was examined by varying process and material parameters. Amongst other things, the green and red dyed polymers were processed through the inner and the outer syringe in order to get a clear distinction between the core and the shell. While these structures were observed occasionally using confocal laser scanning microscopy, they were found to be unstable due to diffusion and mixing at the Taylor cone during the MEW process. The in-process-mixing of the materials can be of interest for the application-specific compounding of heat- and strain-sensitive polymers while having control over their composition depending on the chosen flow rates. Janus fibres were also shown possible through adjustment of the axial location of the core syringe used, although mixing of the polymer prior to solidification affected this effect. Nevertheless, MEW is a technique with a vast amount of possible parameter combinations. Hence, the production of core-shell and Janus fibres is shown possible and offers a variety of applications such as in microelectromechanical and drug delivery systems as well as robotics. When applying air through the core syringe, the insertion of air into the melt leading to hollow channels in the fibres was shown feasible and reproducible. This technique offers the printing of fibres with outer diameters as big as 90 µm while containing a 25 µm cavity, as well as fibres with an outer and inner diameter of 10 and 2 µm, respectively. While the production of hollow fibres usually demands for a fabrication of core-shell structures first with a later dissolving of the core material, the coaxial MEW of hollow fibres is a one-step approach that works without toxic solvents. Furthermore, it enables the fabrication of structures that are known to be lighter while having improved mechanical properties compared to dense materials, hence offering a wide spectrum of applications such as in regenerative medicine and microfluidics.

Table of Contents

List of Figures

List of Tables

List of Abbreviations

3D	Three-Dimensional
c	Concentration
cc	Cubic centimetres
CSF-1	Colony Stimulating Factor 1
CTS	Critical Translation Speed
DiI	1,1'-dioctadecyl-3,3,3',3'-tetramethylindocarbocyanine perchlorate
DiOC18	3,3'-dioctadecyclocacarbocyanine perchlorate
ECM	Extracellular Matrix
EFG	Edge-Functionalised Graphene
EFG-PCL	PCL containing 1 wt% EFG
ES	Electrospinning
FBGC	Foreign Body Giant Cell
FFF	Fused Filament Fabrication
FGM	Functionally Graded Material
FGP	Functionally Graded Porosity
G	Birmingham gauge
h	Hour
HV	High Voltage
kDa	Kilodalton
kPa	Kilopascal
m	Mass
mbar	Millibar
MES	Melt Electrospinning
MEW	Melt Electrowriting
mm	Millimetre
ms	Millisecond
MSC	Mesenchymal Stem Cells
min	Minute

mL	Millilitre
MW	Molecular Weight
µL	Microlitre
µm	Micrometre
NFES	Near-Field Electrospinning
nm	Nanometre
p	Pressure
pA	Picoampere
p_C	Core pressure
PCL	Poly(ε-caprolactone)
PEEK	Polyetheretherketone
PP	Polypropylene
p_S	Shell pressure
s	Second
s_c	Collector speed
s_j	Jet speed
SEM	Scanning Electron Microscopy
SES	Solution Electrospinning
Ti6Al4V	Titanium alloy containing 6 wt% aluminium and 4 wt% vanadium
V	Volt
V_C	Critical voltage
VEGF-A	Vascular Endothelial Growth Factor A
W	Watt
wt%	Weight percent
°C	Degree Celsius

1. Introduction

Three-dimensional (3D) printing techniques have been gaining great attention in recent history by offering new perspectives for tissue engineering. Tissue engineering is a research field that aims to replace or repair tissue functions for the treatment of diseases or injuries by artificially recreating said tissues. For this approach, scaffolds that act as a template for the tissue formation are combined with bioactive molecules and cells [1]. These structures can be produced in different ways, for example via 3D printing that offers the accessibility of complex, tailor-made structures [2]. Melt electrowriting (MEW) is a 3D printing technique that was first described in 2011 by Brown *et al.* and is based on the effects of electrospinning, leading to well-defined fibres in the low micrometre range [3]. The following literature review will provide background knowledge to describe how MEW differs from other fibre manufacturing techniques by analysing its basic principles, as well as the requirements for the materials used in the scaffold production, and the types of geometries that are accessible from coaxial extrusion processes since the latter will be investigated in the present study for MEW.

1.1 3D printing in tissue engineering

Tissue engineering is a scientific field that uses multidisciplinary approaches to develop constructs that restore, maintain or improve tissue functions for regenerative medicine [1]. For this purpose, typically a combination, as seen in Figure 1, of biomaterial scaffolds, cells and bioactive molecules are used in order to stimulate tissue formation and incorporation within the surrounding tissue [1].

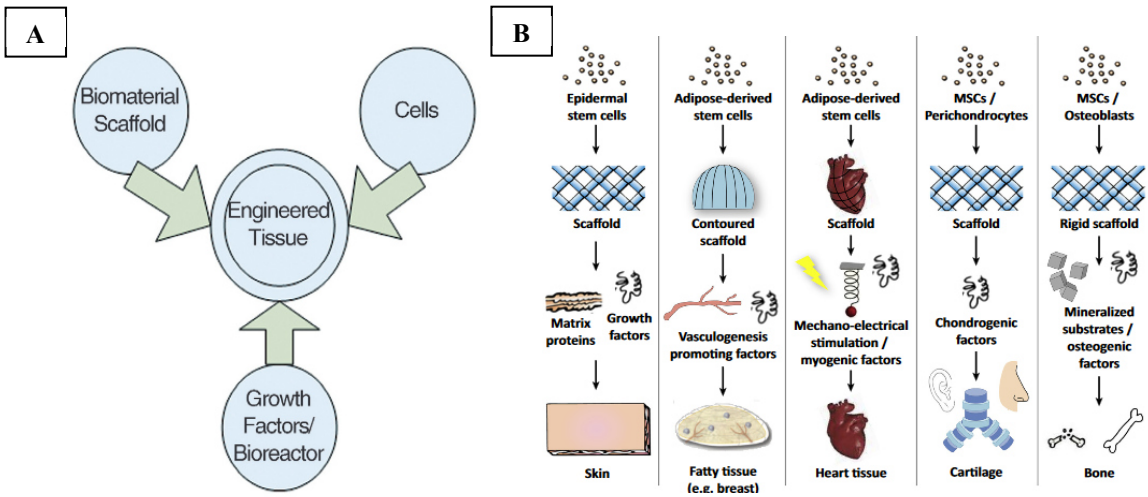

Figure 1: *Tissue engineering triad of cells, growth factors/ bioreactor (chemically/ physically provided signals) and scaffold (A) and examples of such combinations resulting in different tissue types (B). Figure A and B reproduced from [4] and [5], respectively.*

Scaffolds act as a template for tissue formation; they are 3D structures with the purpose of supporting cell migration, proliferation and differentiation [6]. They can be manufactured in different ways, for example through additive manufacturing, often referred to as 3D printing.

Additive manufacturing is the fabrication of objects by converting a digital 3D design into a physical object in a 'layer-by-layer' approach [7, 8]. There is an ever-expanding range of additive manufacturing technologies, each being categorised by the respective processing technique and the raw materials being used. There are solid-, powder- and liquid-based techniques [9]; Fused filament fabrication (FFF), one of the most widely employed additive fabrication approaches, is part of the solid-based techniques: A solid thermoplastic polymer filament is heated until molten, extruded through a nozzle and deposited in successive thin layers [10, 11]. The resolution of fibres obtained by FFF is limited due to the Barus effect, which is the phenomenon where the polymer melt swells when leaving a die after being compressed [12]. This results typically in fibre dimensions in the range of 100 to 300 µm [13, 14].

Scaffolds containing ultra-fine fibres in the sub-micrometre range provide excellent properties such as large surface-to-volume ratios [15] that are known to promote cell adhesion, proliferation, migration, and differentiation [16] and can be attained by many different fabrication methods like for example solution electrospinning (SES) [17, 18] self-assembly [19] and phase separation [20]. Nevertheless, these methods result in chaotic and/or uncontrollable structures that can act as a barrier to cell infiltration due to low pore sizes. It was found by Pham *et al.* that for randomly deposited solution electrospun meshes, for a promotion of cell invasion and growth the fibre diameter must be at least 4 µm to obtain a pore size of at least 20 µm [3, 21]. Additive manufacturing techniques provide more ordered control over the resulting pore sizes through precise deposition and regular stacking of materials as can be seen in Figure 2 by comparing the irregularity of the electrospun structure in Figure 2 A to the repeatable layered, but comparatively large structures prepared through FFF in Figure 2 B and the finely ordered micron-scale melt electrowritten structure (MEW) in Figure 2 C.

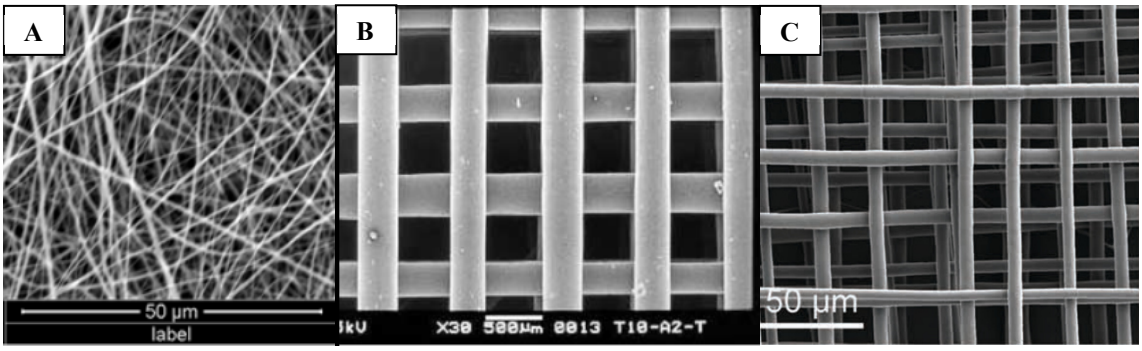

Figure 2: *Adapted Scanning Electron Microscopy (SEM) images of PCL scaffolds, fabricated via SES (A), FFF (B) and MEW (C). Figure A, B and C reproduced from [22], [23]and [3], respectively.*

1.2 Basic principles of MEW

MEW is an additive manufacturing technique, similar to SES, based on electrohydrodynamics, which allows the controlled deposition of fibres in the lower micrometre range (typically 2 - 50 µm [24]), thus making it advantageous for tissue engineering. Although even nanofibrous structures as small as 800 nm have been obtained via MEW [25], it is important to note that this is the exception to the rule.

1.2.1 Solution Electrospinning

Electrospinning is based on the uniaxial elongation of a viscoelastic jet originating from a polymer melt or solution by applying electric charge [26]. It allows the production of fibres, which are formed due to solidification of the melt or loss of the solvent. The diameters of the resulting fibres range from tens of nanometres to a few micrometres [27].

Figure 3 visually represents the basic principle of SES: A homogeneous polymer solution, for example PCL dissolved in acetic acid [28], is loaded into a syringe. A syringe pump is used to extrude the solution at a constant rate from the spinneret, e.g., a blunt tip needle connected to the high voltage (HV – in the order of kilovolts) power supply. This allows the spinneret a dual task of being a dispenser as well as an electrode [29]. The counter electrode that the fibres are directed towards is called the collector and is placed at a defined distance from the spinneret and may be either grounded or oppositely charged [30].

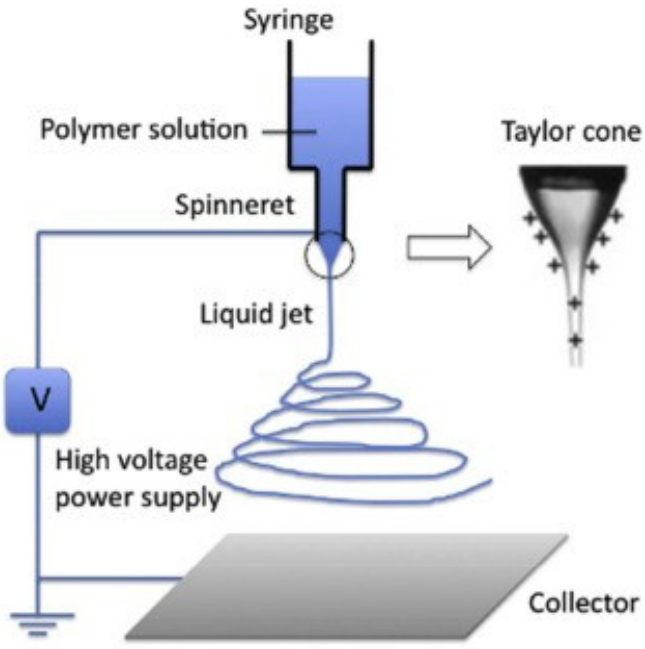

Figure 3: *Schematic setup of a basic electrospinning system [31].*

There are different collector geometries available, for example a stationary plate that allows the fabrication of a pile of randomly layered fibres or, rotating drum configurations that allow an even spreading of the non-woven mesh into a desired shape. Depending on the chosen polymer and the application the substrate that the fibres are deposited to can be made of amongst others, glass, metal and silicon wafers [32].

Typically, when a drop of polymer solution leaves the tip of a capillary it forms a hemispheric shape due to its surface tension. After leaving the capillary, the emerging liquid jet will have a cylindrical shape while falling under gravity. As the length of the stream increases the jet will lose its constant radius and break into droplets that have a smaller total surface area, as seen in Figure 4 A. This phenomenon is called Plateau-Rayleigh instability, which implies the existence of tiny perturbations inside of the jet [33]. When applying voltage to the spinneret, a charge on the surface of the solution is created, which leads the drop (Figure 4 B) to experience two kinds of electrostatic forces, namely, a mutual electrostatic repulsion between the like charges, as well as the Coulombic force of the external electric field [26]. This electrical potential causes a movement of the charges and thereby a movement of the drop. As per electrohydrodynamics, the distortion of the fluid evolves from a conical shape, called a Taylor cone, which is caused by increasing repulsive electrostatic forces, to a charged jet that gets drawn towards the collector as soon as the repulsive forces become predominant at the critical voltage Vc. Depending on the applied voltage, the viscosity of the solution and the molecular weight of the polymer, the fluid molecules can lose their cohesion instead of building a jet. The latter phenomenon is called electrospraying and is also dominated by Rayleigh-Plateau instabilities [15, 26, 29, 34, 35].

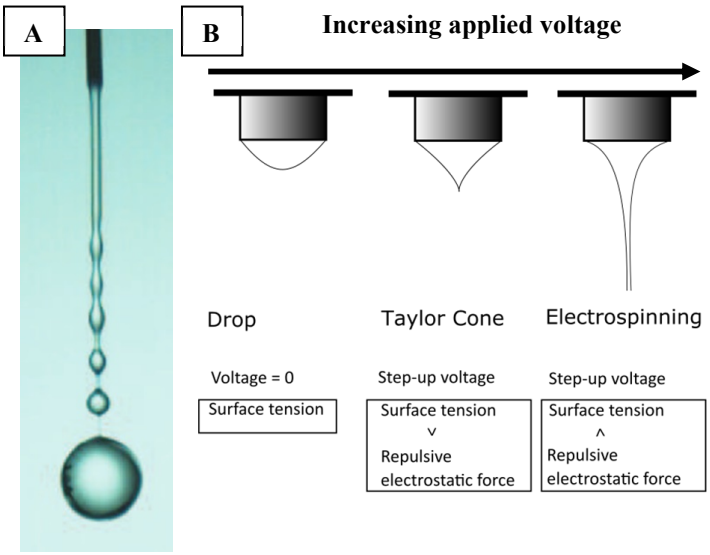

Figure 4: *A liquid stream breaking into multiple droplets according to Plateau-Rayleigh instabilities (A) and the effects of increasing voltages on drops of polymer solution (B). Figure A reproduced from [36], figure B adapted from [34].*

As shown in Figure 5, the jet that is produced during the electrospinning process initially follows a straight path after leaving the orifice but later undergoes a whipping movement, which is the essential mechanism of SES. At this point, Rayleigh-Plateau instabilities are fully stabilised, and the occurring instabilities are merely electrically driven [37]. At high charge densities, the whipping instability occurs, which leads to multiple bending segments that are induced by slight bends in the fibre and their electrostatic repulsion. This effect combined with the incipient evaporation of the solvent results in even smaller fibres due to the whipping inducing a mechanical stretching of the jet, and if not managed leads to a rather chaotic fibre formation [35].

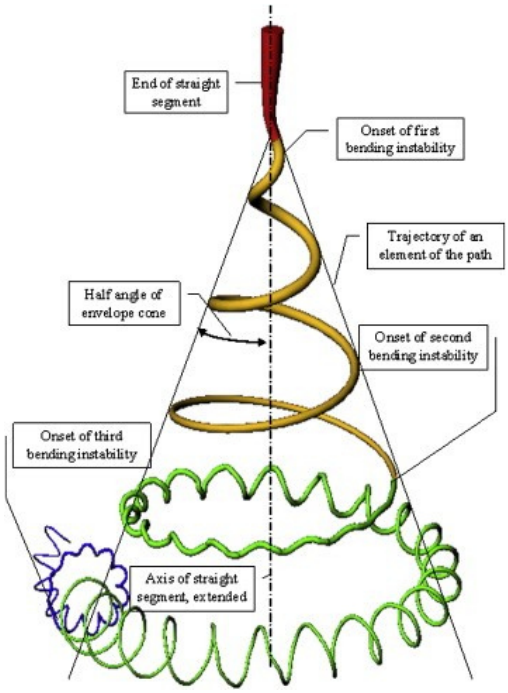

Figure 5: *Schematic representation of the electrical bending instabilities that occur during SES, containing a straight segment, which gets transformed into a 3D coil that keeps spiralling throughout the process [35].*

1.2.2 Melt Electrospinning vs. Solution Electrospinning: Setup and physics

Electrospun fibres are used in a variety of areas such as biomedical applications [38], drug delivery [39], wound dressing [40], filters [41], batteries [42] and catalysts [43]. As mentioned before, electrospinning is a polymer processing technique that not only applies to polymer solutions but also polymer melts. The most obvious advantage to use melts instead of solutions is the redundancy of toxic solvents that otherwise have to be removed from the fibres, for example via fibre heating [44], to make them applicable for medical purposes, which is difficult as well as expensive [45].

Regarding the used equipment and the basic principles, MES does not differ too much from SES: There needs to be a HV supply, a syringe with a suitable feeding system and a collector. After extruding a pendant drop, the repulsive electrostatic forces overcome the surface tension, and a charged jet is emitted onto the collector and solidifies, delivering a non-woven mesh with a diverse range of fibre diameters (from 270 nm [46] to 50 µm [3]).

The biggest difference in the equipment setup is the controlled heating element, which is necessary to melt the polymer uniformly, as well as a temperature sensor that makes it possible to manage the temperature of the melt and keep it at or close to a constant target temperature. Usually, MES systems use electrical heaters because of their easy assembly and user friendliness. Since the heater needs to be connected to the syringe and therefore to the spinneret, the safest setup for MES is to connect the HV to the collector and to ground the spinneret in order to separate the heater from the HV source. This inversion of the system is possible provided that the polarity of the ES system is arbitrary and the resulting electric field achieves the same strength in any approach [27]. Alternative heating sources are available: For example an infrared heating chamber that provides electrical insulation and hence overcomes the need for a spatial separation of syringe and voltage supply [47]. This also applies to lasers that only heat the tip of a polymer filament, which offers the great advantage that the polymer does not have to be melted all at once for a long period of time. This instance will prevent thermally sensitive materials from degrading too quickly [48]. Further options include heated fluids that circulate around the syringe, heated air that could be supplied via a hot air source, e.g., a heat gun [48] or fire heating [49].

Regarding the electrospinning process there are distinct differences between the use of solutions and melts caused by the major divergence of their jet paths:

The bending instabilities of polymer solutions in the SES process have been described in Section 1.2.1. Nevertheless, the whipping process is not present or rather weak during MES [27, 50, 51]. As previously mentioned, the whipping during SES is mainly caused by the high charge density on the surface of the liquid. This is presumably due to the fact that most polymers used in MES are electrically insulating and do not possess a high electron or charge-carrying capacity, preventing coulombic charge repulsions from rising along with the jet [52]. In addition, polymer melts have higher viscosities than polymer solutions, which most likely is also an influencing factor for the reduced jet whipping [27, 53]. This characteristic of MES is the fundamental basis of the aforementioned MEW that works with a moving collector, as seen in Figure 6.

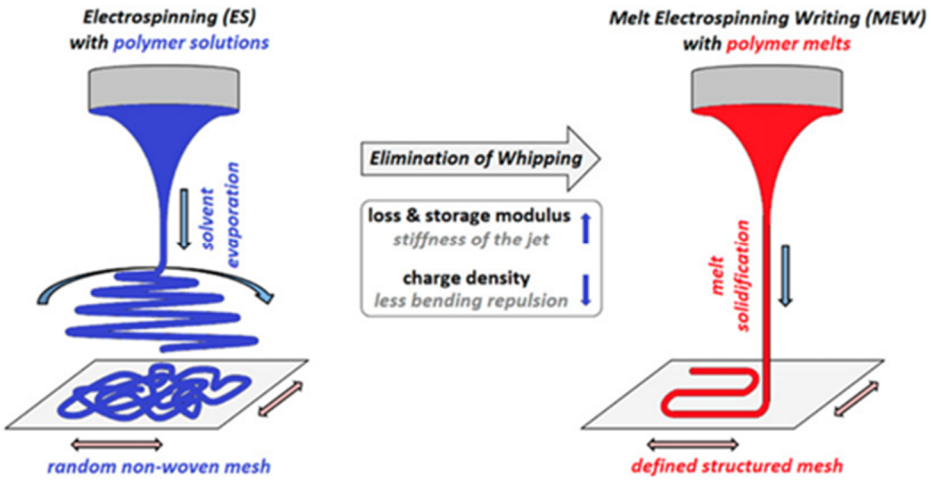

Figure 6: *Schematic of the chaotic fibre deposition during SES and the controlled deposition during MEW with responsible physical factors [25].*

Although the bending instabilities during the MES process are not as strong as in SES, it is still necessary to decrease the distance between spinneret and collector (30 mm or less [3]) to achieve accurately deposited fibres in a direct-writing manner.

A comparable technique called Near-Field Electrospinning (NFES) has been established for SES [54] that requires certain changes in the setup compared to conventional SES: In SES there is a distinct connection between fibre diameter and spinneret size [51]. For the NFES of solutions, a very small needle tip is crucial to obtain small fibres since the mechanical stretching of the bending instability is omitted [54, 55]. This technique also requires a lower working voltage than conventional SES in order to reduce the whipping of the jet [56]. Regarding the accuracy of the fibre deposition, this technique is still highly limited due to the strong bending effects. It was shown that this problem could be overcome with the help of a guiding electrode [57]. Compared to MEW, the fibre morphology from NFES is rather coarse owing to the solvent evaporation, which in parts now occurs after the deposition since there is a smaller gap between the spinneret and the collector. Figure 7 allows a comparison between NFES (A and B) and MEW fabricated fibres (C and D).

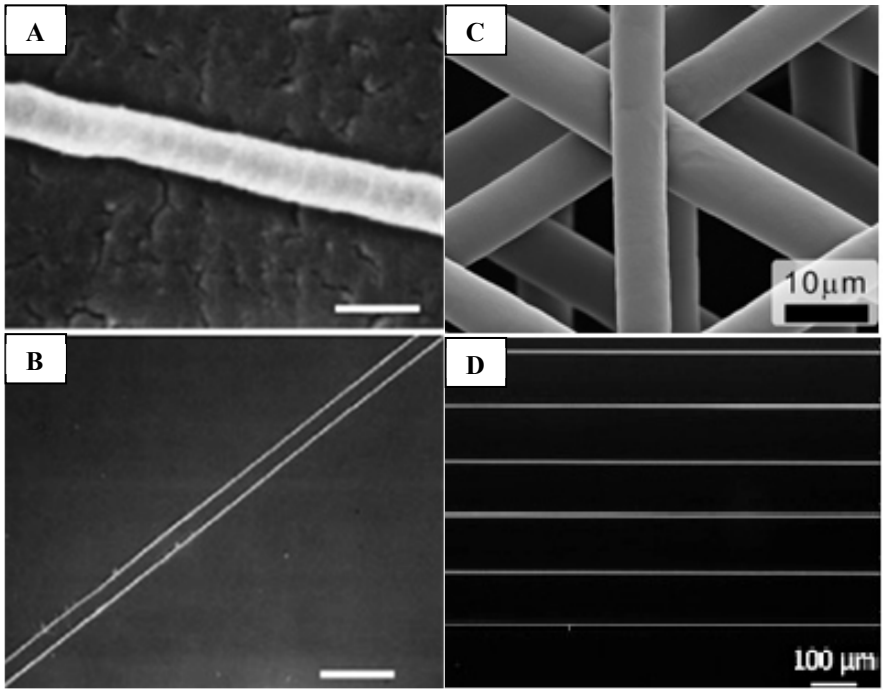

Figure 7: *Comparison of the morphology and deposition accuracy of fibres obtained via NFES (scale bar: 500 nm (A) and 100 µm (B)) and MEW ((C) and (D)), Figure A and B adapted from [54], Figure C and D adapted from [13] and [58], respectively.*

MEW can be seen as a combination of FFF and SES, utilising both techniques' advantages: Using polymer melts as in FFF, making it unnecessary to deal with additional costs for and the cytotoxicity of solvents and achieving

a much more predictable jet path as in SES instead. But at the same time using the electrostatic effects on fluids, allowing the fabrication of significantly finer fibres compared to FFF.

1.2.3 MEW Process Parameters

For the fabrication of ultrafine fibres using MES and MEW, there are certain parameters that need to be considered. Regarding the material parameters, a lower molecular weight results in a decrease of the fibre diameter due to less chain entanglement. The latter is the main cause for a low Melt flow index, which is a factor that quantifies the flowability of melts [27, 59]. It has been stated that in MES, the best fibre quality was achieved with molecular weights between 40 and 80 kDa [48]. In order to enhance the processing performance, it is possible to blend the desired materials with lower molecular weight polymers [60]. Furthermore, the molecular weight has a strong influence on thermal, structural, and mechanical properties of the fabricated fibres [51]. The stereoregularity of the polymer plays another important role [59]. Thus, isotactic polypropylene (PP) produces finer fibres than atactic PP, which is possibly owed to steric effects that prevent close packing of the macromolecular chains in atactic PP and therefore cause poor crystallisation [27, 59]. The viscosity of the material should not be too high as to inhibit extrusion through a heated nozzle or too low as to overflow without control out of the heated extrusion nozzle. Too low viscosities are a result of very low molecular weight and probably not suitable to produce a continuous fibre. Too high viscosities can cause nozzle blockage, result in thick fibres or even prohibit the spinnability of the polymer because the electric force might not overcome the viscous resistance [61, 62].

Specific MEW process parameters and their impact on produced structures are outlined below.

- Temperature:

The fibre diameter is mainly affected by the temperature setpoint of the heating system. When the temperature increases, the viscosity decreases, along with the fibre diameter and its standard deviation [27, 51]. At the same time the temperature should not be excessive, in order to prevent degradation of the polymer at elevated temperatures [48, 51].

- Voltage:

In general, applying a potential difference between the heated nozzle and the collector is the basic requirement for the electrospinning process. The fibre diameter will decrease with an increasing electric field as the viscous melt undergoes an increasing dragging force [51, 59]. But with a too high voltage, the Taylor cone will diminish, and the fibre diameter will become bigger [27]. Polymer melts require a stronger electric field than solutions in order to get dragged to the build plate due to their higher viscosity [63]. A greater electric field strength can be provided by choosing a higher voltage and/ or a conductive material since these two parameters determine the charge density on the surface of the jet. However, MEW works in a much shorter collector-spinneret distance than SES, which again requires a lower voltage to prevent electrical arcs but also a breakage of the jet because of the additional bending effect [45, 54]. By using a higher applied potential difference, a higher melt material flow rate becomes crucial in order to maintain good quality fibres [64]. Another effect that occurs during MEW and limits

the attainable thickness of scaffolds and the pore size, is the build-up of residual charges in the collected fibres that will lead to a repulsion between the fibres and the jet [65].

- Ambient conditions:

The effect of variance in ambient conditions on fibres fabricated via MEW has not been thoroughly investigated yet. Relative humidity and environment temperatures are known to have a high impact on solvent evaporation during the SES process, whichdoes not occur during MES. However, an influence of these conditions on fibre diameter and morphology should be considered [27, 45]. Therefore, measurement and management of these conditions is advised so that the effects of variance can be limited.

- Spinneret:

Compared to SES, the spinneret size in MES is generally larger, i.e., a larger nozzle diameter ideally in the order of 400 µm to 600 µm [66], because of the higher viscosity of polymer melts . As the size of the orifice decreases, the fibres will also decrease in their cross-section dimension. However, it is important to consider that small spinneret sizes (less than 400 µm inner diameter) can result in larger fibre diameters due to the high pressure that is needed to form a Taylor cone [66]. There are different kinds of spinnerets available for MES, for example needleless systems using a flat disk. Here, the disk is submerged into a polymer melt bath and then turned, hence placing the melt in physical proximity to the collector [63]. This approach has not been explored for MEW systems as thus far needles/ single controlled nozzles have been used to obtain a controlled and accurate fibre deposition.

- Flow Rates:

MEW utilises low flow rates that allow a predictable and continuous jet path, which is essential for operation of systems over extended time periods. By increasing the flow rate, more polymer is drawn towards the collector, hence the fibres become coarser [24, 64]. With low applied air pressures the jet can exhibit pulsing, which is defined as the undesired sectional oscillation of the fibre diameter [24, 58]. The fibre diameter can be adjusted by aligning the mass flow rate with collector speed variations, a stable MEW process is obtained with flow rates of typically 20 – 50 µL/h [58, 65, 67].

- Collector:

A stationary collector results in a random layering of the fibres while using a moving collector makes the direct-writing method possible. The fabrication of differently patterned structures is possible via the geometry of the collector, for example well defined tubular structures can be achieved with a rotating cylindrical collector [68]. Also, the type of substrate for the fibre collection, e.g., glass or aluminium, can affect the way fibres are collected [27, 69]. The collector rotational or translational speed determines the path of the collected fibres and their diameter.

With specific attention to the collector, Figure 8 A demonstrates the shape of the jet profile in accordance with different fibre drawing rates: State 1 illustrates the buckling effect in a stationary collector with a collector speed

s_c of zero. With this setting, the jet will bend due to a compressive force and not be deposited straight beneath the spinneret [3, 70]. As the collector speed is increased, there is a balance between the compressive and new established tensile force, which results in a fibre deposition directly beneath the spinneret, as seen in state 2. Here, the jet speed s_j equals the collector speed. State 3 shows the result of a collector speed that is higher than the jet speed. Here, the point of contact between the jet and the collector lags behind the point below the spinneret. With this setting, the viscoelastic jet gets elongated due to mechanical stretching and hence, the fibre diameter can be reduced. If the collector speed is much higher than the jet speed, as seen in state 4, the jet gets even more elongated. But this results also in less accurate positioning of the fibres, a circumstance that becomes apparent as soon as the collector changes its direction [3, 24]. This relation in connection with applied air pressures and collector speeds is shown in Figure 8 B: With increasing applied pressures while keeping the velocity of the collector movement constant, the jet experiences less dragging force and therefore a more unstable path, which is analogous for increasing speeds at a constant flow rate.

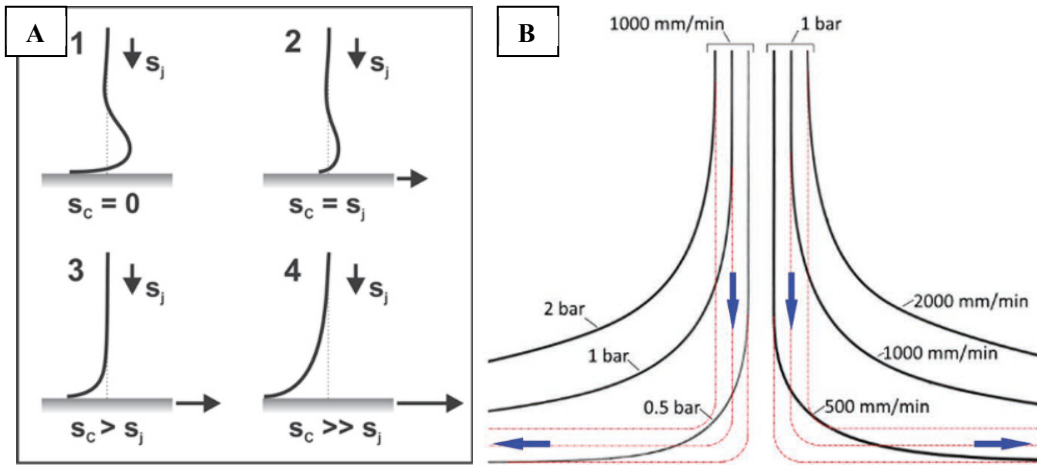

Figure 8: *Schematic illustration of the dependence between the speed of collector s_c and the speed of the jet s_j, reproduced from[3] (A); programmed collector path (dashed red line) and direct-written lines (black) approaching and turning 90°, reproduced from [24] (B), blue arrows indicate the direction of motion.*

From the point where the collector speed becomes higher than the jet speed, straight fibres are produced. This point is called a critical translation speed (CTS). Figure 9 shows the effects that occur while printing below the CTS [58]. These non-linear fluid patterns have already been described for falling viscous liquids under conditions that do not correlate to effects of electrohydrodynamics [71]. Collector speeds above the CTS result in structures that can be seen in Figure 9 A. Speeds below the CTS turn the deposited fibre with decreasing s_c into sinusoidal meanders (Figure 9 B), a pattern with translated coiling (Figure 9 C) and "figure of eight" loops (Figure 9 D) [58].

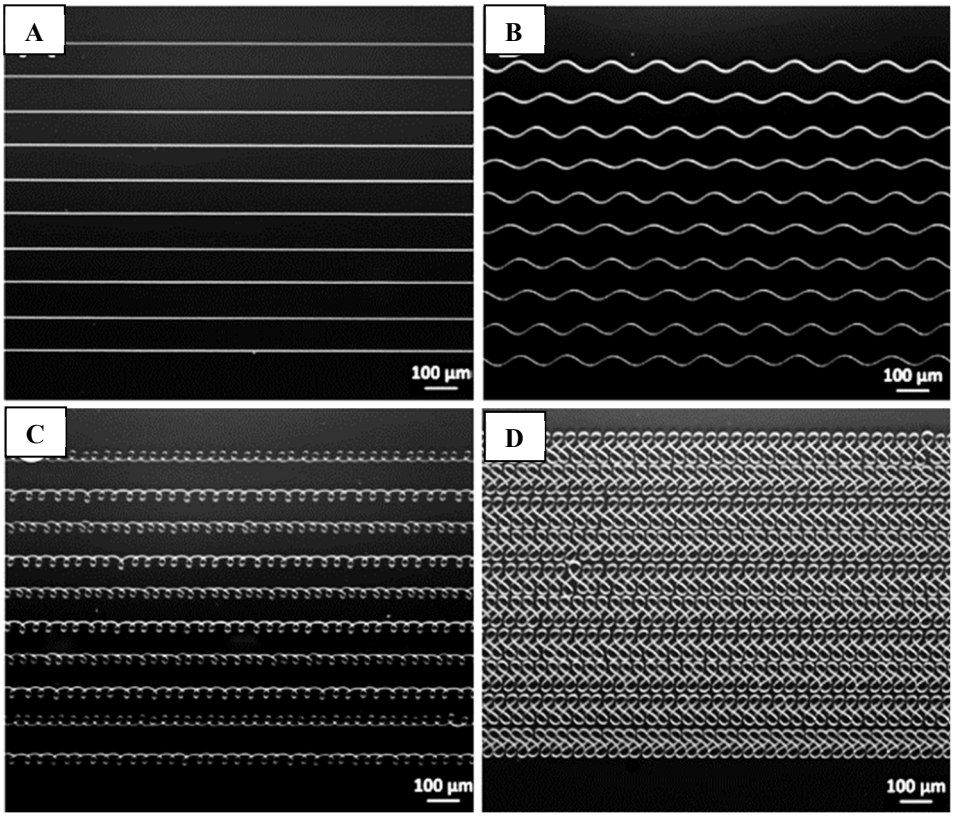

Figure 9: *Different patterns that occur during the MEW process of PCL above (A) and below (B-D) the CTS, adapted from [58]. Above the CTS, the fibres are deposited in straight lines (A). With decreasing collector speeds, the deposition of the fibres turns to meanders (B), coils (C) and "figure of eight" loops (D).*

A decreasing working distance between the collector and the spinneret will prevent a sufficient thinning of the jet before it is collected, leading to coarser and thicker fibres. But at the same time in the instance where fibres are not properly cooled down when collected, there can be a benefit of allowing fusion of the fibres at crossover points in produced multi-layer structures, which stabilises and reinforces the fabricated structures [27].

In summary, finding the right MEW process parameters is mainly dependent on the kind of material that is used and its properties, and is often challenging because each process parameter and its variation can have a direct impact on other parameters.

Although most of the research on MEW uses controlled and straight architectures with a predictable pore size [3], for example box-like structures [72], other approaches utilise the crimped patterns that can be achieved through MEW (e.g., Figure 9 C and D) to provide different mechanical properties, for example to mimic ligaments and tendons [73]. Due to the accessibility of fine and flexible lattices, MEW is a promising 3D printing technique for use in the Biofabrication field, which has been described by Groll *et al.* as "the automated generation of biologically functional products with structural organisation from living cells, bioactive molecules, biomaterials, cell aggregates such as micro-tissues, or hybrid cell-material constructs, through Bioprinting or Bio-assembly and subsequent tissue maturation processes" [74].

1.3 Biomaterials and their compositions

Having given an overview of the MEW fabrication process and some of the key influencing parameters, it is now important to discuss materials that are compatible with the MEW process but also critically, applicable for use in medical applications.

1.3.1 Requirements for biomaterials

Irrespective of the type of tissue that is aimed to be imitated, there are many fundamental requirements for the materials used for scaffold fabrication.

Besides the manufacturing technique of the suitable scaffold structures, which has been discussed in the previous chapter, an inherent prerequisite for a tissue scaffold material is its biocompatibility, which – for a long time – has been understood as its inertness, demanding the material to not cause any harm or toxicity to the surrounding tissue. The foreign body reaction, as shown in Figure 10, is the last stage of the very common inflammatory and wound healing process after implanting a medical device [75].

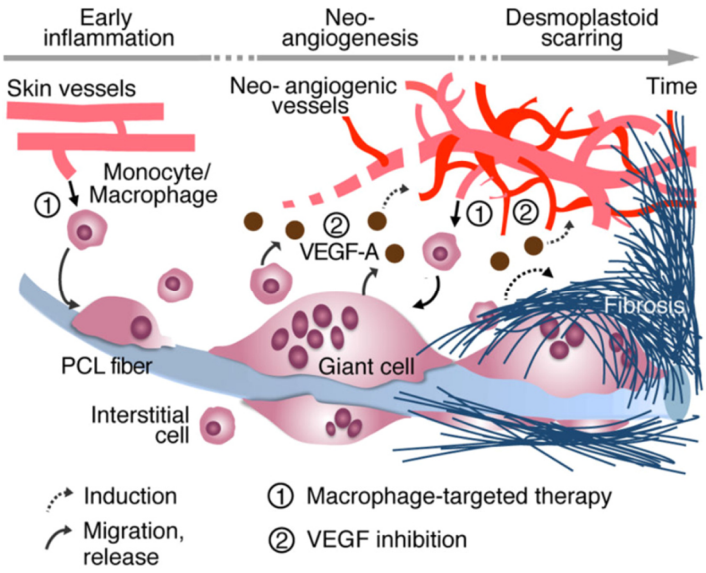

Figure 10: *Foreign Body Reaction and late-stage scarring mediated by macrophages, giant cells and neovessels [76].*

This kind of formation of excess fibrous connective tissue is often found around medical implants as an attempt of the body to isolate the foreign material from the rest of the body by surrounding it with dense scar tissue [77]. The biggest issue with this kind of scar tissue formation is the fact that it often prevents the implant from doing what it is supposed to do, like providing drugs locally [78].

While the foreign body reaction is difficult to manage, the material itself and its structural form need to provide a suitable environment for cell adhesion and migration. For many applications, the material should be biodegradable since it is only meant as a temporary, structural support that allows the body's own cells to replace the implanted

tissue engineered construct over time and to produce their own extra-cellular matrix (ECM). Commonly employed biocompatible materials for scaffolds include naturally derived materials such as collagen, or synthetically prepared materials such as poly (ε-caprolactone) (PCL) [4, 79].

A further requirement is that scaffold structures must possess sufficient mechanical strength and stiffness to withstand surgical handling and, after implanting, have mechanical properties that are similar to the damaged tissue. Thus, a scaffold combined with tissue-engineered cartilage that has the purpose of repairing large focal defects in a loaded knee joint needs greater mechanical strength than a scaffold used to repair an auricle, which provides more of an aesthetic function and undergoes less movement as well as being under a lower comparative mechanical loading [4]. At the same time, a scaffold used in a soft tissue environment should be flexible enough to not cause any damage to the surrounding tissue and thereby promote inflammatory host foreign body responses. Certain mechanical properties can be obtained by choosing different materials [1], scaffold architectures [81] and fabrication methods [82].

Over the last decades, biodegradable materials have been more and more in demand for medical purposes as for example implants like screws are not meant to stay in the body forever. Instead of submitting the patient to another medical intervention to explant the foreign material, it is often more beneficial to use a material that over time will get absorbed by the body. This approach saves time and spares the patient the stress of another surgery, additional costs and recovery time [83].

PCL is the most commonly investigated polymeric material for MEW. It has been widely used in tissue engineering research due to its availability, low cost , its approval by the Food and Drug Administration for the use in humans, its good processability, its thermal stability, and suitability for modifications [84]. Figure 11 shows the chemical structure of the polymer.

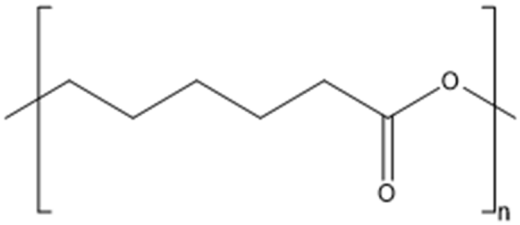

Figure 11: *Structural formula of PCL.*

PCL is a semi-crystalline polyester that is synthesised by ring-opening polymerisation of ε-caprolactone using a catalyst such as enzymes as well as organic or metal-based compounds [97]. It has a glass transition temperature of – 65 to – 60 °C and a melting point of 56 to 60 °C, depending on its molecular weight and degree of crystallinity [85]. While bacteria and fungi are able to biodegrade PCL, animal and human bodies do not have the necessary enzymes to do so. This is why the hydrolytic degradation process for implants made of PCL takes much longer by dissipating the polymer from the surface to its inside [86].

More recently, smart polymeric materials have started to emerge in the research field of tissue engineering with the aim of reacting to external stimuli like temperature, pressure, electric and magnetic field and pH. On another note, functionally graded materials (FGMs) are specifically designed to not only prevent the tissue from getting damaged any further but also to promote repairing processes.

1.3.2 Functionally graded materials

FGMs are advanced composite materials that are characterised by a compositional and/or structural gradient from one component to the other [92], as shown in Figure 12 as a demonstration of transitions within graded alloy structures [93]. The functionally graded composition can be found not only in combining different alloys but also within other material classes such as (particle filled) polymers [92].

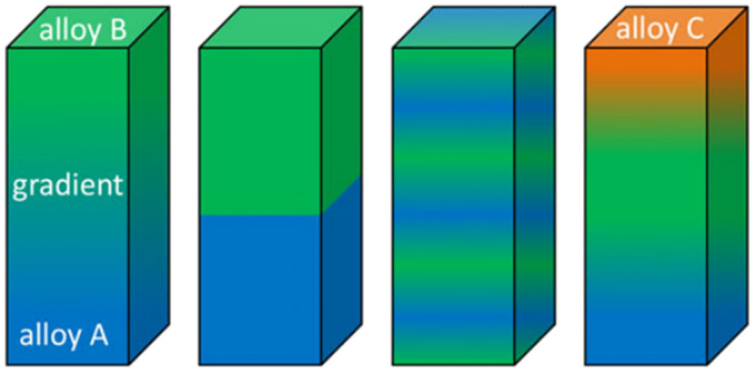

Figure 12: *Schematic of the range of Functionally Graded Material compositions accessible for Laser Deposition, processing different alloys, adapted from [93].*

FGMs are supposed to provide changing properties – which can be chemical, mechanical, magnetic, thermal or electrical – over their volume of the bulk material. This makes them accessible for applications that demand a specific function in areas such as automobile, aerospace, opto- and thermoelectronics, energy, and of course biomedicine [94]. The human body itself contains a lot of FGMs, such as in bones and teeth. Figure 13 shows the use of FGMs in teeth implants. By using a graded porosity in the anchoring of the prosthesis, the aim is to not only mimic the shape of natural teeth but also to minimise the elasticity mismatch between the jawbone and the titanium alloy Ti-6Al-4V and hence the stress shielding and thus improving the osseointegration properties of the implant [95].

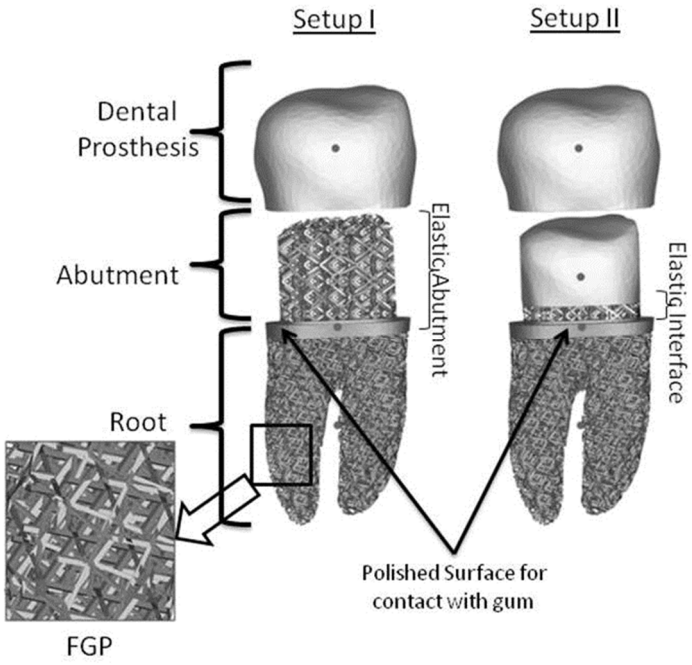

Figure 13: *Bio-adaptable dental implants with a functionally graded porosity (FGP)[95].*

1.3.3 Coaxially manufactured FGMs

While for teeth and bone replacement metal powder 3D printing techniques are favoured, it is also important to consider extrusion-based techniques for the FGM fabrication, especially the ones that allow the manufacturing of coaxial structures. That means that two (or more) materials are present and share a common axis [96], hence creating a gradient in the chemical composition. Core-sheath structures can be used to incorporate adequate mechanical characteristics into the produced materials while maintaining cell proliferation and nutrient dissemination [97] but they also find their application as drug delivery systems and, by including conductive materials, to transfer electrical signals [98].

Cornock *et al.* designed a nozzle for coaxial melt extrusion-based printing and used it for the fabrication of alginate hydrogel encapsulated in PCL. The printed scaffolds later were explored regarding the viability of an L-929 mouse fibroblast cell line that was embedded in the alginate matrix. This setup, which can be seen in Figure 14, required an independent control of temperatures and pressures for the coextruded materials because the sensitive material in the core does not need any heating for its processing, whereas the thermoplastic that forms the sheath and is supposed to hold the structure together has to be melted [97].

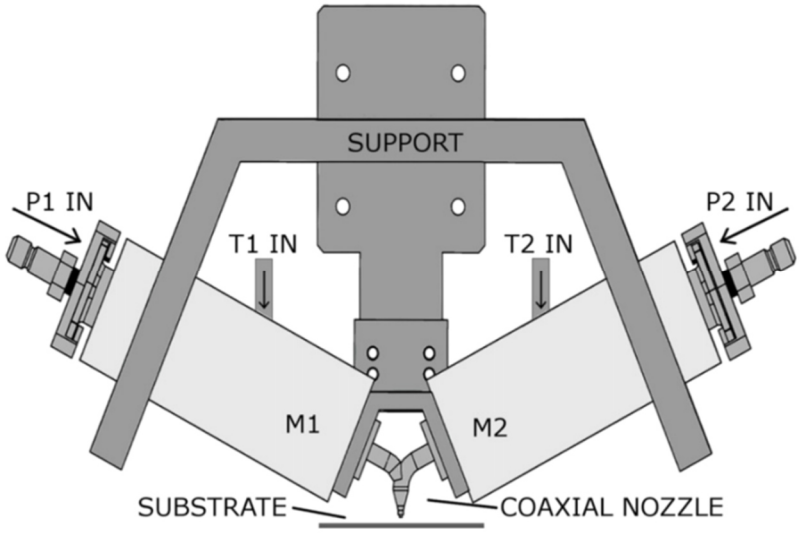

Figure 14: *Schematic of the coaxial melt extrusion printing system with material reservoirs M1 and M2, independent temperatures T1 and T2 and pressures p1 and p2 [97].*

Taylor *et al.* further investigated the previous work by making it accessible for thermoplastic filaments with a melting point of up to 275 °C, which increased the range of materials that can be used and also resulted in different morphologies dictated by the nozzle and the process parameters [96].

For the MES of coaxial structures, different core materials apart from polymers such as hydrocarbons [99] or rather perovskite microcrystallites have been used [100]. Other approaches were the fabrication via a partial melting and clamping of thin films [101] and furthermore using polymers of different molecular weights at different process temperatures [102]. –

Coaxial MEW has been established in early 2018 [103] as an attempt to allow the fabrication of core-shell structures that may be applicable as drug-carrier systems using a core material, which has been loaded with a drug while the shell slowly dissolves and acts as a barrier to the drug release rate [39, 104]. Previous studies have used an inverted fluorescence microscope in order to analyse the coaxially processed, fluorophore-loaded fibres [103]. In order to further investigate the process and the resulting structures, confocal laser scanning microscopy can be of interest for an optical sectioning of the fibres.

Apart from core-shell structures, there are two other aspects that are of interest for the coaxial MEW setup; first of all, there is the fabrication of hollow structures. In SES, hollow fibres are attained by producing core-shell fibres and later selectively dissolving [106] or sintering [107] the core material away. Hollow structures are known to be lighter and to have improved mechanical properties compared to dense structures [108] due to the cavity causing a resistance to being bent [109]. These properties make hollow fibres applicable in the textile industry and regenerative medicine [110, 111]; by using them in combination with microfluidics they can be of great interest for a variety of applications, including optics and information technology [112].

Second, a coaxial setup is also of interest for the production of Janus fibres. Whereas core-shell structures are made of an outer-inner composition of two materials, Janus structures show a side-by-side conformation and are usually processed by bottom-up routes, such as self-assembly [113-115]. In Janus structures, both components are allowed to interact with the surroundings, hence the heterojunction structure offers a possibility for designing of novel smart materials [114], such as reversibly actuating fibres that can be controlled with external stimuli like temperature, and that offer applications in robotics and biotechnology [116, 117].

1.4 Summary

There is a high demand for the further development of additive manufacturing techniques and associated process compatible materials for application in regenerative medicine. Advances in these areas will enhance functionality and accessibility of custom-made scaffolds that, in combination with cells and bioactive molecules, can be used for the repair of damaged tissues.

Different scaffold fabrication techniques have been presented, such as FFF and SES. MEW is a 3D printing technique that was first described in 2011 and combines the advantages of both, FFF and SES, by making well-defined and flexible fibres in the low micrometre range accessible without the need of toxic solvents. In SES and FFF, coaxial procedures are available that focus on the simultaneous extrusion of two materials that lead to functionally graded core-shell structures, which can be used in drug delivery or micro electro mechanical systems or, by using sacrificial core materials that get dissolved in post-processing, even hollow structures that are known for their light weight and excellent mechanical properties. By using a side-by-side extrusion of different materials, Janus fibres are feasible in different manufacturing techniques, which offer the production of smart materials that can change their properties by being exposed to external stimuli.

To date, all of the described approaches for MEW were focussing on a uniaxial processing. Therefore, a gap in the technology was identified and in order to allow the co-extrusion of different materials and further the possibilities of this relatively new 3D printing technique, a coaxial MEW setup was built in early 2018.

There is now the opportunity to further investigate the coaxial MEW process configuration and examine the potential in using this novel additive manufacturing approach to generate new micron-scale fibre structures and conformations.

2. Research aims

Scaffolds in combination with cells and bioactive molecules are 3D structures that have the aim to support the regeneration of tissue in a body. Biocompatibility of the materials and processes used in the production of scaffold structures is crucial in order to prevent the human body from reacting to the implantation with any kind of inflammatory response. Melt electrowriting (MEW) is an emergent process in the biofabrication field that allows for high resolution scaffold structures to be fabricated. Coaxial MEW is a recent approach to combine multiple materials during the MEW process offering the potential to create novel structures and material combinations.

The work presented here aims to evaluate polycaprolactone (PCL) composite materials and determine their applicability in the coaxial MEW process through production and characterisation of fine multi-material structures. To achieve this aim, work was segmented into the following objectives:

1. Establish a robust process for the incorporation of suitable fluorophore fillers within a PCL matrix and subsequently characterise the effect on the MEW process parameters as well as the structures by the addition of different percentages of the fillers. This objective will determine applicability of the chosen filler material, lead to elimination of non-compatible materials, and identify basic material parameters for uniaxial MEW processing prior to progression to a coaxial configuration.
2. Investigation of the coaxial MEW process and determination of the impact on process parameters due to filler materials, characterised through stereo microscopy and different fluorescence microscopy methods. This objective will identify the applicability of material ratios to be used in subsequent process evaluation.
3. Examination of structural features that can be practically achieved, including core-shell, Janus and tubular structures, through the coaxial MEW configuration and determination of their practicality.

3. Materials and Methods

The following chapter provides an overview of the materials, processes and optical imaging methods that have been used in this study. The primary polymer component in use within this body of work was polycaprolactone (PCL). This material has proven compatibility with the melt electrowriting (MEW) process as documented in the literature. The PCL was modified with the addition of fluorophores to allow a distinction between two polymer masterbatches being simultaneously processed through a coaxial MEW arrangement. The methods employed in optimising the polymer composites for visualisation through fluorescent imaging are presented. Furthermore, a detailed description is provided on the custom-built MEW system that allowed the fabrication of both uniaxial and coaxial PCL composite based structures.

3.1 Materials

The raw materials used for the fluorophore-loaded PCL were master batches containing the fluorescent dyes 1,1'-dioctadecyl-3,3,3',3'-tetramethyl-indocarbocyanine perchlorate (DiI) and 3,3'-dioctadecyclocacarbo-cyanine perchlorate (DiOC18), which have been purchased from Sigma Aldrich, and PCL that was obtained from Corbion Inc (PURASORB PC12, Lot#1412000249, 03/2015). These master batches have been prepared in advance using a compounding mechanism. Another fluorophore that has been investigated, named Rhodamine B, purchased from Sigma Aldrich, has been incorporated into PCL from Corbion Inc (PURASORB PC12, Lot#1712002224, 05/2018) that was also used in its neat mode as a comparison. The solvents used in the precipitation process were chloroform and hexane, both purchased from RCI Labscan. The preparation of the fluorescent thermoplastics was done by firstly dissolving a defined ratio of PCL and the respective fluorophore in chloroform and stirring the mixture for up to six hours in order to ensure a homogeneous blending of all components. This procedure was done at room temperature under exclusion of light by covering the beaker in aluminium foil. Hexane was added slowly for a controlled precipitation of the now coloured PCL. The sediment was transferred to a container covered in aluminium foil that contained small holes, so the substance could be dried in a fume hood at room temperature overnight. The resultant solid product was cut into smaller pieces and placed into a vacuum oven at 0.1 mbar for up to 48 hours at 40 °C for final drying.

3.2 3 Axis positioning stage and control

A custom MEW setup was developed and assembled for the requirements of the coaxial process in previous studies [103]. The first component of the setup to be described here are the stages of the printer. Three precision motorised linear stages with step resolution of approximately 0.5 µm, repeatability of < 2.5 µm and unidirectional accuracy of 15 µm (A-LSQ150B, Zaber, Canada) [118] were used to provide an XYZ positioning framework. The stages were simultaneously controlled using in house developed software written in the C++ programming language using the Qt Framework (The Qt Company Ltd.). This process facilitated control of the stages by first

defining the intended pathways through commonly employed G-Code commands, as outlined below, and then translating these instructions to the native RS232 serial interface commands of the stages [119].

The G-Code was generated from a simple spreadsheet, created with Microsoft Excel (Appendix A).

3.3 3D printing setup in the uniaxial MEW process

A high-voltage source (Gamma High Voltage Research Inc., USA) was used for the generation of a voltage potential between the collector and the grounded nozzle tip. The aluminium collector was mounted on the previously described X-Y stages. The tool head was mounted on the Z-programmable stage, which enabled fine distance control between nozzle tip and collector. For the melting of the plastic a heating element with temperature sensor is utilised (12V, 40W). The (micro-)controllers in use are Ultimaker 1.5.7 (Ultimaker, Netherlands) and Arduino Mega 2560 (Arduino, Italy). The melted plastic was extruded with the help of a pneumatic feeding system (AD 3300C, Iwashita Engineering Inc., Japan) and the resulting fibres were deposited through a 0.4 mm nozzle onto microscope glass slides (Cat. No. 7101, Sail Brand, China). The printing process was observed with a camera (CMLN-13S2M-CS, Point Grey Research Inc., Canada) that has been focussed on the nozzle tip. For safety purposes, the overall system configuration was placed into a semi-enclosed plexiglass box (Appendix A). This also helped to compensate for ambient conditions that might affect the process and, in addition, are minimised by placing the whole setup in a climate-controlled room with an average temperature of 23 ºC and an average humidity of 43%. Also, compressed dry air was applied to the box at a constant flow rate, bringing the humidity down to a stable value of 19 % and the temperature to 22 ºC. The components of the uniaxial tool head are presented in Figure 15.

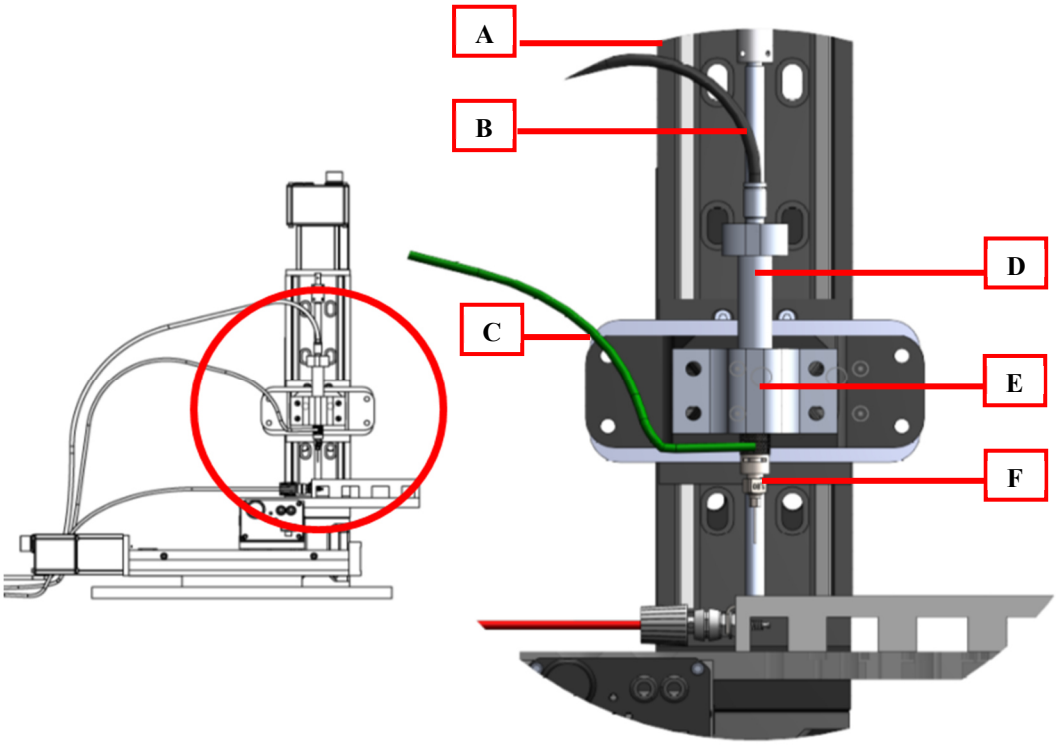

Figure 15: *Schematic of the assembled uniaxial tool head mounted onto the Z stage (A), with the pneumatically controlled (B) syringe (D), heating block in the Onyx bracket (E) and the grounded (C) nozzle (F).*

Figure 16 shows the assembled MEW system using the example of the coaxial tool head, which will be further discussed in the following section.

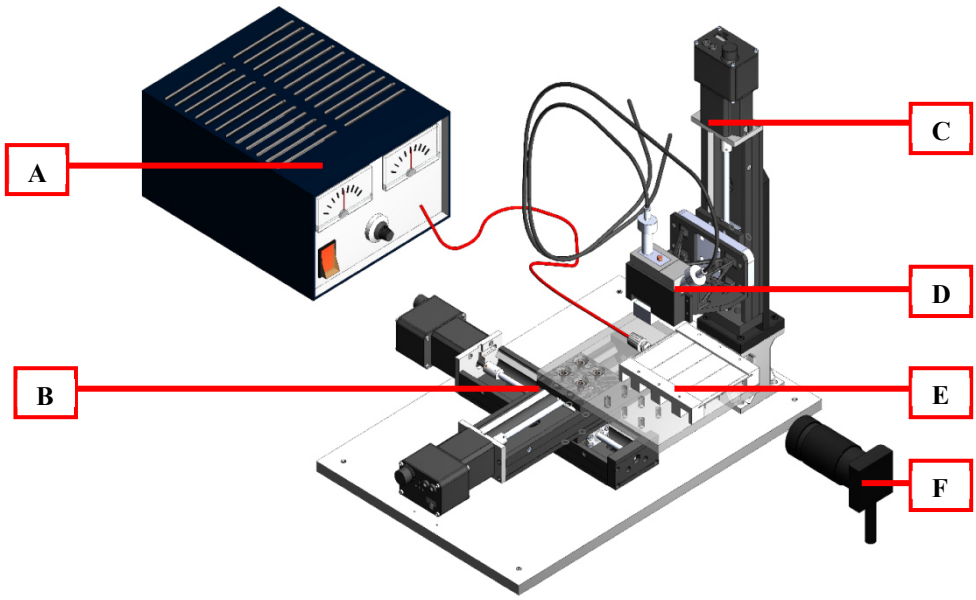

Figure 16: *Schematic of the assembled MEW system with HV supply (A), X-Y stages (B), Z stage (C), coaxial tool head (D), collector (E) and USB camera (F).*

3.4 3D printing setup in the coaxial MEW process

The general setup and control of the MEW system have been described in the previous section. To enable coaxial printing, a tool head was installed that contained a custom-made aluminium heating block wrapped in rockwool and Kapton© tape, which was inserted into a 3D-printed Onyx bracket (Markforged, Watertown, USA). All fibre samples were printed with a custom-built nozzle that has been fabricated via selective laser melting of the titanium alloy Ti6-Al-4V. The orifice was measured to have a size of 0.810 mm, for thermal insulation the nozzle was embedded into fireproof cement (Selleys, Padstow, Australia). The core and shell materials were applied via a pneumatic feeding system through 3 cc aluminium syringes (Inkredible by CELLINK, Goeteborg, Sweden), with the core material being inserted through a 26G luer lock needle. The composition of the coaxial tool head is detailed in Figure 17.

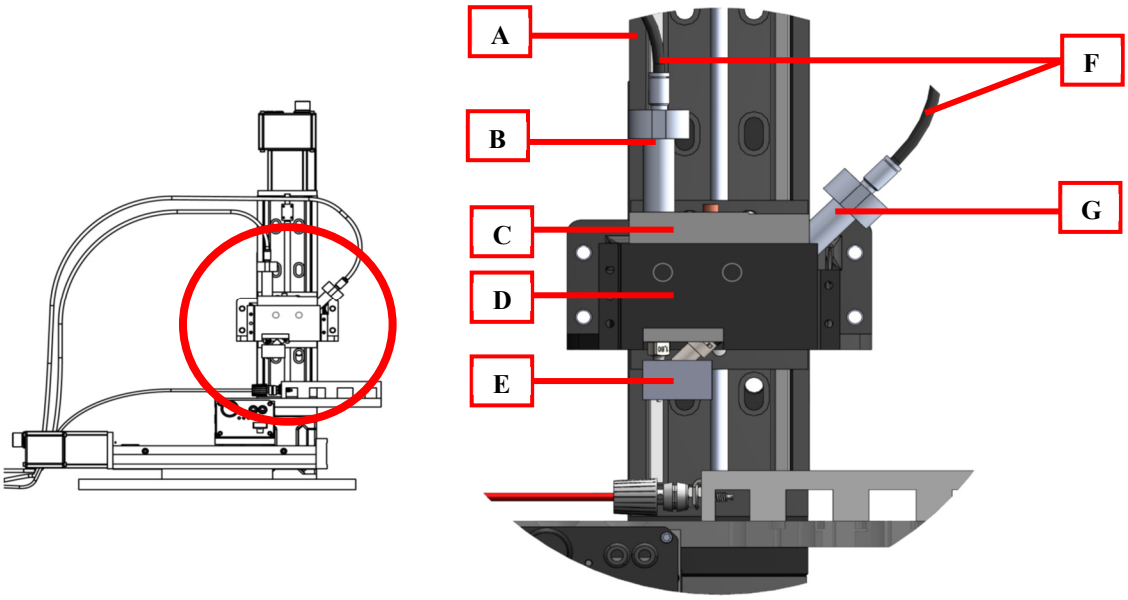

Figure 17: *Schematic of the assembled coaxial tool head mounted onto the Z stage (A), with pneumatically controlled (F) core (B) and shell syringes (G), heating block (C), Onyx bracket (D) and the grounded and heated coaxial nozzle that is embedded in fireproof cement (E).*

Figure 18 provides a closer look into the structure of the coaxial tool head with the two different heating elements being connected to the heating block around the syringe containers and the coaxial nozzle embedded in fireproof cement as well as the inner and outer channels of the nozzles that provide the polymeric materials.

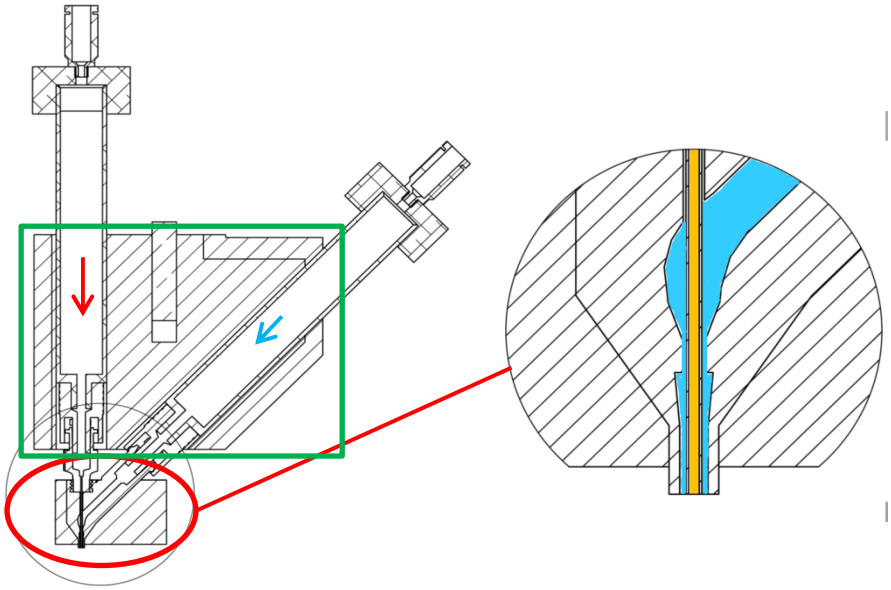

Figure 18: *Geometry of the coaxial tool head marking the position of the core (red arrow) and shell syringe (blue arrow) with two separate heating zones (green square and red circle) as well as an augmentation of the interior of the coaxial nozzle with the needle (yellow) that inserts the inner material into the channel that provides the outer material (blue).*

3.5 Optical imaging

The printing process was monitored using a USB camera (CMLN-13S2M-CS, Point Grey Research Inc., Canada).

Optical microscope images that allowed a first impression of the outer structures and diameters of the printed fibres were taken with a stereo microscope of the type M205 A (Leica, Germany). Fluorescent structures were examined using an inverted fluorescence microscope (Axiovert 40 CFL, ZEISS, Germany) as well as confocal laser scanning microscopy (TCS SP5 II, Leica, Germany).

Scanning electron microscopy (SEM) was performed using a Crossbeam 340 SEM (Carl Zeiss, Göttingen, Germany). Prior to SEM imaging, samples were platinum-coated using a Leica EM ACE 600 sputter coated (Leica, Germany). In situ cutting of the fibres was performed using a gallium focussed ion beam at a current of 700 pA and an acceleration voltage of 30 kV.

3.6 Summary

For the characterisation of melt electrowritten fibres, different concentrations of different fluorophores have been incorporated into a PCL matrix using an adjusted precipitation process. Fibres were produced using a custom-built MEW system that provided the possibility of a uniaxial printing of single materials as well as a co-extrusion of two different composites. The resulting fluorescent fibres have been investigated regarding their composition and general properties using different microscopy methods such as confocal microscopy and SEM, which also allowed conclusions about the printing process.

4. Results and Discussions

This research intended to examine the MEW process and the capability of printing multi-material structures through a coaxial nozzle configuration from PCL filled with different fluorophores with outer dimensions in the lower micro metre range. A custom-built MEW setup was utilised in the processing of fluorophore laden PCL. Masterbatches of polymers were distinguished through the addition of fluorophores with significantly different colours so that multi-material structures could be later optically analysed. Furthermore, a way of incorporating fluorophores into a polymer matrix will be presented. The uniaxial MEW process of the resulting fluorescent composites will be investigated regarding their heat stability as well as their critical translation speeds (CTS). Finally, the co-extrusion of PCL filled with different fluorophores and generated coaxial MEW structures will be analysed, before investigating the potential to use the same hardware in the production of Janus fibre structures and hollow fibre structures. This work will highlight that these morphologies are possible but not yet reliable. Significant improvements to the hardware are suggested and rationalised in context of refining the process so that stable process control can be achieved in further research outside of the scope of this thesis.

4.1 Incorporation of fluorescent dyes into the PCL matrix

For the analysis of the coaxial MEW process described in Section 4.3, the different regions in the fibre will be distinguished using fluorophores. The following sections describe an approach of incorporating fluorophores into a PCL matrix using precipitation chemistry. For a proper characterisation of fluorophore-containing PCL fibres attained with coaxial MEW different aspects were crucial regarding the fluorophores. The following sections are going to describe an approach of distributing the dyes evenly in the polymer using a precipitation process while also ensuring a sufficient drying of the precipitates.

4.1.1 Mixing the components

Three different candidate dyes have been investigated: Figure 19 shows the chemical structures of Rhodamine B (Figure 19 A), DiI (B) and DiOC18 (C).

DiI (red staining) and DiOC18 (green staining) are lipophilic tracers that are often used to label and distinguish cells while not affecting their physiological properties. The dyes have excitation and emission maxima that are separated by over 60 nm and therefore a contrasting two-colour labelling is facilitated when they are used in combination [120]. By using Rhodamine B in combination with DiOC18 the excitation/ emission gap between the dyes could be further increased.

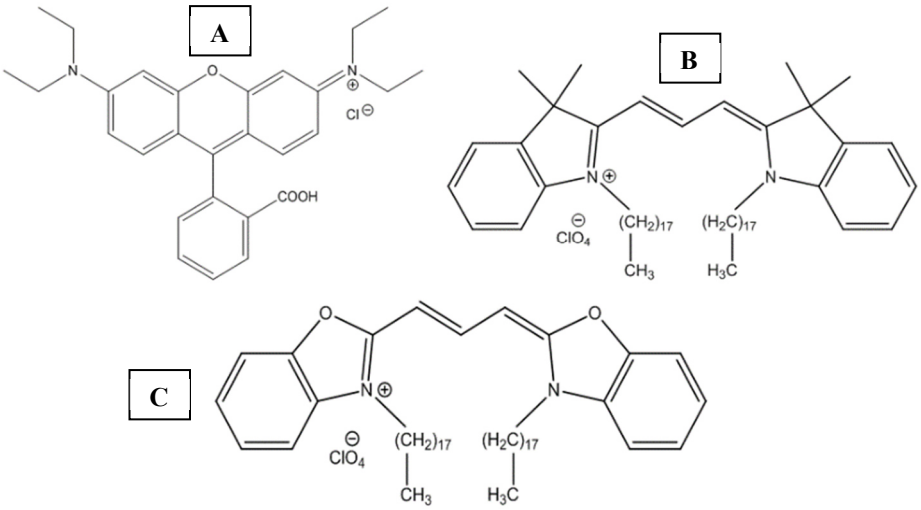

Figure 19: *Chemical structures of Rhodamine B (A), DiI (B) and DiOC18 (C).*

Table 1 provides an overview of the fluorophores presented in Figure 19 regarding basic characteristics such as their dye classes, chemical formulae and physical appearances. Also, their decomposition points and fluorescent properties are named, which were important for the fabrication process and fibre characterisation. Furthermore, suitable solvents are presented that were of importance for the precipitation alongside the final fluorophore concentrations used in this study.

Table 1: *Overview of the differences between the investigated fluorescent dyes.*

Name	DiI	DiOC18	Rhodamine B
Chemical/ Dye class	Cyanine	Cyanine	Fluorone
Molecular formula	$C_{59}H_{97}ClN_2O_4$	$C_{53}H_{85}ClN_2O_6$	$C_{28}H_{31}ClN_2O_3$
Physical form	Red solid	Yellow orange solid	Dark purple solid
Solubility	Ethanol, methanol, N,N-dimethylformamide, dimethyl sulfoxide [121], chloroform [122]	Ethanol, methanol, N,N-dimethylformamide, dimethyl sulfoxide [120], chloroform [122]	Chloroform [123], dimethylsulfoxide [124], ethanol, methanol [125]
Decomposition point	68 °C [121]	unknown	210 °C [125]
Absorption ($\lambda_{max, MeOH}$)	549 nm [121]	484 nm [120]	553 nm [125]
Emission ($\lambda_{max, MeOH}$)	565 nm [121]	501 nm [120]	627 nm [125]
Concentrations used	various	0.0011 wt%	0.17 wt%

On one side, an even distribution of the dyes was demanded in order to get a fair imaging of melt electro-written fibres without single particles or agglomerates disturbing the outcome. Figure 20 shows how unevenly distributed dye particles and their formation into agglomerates could negatively affect (represented as concentrated "hot spots") the fluorescence imaging of Rhodamine B incorporated in PCL.

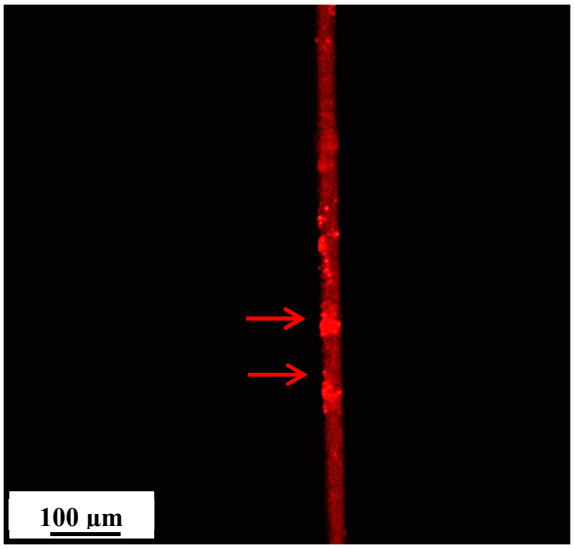

Figure 20: *Red fluorescence confocal microscopy imaging of Rhodamine B incorporated into PCL, clearly showing single particles as well as agglomerates of the dye (red arrows).*

On the other side, an uneven distribution of the dyes could have an impact on the MEW process itself, since the three fluorescent dyes were of ionic nature as shown in Figure 19. Hence, uneven distribution of the fluorophores that add charges to the polymer melt jet would lead to variation in carried charge that could lead to uneven fibre diameters since the accelerating voltage would cause a stronger drag on the ionic dyes and especially agglomerates than on the surrounding polymer.

By dissolving the dyes in chloroform along with PCL and stirring the mixture for up to 6 hours under exclusion of light in order to protect the dyes from photobleaching these effects have been minimised, the more even distribution is shown in Figure 21.

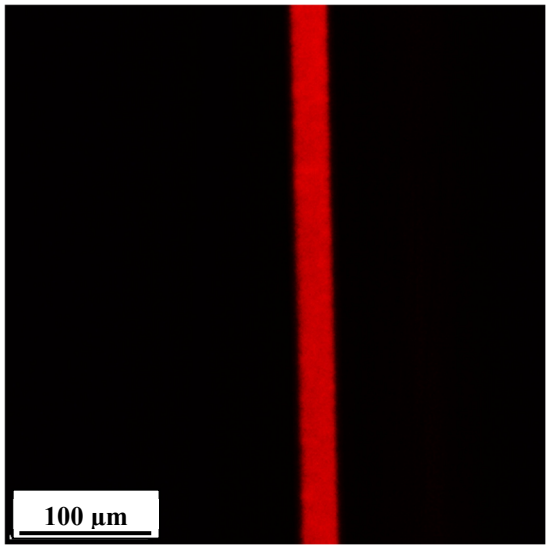

Figure 21: *Red fluorescence confocal microscopy imaging of Rhodamine B incorporated into PCL, showing a more even distribution compared to Figure 20.*

Yet, it has to be noted that while the dyes could be dissolved in certain substances, they could not be molten. While there was even distribution of the dye within the polymer during this pre-processing stage the particulate nature of the dye within the polymer in combination with remelting and the low mass flow rates utilised in the MEW process could cause particles to move freely within the polymer matrix and fuse again, making agglomerations a persistent challenge. This effect could be identified for composite materials containing graphene particles as presented in Appendix C.

4.1.2 Drying the precipitates

For MEW, it is important to use dried materials since residual solvent can affect the fibre fabrication process due to a lowered viscosity in the melt-solution mixture as well as an evaporation of the solvents during the printing as described by Ferreira *et al.* for the behaviour of solutions during the SES process [28].

Initial attempts of drying PCL that has been dissolved in chloroform and precipitated with hexane included heating it up to 40 °C in a vacuum oven at 0.1 mbar for 24 h while regularly ventilating to prevent the formation of an equilibrium state between the solvent in its liquid and gas mode [126]. This approach turned out to be insufficient. During the later described coaxial fibre fabrication process of materials prepared in this way, solvent was observed to be trapped inside of the melt, leading to inconsistent fibre diameters and breakages. The latter also resulted in the dye being carried out of the fibre by the solvent. This effect can be observed in Figure 22, an inverted fluorescence microscope imaging of three fibres, which clearly shows leaching of the dye onto the print substrate.

Figure 22 A shows the red, B the green fluorescence channel, C the brightfield image and D the overlay of all three channels of three fibres: Fibre 1 contained only the outer material (red) that was dried for 24 h and due to

residual solvent being dispensed in the fibre broke and spread the fluorophore over the glass slide. Fibres 2 and 3 were printed with just the inner material containing DiOC18, which had been dried for 48 h instead.

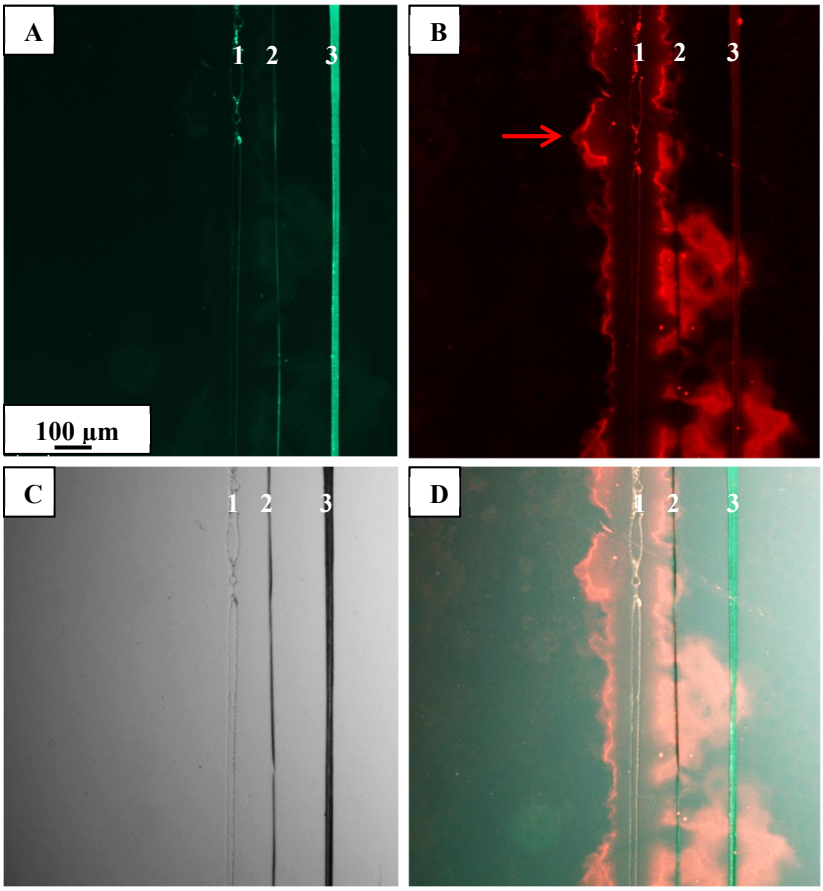

Figure 22: *Green (A) and red (B) fluorescence channel, brightfield image (C) and an overlay of all 3 channels (D) of one fibre that contained Rhodamine B-loaded PCL, which carried a too high amount of solvent (1), leading to jet breakages and a spreading of the fluorophore onto the glass slide (red arrow), and two fibres that contained DiOC18-loaded PCL, which has been dried for 48 hours (2, 3).*

The following results were achieved with materials that have been dried for 48 hours at 40 ºC and 0.1 mbar with regular ventilation while cutting the plastics into preferably small pieces with an edge length of only 1 mm beforehand to maximise their surface and improve the desiccation.

4.1.3 Summary

Using precipitation chemistry for the incorporation of fluorophores into PCL delivered adequate results in microscopy for DiOC18 and Rhodamine B. The mentioned concentrations of the dyes in the raw materials do not necessarily have to be accurate because this way of preparing them can cause parts of the fluorophores to wash out. Furthermore, while the drying process has been adapted and allowed a sufficiently good fibre deposition, residual solvents can have an impact on the coaxial MEW process.

In order to determine the exact dye concentrations and amounts of solvents nuclear magnetic resonance spectroscopy or mass spectrometry in combination with a gas chromatograph can be helpful. Moreover, the way in which different types and concentrations of the dyes affect the coaxial print offers a variety of further investigations.

4.2 Processing fluorophore-loaded PCL in uniaxial MEW

The previous sections described a way of mixing fluorescent dyes with PCL using precipitation chemistry while ensuring an even distribution as well as a proper drying. The next sections will discuss the processing of the filled polymer components in terms of their heat stability and the resulting fluorescence as well as their printing behaviour compared to neat PCL.

4.2.1 Heat stability of the fluorescent dyes

The MEW process works with a very low flow rate, meaning that the materials are subjected to heat above the melting point of the polymer (typically in the order of 80 to 95 °C for PCL) and stay in their molten state for an extended period of time (typically in the order of hours). Therefore, it was important to ensure that the materials used would not degrade over time while being held at the standard system operating temperature.

The green dye that was investigated was DiOC18; although there was no data available regarding its decomposition temperature, DiO dyes with different chain lengths are known to be stable to approximately 200 ºC [121]. Table 2 gives an overview of the decomposition/ melting temperatures of different DiO types; the number in the name is equivalent to the length of the alkyl chain that is connected to the oxazole nitrogen atom.

Table 2: *Overview of the decomposition temperatures of DiO dyes with different chain lengths [121].*

Type	Decomposition/ melting temperature [ºC]
DiOC2	278
DiOC5	214-215
DiOC6	222-224
DiOC7	194-197

The data obtained from the literature presented in Table 2 [121] allowed the presumption that DiOC18 had a high enough decomposition temperature to withstand the process temperature. In order to demonstrate the thermal stability of DiOC18 over time, PCL fibres containing around 0.0011 wt% of the dye were fabricated via uniaxial MEW over defined 30 min intervals. A montage of the resultant fibres under the green fluorescent channel are presented in Figure 23. The mixture had been heated to approximately 95 ºC; the relatively high temperature for this study was chosen to correspond with an observed overshoot in the temperature control system of the coaxial nozzle. This heating effect for this system arrangement is discussed in greater detail in Section 4.3.2.5.

Since MEW works with a comparatively small material flow [45], it could be assumed that over time in several printing processes that this maximum recorded temperature would be experienced multiple times by the same parts of the material. For this reason, the stability of the dye was investigated under the most extreme conditions that the coaxial setup caused.

The first print was started after 60 minutes of heating in order to allow the polymer to be in a homogeneous melt state, the relevant fibre is shown in Figure 23A. Figure 23 B to Figure 23 F show the fluorescence of fibres with similar diameters printed at incremental 30 min periods, imaged using the same exposure time of 1200 ms that was found to be suitable for the fluorescence of the first fibre (Figure 23 A). The investigation shown was done by not having the MEW device running continuously but rather heating the material over the period mentioned and only starting the pneumatic feeding in 30 min intervals in order to additionally investigate possible agglomerate formation while the system was left in an idle state. As shown in Figure 23, the fluorescence of the fibres was visibly uniform, meaning that the holding time did not have a negative effect on the distribution of the dyes.

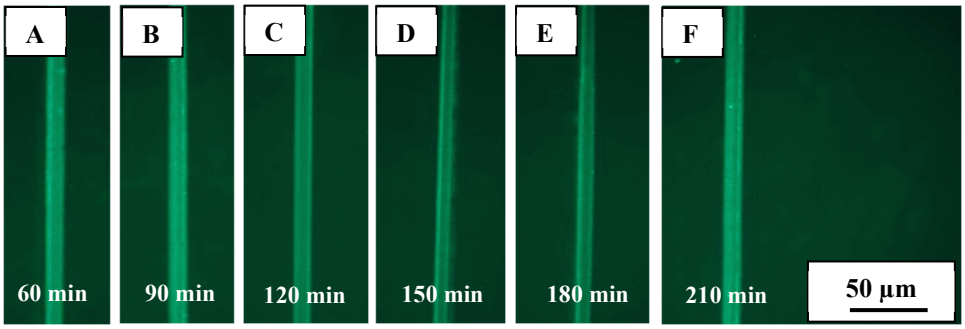

Figure 23: *Green fluorescence channel imaging of PCL fibres containing DiOC18 printed in 30 minute intervals starting after 60 minutes (A) while heating consistently with a heater temperature of 95 °C; exposure time: 1200 ms.*

As a contrast for the green dye, two different red fluorescent dyes were used in the MEW processes at hand as well, one of them being DiI. Irrespective of the concentration that was used, fluorescence microscopy from fibres made of PCL containing DiI resulted in an inadequate red signal. The dye has a decomposition temperature of 68 °C [121]; nevertheless, some substances can be processed above their temperature of thermal degradation for a short period of time [127]. In order to investigate the time frame for DiI-doped PCL a thermal stability study similar to that presented in Figure 23 was performed for PCL containing approximately 0.011 wt% DiI. The resulting dataset is presented in Figure 24.

Here, the use of a lower exposure time when compared to that used in the investigation on DiOC18 was possible due to an order of magnitude higher dye concentration. While the fluorescence is rather similar in Figure 24 A and B, there is a distinct and progressive loss of brightness following this (Figure 24 C to Figure 24 F) due to exposing DiI over an extended period to temperatures above its decomposition point of 68 °C.

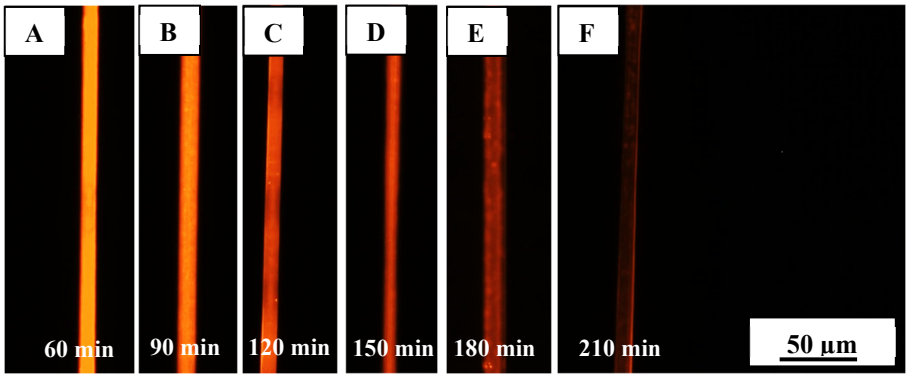

Figure 24: *Red fluorescence channel imaging of PCL fibres containing DiI that have been printed in 30 min intervals starting after 60 minutes (A) while heating consistently at a heater temperature of 95 ºC; exposure time: 812 ms.*

Rhodamine B was identified as an alternative for the red staining of the polymer in the following experiments. It has a decomposition temperature of 210 ºC [125]; its thermal stability was not investigated in advance due to this high value.

4.2.2 Examining the printing behaviour of fluorophore-loaded PCL in MEW

One important factor for the processing of different materials in MEW is the critical translation speed (CTS). The CTS was determined for the fluorophore-loaded materials in order to compare them to neat PCL. The Rhodamine-loaded fibres at increasing collector plate translation speeds are shown in Figure 25, its CTS was found to be 15 mm/s. The CTS for neat PCL was identified in a similar way and found to be 8 mm/s, the comparison of the values is presented in Figure 26A, alongside with the chosen MEW parameters (Figure 26 B).

As described by Reneker and Yarin for the use of salts in SES, the ions in the dye increased the electrical conductivity [35] of the melt and therefore caused a stronger acceleration of the jet while needing faster collector movements in order to allow the deposition of straight fibres with a decreased diameter. It has to be noted that it was not possible to apply air pressure to the materials continuously. Instead, the air pressure was applied for a short moment to allow a droplet formation at the nozzle tip that was then formed into a jet by the electrical potential. Nevertheless, voltage and gravity were not strong enough to allow a continuous fibre deposition with this approach: The pneumatic feeding system needed a manual 1 second pulse every approximately 30 seconds of operation, making this kind of investigation rather imprecise because this manual manipulation can lead to variations in the amount of material delivered. Furthermore, the average diameter of the PCL fibres was 8 µm, whereas the strong drag caused the Rhodamine-containing fibres to have diameters of around 13 µm. The additional material influenced the jet geometry and by that impacted its ability to spin, so it can be assumed that the discrepancy between the CTS values will even increase for fibres of the same size.

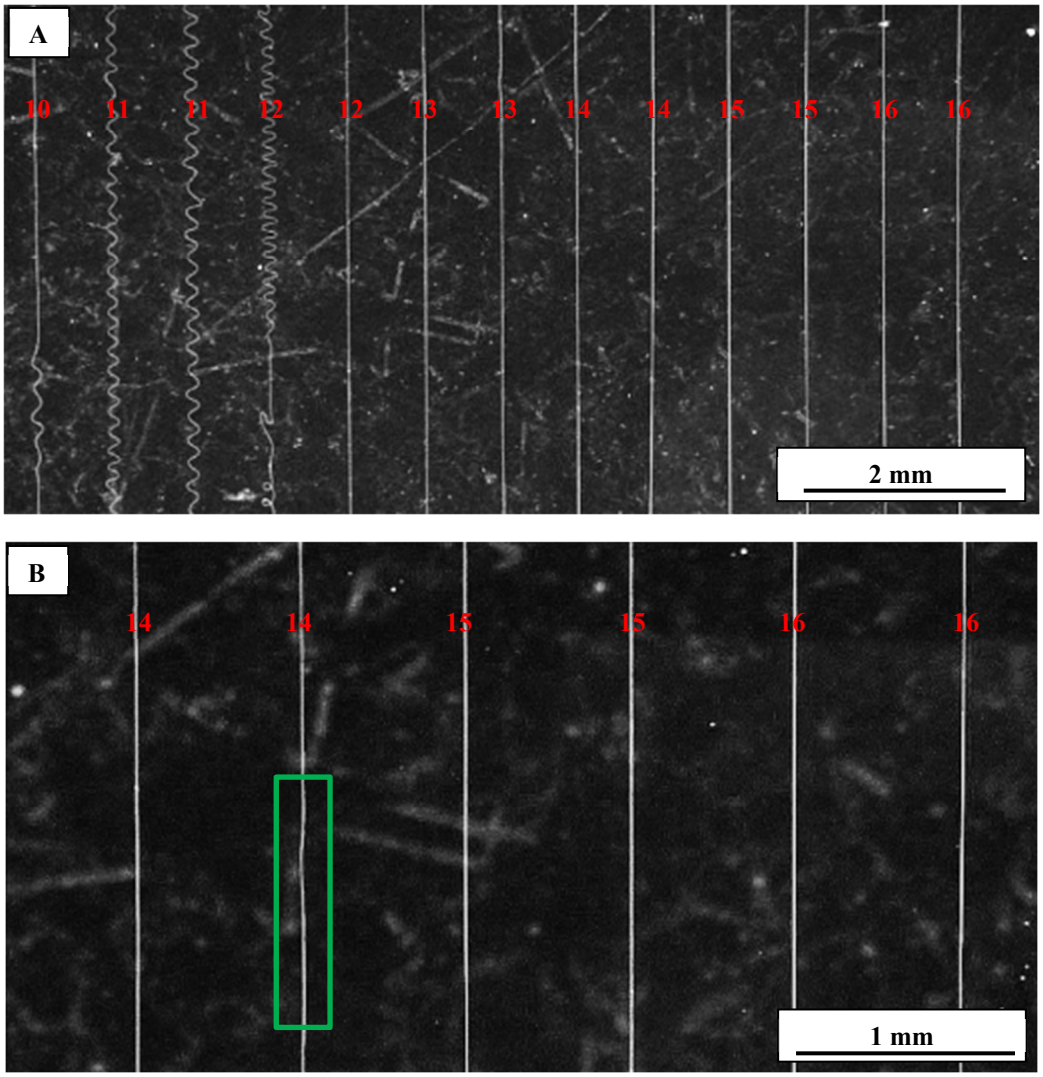

Figure 25: *PCL fibres containing Rhodamine B printed in the uniaxial setup, imaged with a stereo microscope in two different magnitudes with collector speeds (red numbers in mm/s) and spinning regions as well as barely visible instabilities (green box) for values below the CTS.*

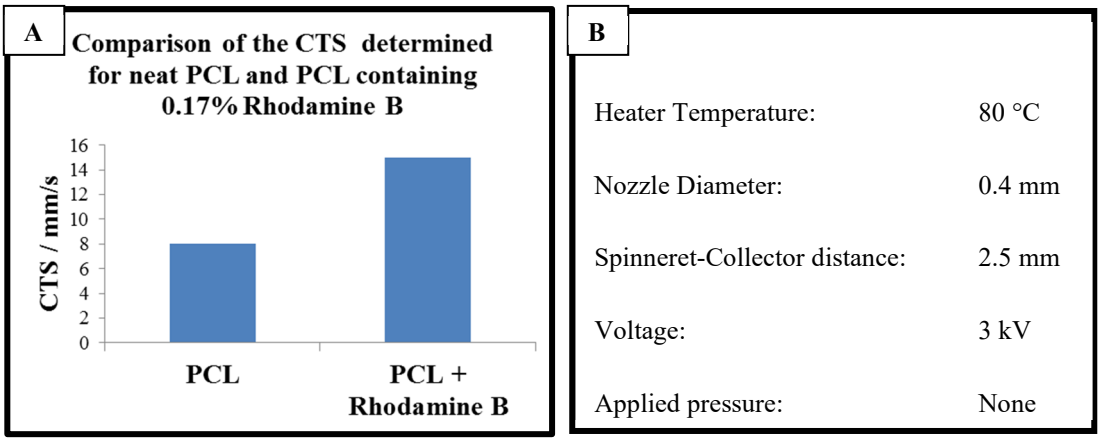

Figure 26: *CTS values for PCL and PCL containing 0.17 wt% of Rhodamine B (A), acquired in the uniaxial setup with comparable settings (B).*

4.2.3 Summary

This section has presented three potential dyes for use as visual indicators to be incorporated into PCL to allow for optical imaging of multi-material fibres to be produced through MEW. While DiI (Red) would provide a good colour contrast to DiOC18 (Green) under fluorescence microscopy and is widely used for biological characterisation it has a comparatively low decomposition temperature, which would lead to it being unstable over extended operating periods. For this reason, DiI was excluded and Rhodamine B was chosen as the red contrast dye for further studies.

By comparing the CTS of filled and neat PCL it was shown that this MEW-specific factor increases for PCL that has been loaded with fluorophores. Due to the fact that the dyes are salts this effect was expected, since salts are used in conventional SES to increase the conductivity of solutions and, with a more pronounced acceleration of the jet, decreasing the resultant fibre diameters. This change in the printing behaviour of dyed PCL will also be of importance in the following sections describing the coaxial MEW processing of PCL with different fluorophore percentages.

4.3 Processing fluorophore-loaded PCL via coaxial MEW

The uniaxial MEW processing of fluorophore stained materials has been described in Section 4.2. In the following section, the coaxial processing of materials with complementary stainings and their interactions will be presented.

4.3.1 Simultaneous detection of green and red fluorescent materials in MEW fibres

In order to see how the dyes respond to being exposed to their own optimum excitation and emission wavelengths, as well as to the wavelengths of the other dye, the dyed PCL has been printed individually while being in the coaxial nozzle, containing approximately 0.17 wt% Rhodamine B in the shell and 0.0011 wt% DiOC18 in the core syringes. These fluorescent fibres were investigated in confocal microscopy afterwards as shown in Figure 27. The images presented have been acquired under the exact same conditions, such as laser power and contrast settings for the different channels. Fluorophores have their optimum excitation and emission wavelengths but they can also show weaker signals while being exposed to wavelengths apart from their optimum values [128] and this explains why there was a weak signal visible in the green fluorescent channel for Rhodamine B (Figure 27 B).

This effect was mainly due to the high concentration of the dye that was necessary to get a sufficient red signal (Figure 27 A). Still, the green signal for the DiOC18-loaded PCL was comparatively stronger (Figure 27 D) and also there was no signal in the red channel at all (Figure 27 C). While the signal of the green dye is weaker compared to the signal of the red dye, it is still strong enough to be detected; and the difference in the behaviour of the two dyes with their respective concentrations in the different fluorescence channels is unique enough to tell the two materials apart, e.g. in a core-shell formation.

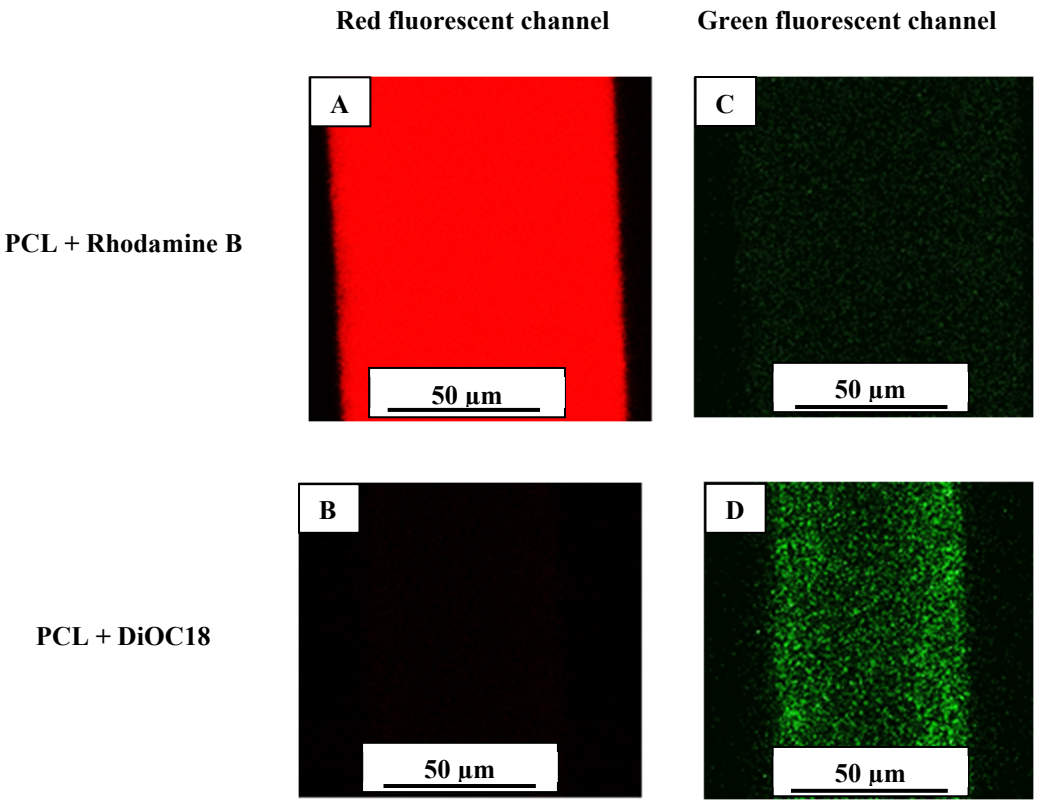

Figure 27: *Red (A and C) and green fluorescence confocal microscopy imaging (B and D) for fibres containing Rhodamine B or rather DiOC18, respectively.*

4.3.2 Concentric coaxial MEW process of PCL with different fluorophore loadings in the inner and outer syringes

In order to enable an unhindered melt flow it was important for the surface of the coaxial nozzle to be smooth [129]. After production via selective laser melting the nozzle underwent a manual 20 µm glass media blasting to remove any loosely bound surface particles. Following this process, the internal diameter of the nozzle orifice was cleaned and freed of any remaining particles or swarf using a 0.8 mm drill. The manual nature of these finishing processes led to small differences in the final orifice dimensions of the produced nozzles. Thus, the results of the following sections have been acquired with just one nozzle that was measured to have an outer diameter of 1.390 mm and an orifice size of 0.810 mm, as shown in Figure 28.

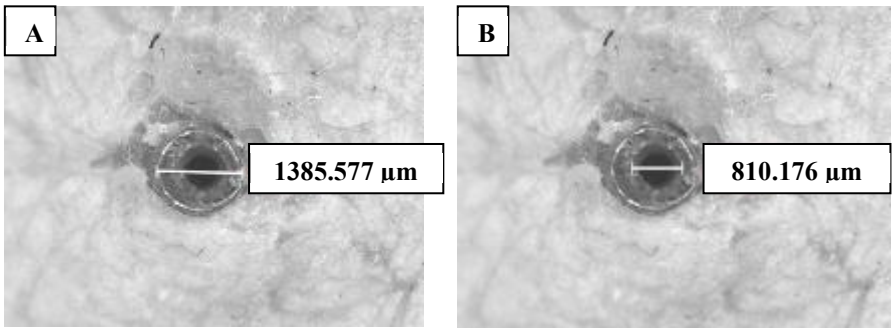

Figure 28: *Measurements of the nozzle tip dimensions with outer (A) and inner (B) diameters while being embedded in fireproof cement, images acquired with a stereo microscope.*

The coaxial nozzle was specifically designed for the insertion of a 26G needle, which was locked concentrically into the nozzle body. The expected arrangement of the melt under MEW conditions from the two connected syringe arrangements is depicted in Figure 29.

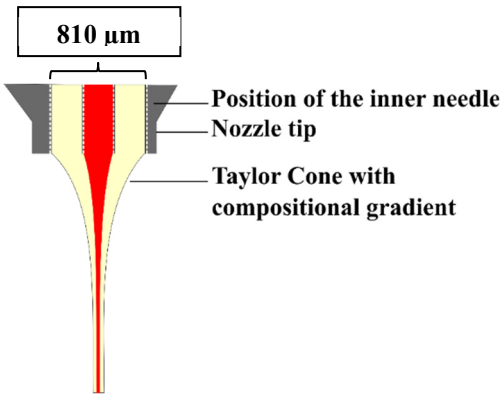

Figure 29: *Schematic representation of the presumed Taylor cone resulting from the concentric coaxial MEW setup.*

The necessity of inserting a needle for the coaxial setup explains the comparatively large inner diameter of the nozzle, which, at 0.81 mm, comprised approximately double the size of standard MEW spinnerets as described in the introduction.

4.3.2.1 Microscopy

As presented in Figure 29, the concentric setup of the inner needle and the nozzle connected to syringes filled with differently stained polymer components had been expected to most likely result in ultrafine core-shell structures with the outer material constituting a sheath around the core.

First attempts for the detection of the core-shell composition in the resulting fibres comprised using an inverted fluorescence microscope. However, by using confocal microscopy and looking at the cross-sections, it was found that the components in fact mixed instead of forming a core and a sheath. Figure 30 presents how the fibres – printed with neat PCL through the shell syringe and PCL stained with DiI through the core syringe – looked under the inverted fluorescence microscope. Figure 30 A shows the fluorescence that was detected for a fibre, which was focussed in a similar way as the brightfield image shown in Figure 30 C. A glowing of the whole fibre could be detected, which could have been caused by reflections from the fluorescent core into the surrounding sheath. By changing the focus slightly as shown in Figure 30 B, a smaller structure became visible that resembled a core that in Figure 30 D in an overlay of B and C makes the presumed core-shell structure apparent.

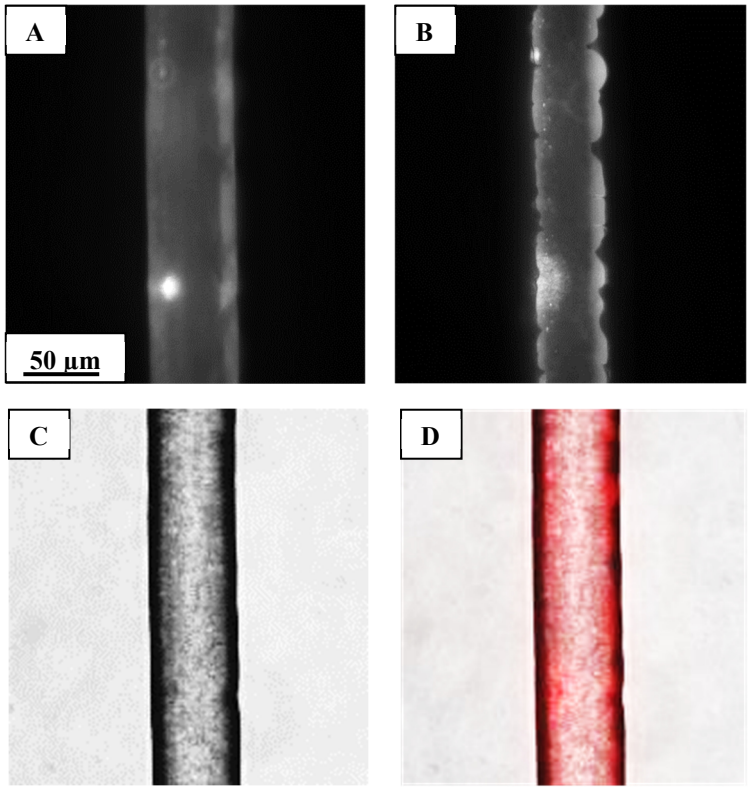

Figure 30: *Fluorescence microscopy of a fibre that has been printed coaxially with PCL in the sheath and PCL containing Rhodamine B in the core, according to previous investigations on the fabrication of core-shell fibres with the red fluorescence channel for the fibre in a different focal planes (A and B), the brightfield image (C) and an overlay of B and C (D); scale bar: 50 µm.*

Via confocal microscopy it was found that in fact the whole fibre must have been soaked with the dye, instead of just the core polymer containing the fluorophore. The fluorescent structure shown in Figure 30 B is therefore most likely the region where the fibre touches the glass slide; this also explains why the presumed core looks so sharp: With this kind of microscopy, depending on the focus there are always planes in the way that blur the image except for the region that is facing the objective [130].

An effect of mixing components in processes based on electrohydrodynamics was described by Marín and Lohse for increased applied voltages on combinations of water and glycerine [131]. Hence, the observed mixing was suspected to be a fundamental consequence of applying voltages to miscible melts. However, it was specified in the introductory section that the MEW process is reliant on a variety of parameters.

Therefore, multiple parameter variations have been examinedin order to investigate the mixing of the materials and the feasibility of core-shell structures. Table 3 gives an overview of the parameters that are known to affect the MEW process the most and that have been chosen for the analysis from the previous study [103]. These variations will be discussed in the following sections by varying one parameter and keeping the rest at fixed values.

Table 3: *Overview of the parameters used in previous investigations [103] that might have affected the fabrication of stable core-shell structures.*

Parameter	Values
Spinneret-collector distance	3 mm
Voltage	3 kV
Collector speed	10 mm/s
Pressure	Shell: 30 kPa, Core: 100 kPa
Heater temperature	80 °C
Fluorophore in PCL	0.00022 wt% DiI
Fluorophore-loading	Just core

4.3.2.2 Spinneret-collector distance and voltage

One parameter that was believed to have established the mixing was the distance between the nozzle and the collector, which could have been both, too high or too low. A too high distance can cause the mixing of the materials by allowing them to be together in their molten state for a longer period of time. A too low distance enhances the electrostatic dragging force as described by Brown [45], which possibly allowed the ions in the core material to overcome the insulating barrier of the sheath and mix with the shell. Figure 31 presents the jet at spinneret-collector distances of 1, 2 and 3 mm, respectively. Distances larger than 3 mm weakened the force of the accelerating voltage and the drag was not strong enough in order to collect fibres, distances lower than 1 mm caused an electrical arcing.

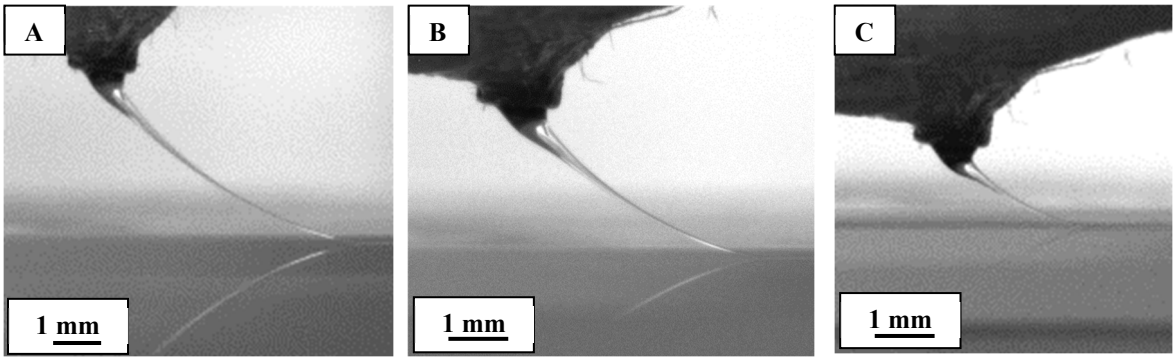

Figure 31: *Resulting jet in a coaxial MEW process with a voltage of 3kV, a collector speed of 10 mm/s, a core pressure of 100 kPa, a shell pressure of 30 kPa and a spinneret-glass slide distance of 3 (A), 2 (B) and 1 mm (C).*

Stable core-shell structures could not be achieved with a variation of the distance, the materials kept mixing. Similar to the spinneret-collector distance the voltage could have been too high or too low. Too high voltages have been shown to induce a mixing of materials by Marín and Lohse [131], too low voltages might destabilise the jet and the cone formation, especially at high molecular weights, as explained by Lyons *et al*. [59]. Voltages between 3 and 4 kV were tested since lower voltages prevented the fibres from sticking to the collector and higher voltages caused an electrical arcing; a mixing of the materials was discovered regardless of the value of the applied voltage. Figure 32 shows pictures of the jet at 3 (Figure 32 A) and 4 kV (Figure 32 B). The drag for a voltage of 4 kV was just slightly stronger than for 3 kV – which can be seen in the calculated lagging distances in Figure 32 – and did not result in a more stabilised jet.

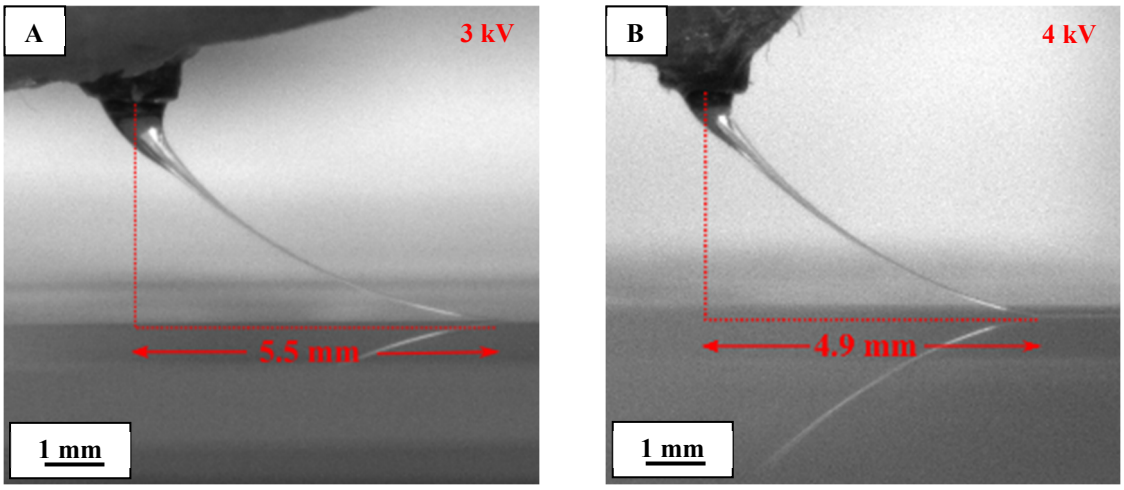

Figure 32: *Resulting jet in a coaxial MEW process with a spinneret-glass slide distance of 3 mm, a collector speed of 10 mm/s, a core pressure of 100 kPa, a shell pressure of 30 kPa and voltages of 3 (A) and 4 kV (B) and the resulting lagging distances (red) of the jet that have been estimated in relation to an outer nozzle diameter of 1.390 mm.*

4.3.2.3 Collector Speed

The collector speed is of major importance for the MEW process: As explained in the introduction, above the CTS the production of straight and defined structures is enabled, by increasing the collector speed to even higher values the fibre diameters decrease due to mechanical stretching. For the coaxial setup, a CTS was not measurable, since even excessively low collector speeds of 1 mm/s did not lead to spinning tendencies in the jet. Zhou *et al.* have shown that the whipping motion is less pronounced in melts compared to solutions [51]. However, the determination of a CTS was shown to be possible and necessary in previous MEW studies [3, 24, 25, 67, 73, 132]. This effect found here is most likely due to the large orifice, which is approximately double the size compared to standard MEW setups, making the jet too thick to spin at low voltages.

It has been considered that in the present study a too high collector speed in combination with an uncontrolled movement of the cone might have had an impact on the mixing of the materials. However, even collector speeds as low as 1 mm/s did not result in core-shell structures.

The lowest possible diameter of the mixed fibres that did not cause a jet breakage and still allowed the fibre collection in a controlled way by applying air pressures for the core and shell of 100 and 30 kPa, respectively, especially in the regions where the direction was changed, has been achieved with a collector speed of 10 mm/s and was found to be 34 µm. Figure 33 shows how increasing the speed from 10 (Figure 33 A) to 40 mm/s (Figure 33 B) affects the fibre diameters (i) as well as the accuracy of the collection path (ii).

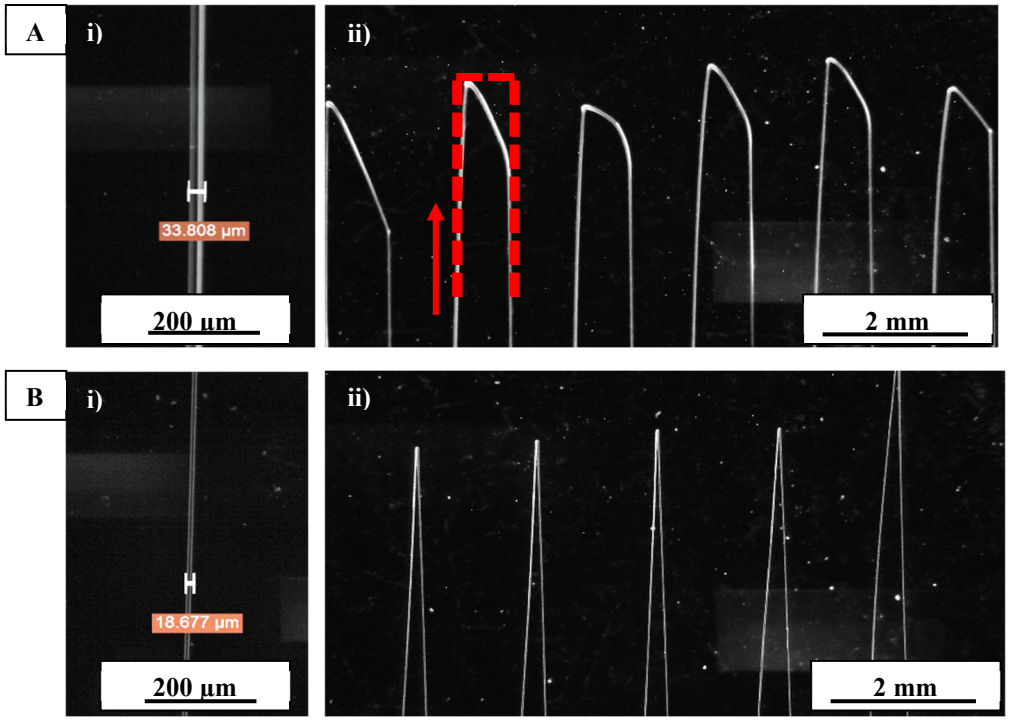

Figure 33: *Fibres (straight (i) and turning regions (ii)) collected at collector speeds of 10 (A) and 40 mm/s (B) with illustrated G-Code path and fibre collection path and direction (red).*

The G-Code for the fibre production was designed to have two 90º angles over a short distance in the direction change areas as indicated with red dotted lines in Figure 33. Due to the inherent lag of the jet behind the moving nozzle as described by Brown *et al.* [58], and demonstrated in Figure 32, this sharp angled shape is not practical to achieve in reality. Observations that the accuracy of fibre placement accuracy decreases with increased translation speeds have been presented by Hrynevich *et al.* [24]. This effect is evident in Figure 33 B where there is a four-fold increase in translation speed in comparison to the fibre recorded in Figure 33 A. The increased speed effectively led to a loss of printing resolution resulting in peak like contours, as opposed to the programmed right-angled turns, as the fibre did not have time to attach to the collector before the rapid change in movement direction.

The standard deviation for the diameters of mixed fibres was considerably higher than the deviation for fibres made of neat PCL, which supports the theory that the additional charges counteracted a controlled fibre deposition (compare Figure 34).

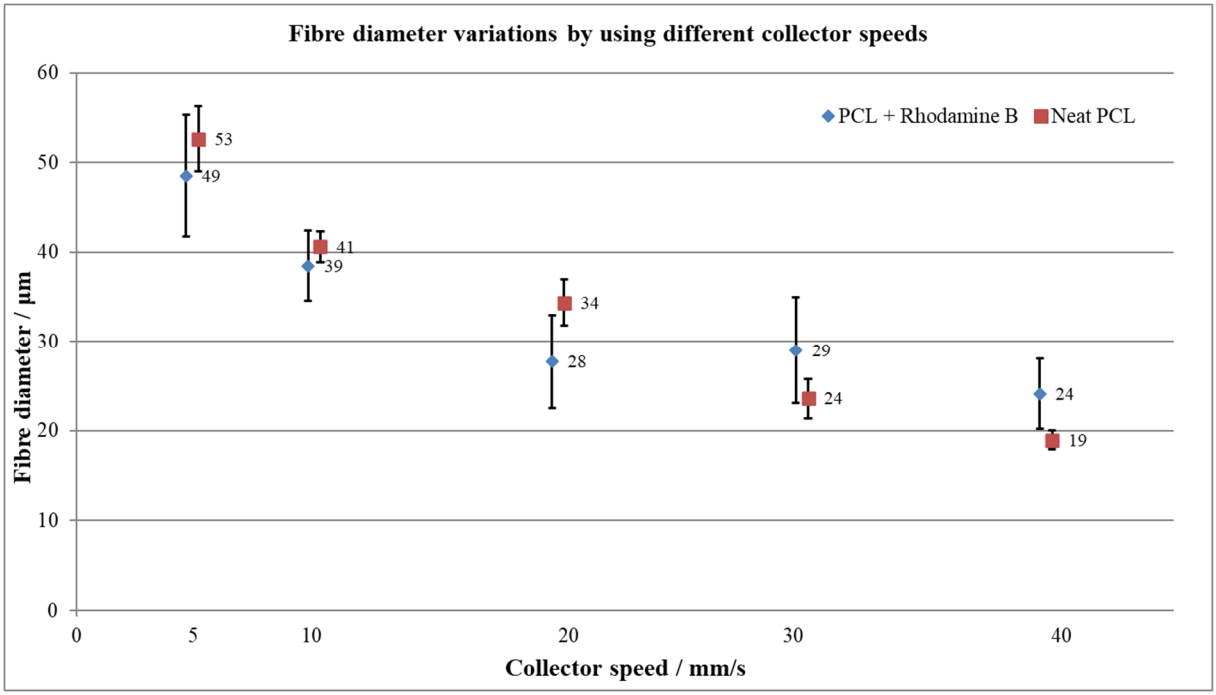

Figure 34: *Average fibre diameters at fixed process settings while changing only the collector speed for neat PCL and PCL containing Rhodamine B, as well as the standard deviations. The exact values of the measured fibres can be found in Appendix B, Table 7 and Table 8.*

4.3.2.4 Pressure

In order to find out whether there has been a cross-contamination of the core and shell materials inside of the nozzle already, a print was performed with the same parameters as used in the previous study (core pressure 100 kPa, shell pressure 30 kPa [103]). For this, the shell material was printed and stabilised first, allowing it to drag down the core material after its insertion. The outcome is shown in Figure 35, which is an overlay of the brightfield image and the red fluorescence channel under the fluorescence microscope.

Figure 35 A is a schematic of the fibre deposition with the extrusion onsets for the two materials. Figure 35 B presents the transfer between the stabilised prints that contained neat PCL from the outer syringe and the effect that the insertion of the fluorophore-loaded PCL from the inner syringe had. The evident increase in the fibre diameter was most likely due to the insertion of the core material that counteracted the prior stabilisation process. Figure 35 C shows the fully glowing fibres after stabilising the simultaneous print of the core and shell materials.

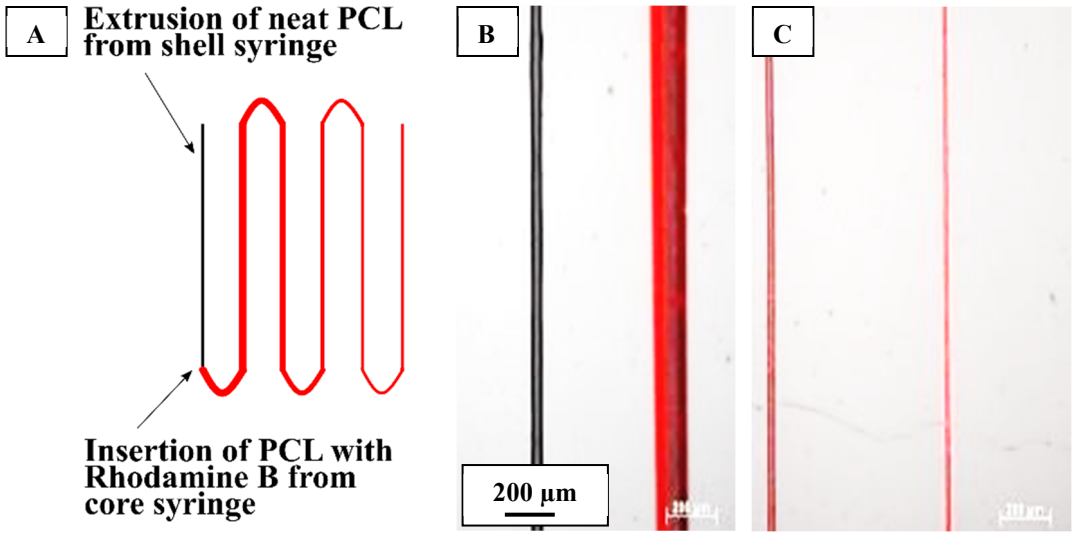

Figure 35: *Overlay of the red fluorescence channel and the brightfield image of fibres that have been printed coaxially according to previous investigations by stabilising the shell material at 30 kPa (neat PCL, A), then inserting the core material (PCL with Rhodamine B, B) with a pressure of 100 kPa, as well as the evenly coloured fibres after their stabilisation (C); scale bars: 200 µm.*

The order of material introduction was then changed so that the core material was initialised and printed first before adding the neat polymer from the outer syringe, which led to mixed fibres as well.

Different combinations for pneumatic pressures applied to the two syringes were investigated. Figure 36 presents two fibres that have been printed with an inner pressure of 50 and 100 kPa while keeping the outer pressure at 30 kPa. The investigation was done via confocal microscopy while using the exact same microscope settings such as laser powers and contrast settings for each of the fibres. With an increasing core pressure, the fibres get a slightly stronger signal in the fluorescence channel since there is an increasing amount of fluorophore uniformly mixing (compare the cross-sections ii) in Figure 36 A and B) with the neat polymer. Lower air pressures on the inner syringe such as 20 kPa resulted in insufficient fluorescence signals, a fact that is due to the lower amount of fluorophore that was allowed to mix with the neat material. However, since the concentration of the fluorophore was comparatively high, it can be concluded that there should have been a distinct signal in the core regions if it was not for a mixing of the materials.

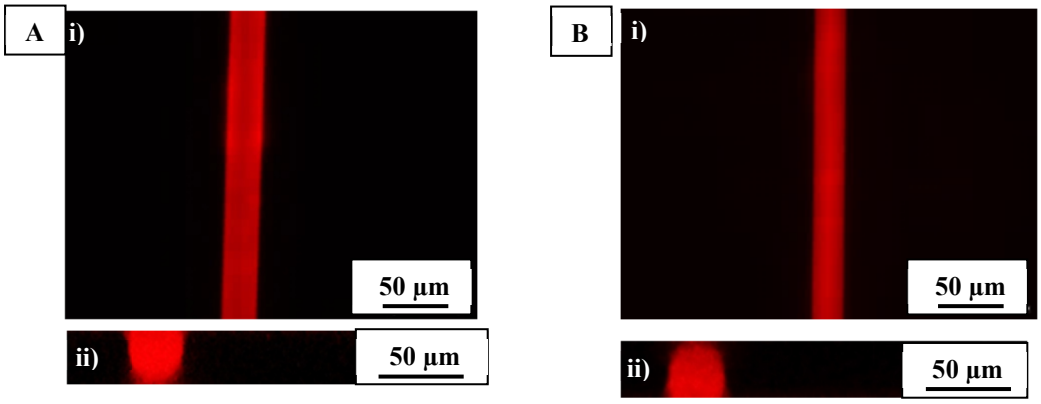

Figure 36: *Investigations on fibres printed with the coaxial nozzle while applying PCL with an air pressure of 30 kPa through the outer syringe and PCL containing Rhodamine B through the inner syringe with an air pressure of 100 kPa (A) and 50 kPa (B). The imaging was done with the red fluorescence channel on the top view of the fibres in confocal microscopy (i), also a cross-section was attained with a section thickness of 0.96 µm (ii).*

Figure 37 offers a comparison of the jets for an outer pressure of 30 kPa, while applying the fluorophore-loaded material with an inner pressure of 100 kPa (Figure 37 A) in contrast with the application of no inner material (Figure 37 B). Here, it is visible that by inserting the fluorophore-containing material into the jet the drag that is caused by the charged collector increased (Figure 37 A), which can be explained with the additional ions in the melt.

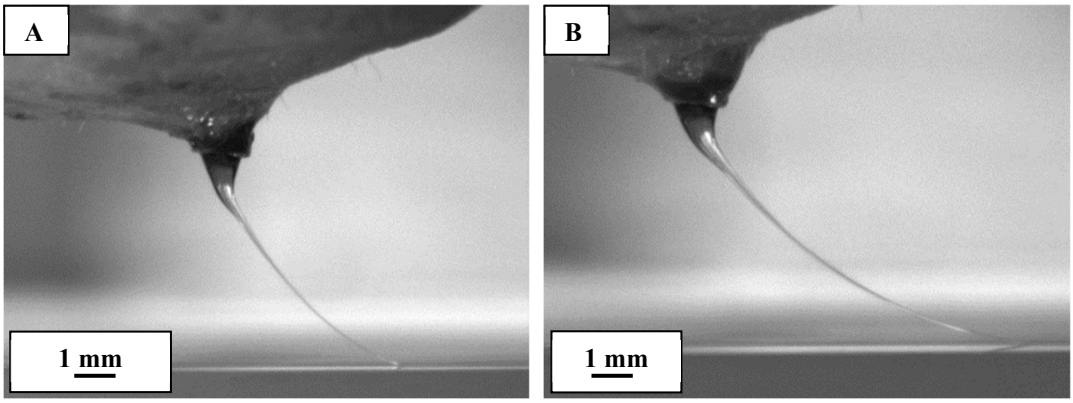

Figure 37: *Resulting jet in a coaxial MEW process with a spinneret-glass slide distance of 3 mm, a voltage of 3kV, a collector speed of 10 mm/s, a shell pressure of 30 kPa and a core pressure of 100 (A) and 0 kPa (B)..*

Figure 38 displays the changes in the diameters for fibres that have been printed with a fixed shell pressure of 30 kPa while varying the core pressure from 20 to 100 kPa. This approach allows the assumptions that with an increasing air pressure that is applied to the core syringe the fibre diameters increase, which can be explained with the higher mass flow. Nevertheless, by inserting the core material at a pressure of 100 kPa the average diameter actually seemed to decrease, which might be due to the stronger drag caused by the higher fluorophore concentration that the jet contains. It also has to be noted that the standard deviation in measured fibre diameter increases with an increasing amount of the dyed core polymer, leading to the assumption that the inconsistencies in the fibre diameters are provoked by the uncontrollable dragging that the accelerating voltage caused to the increasing amount of ions.

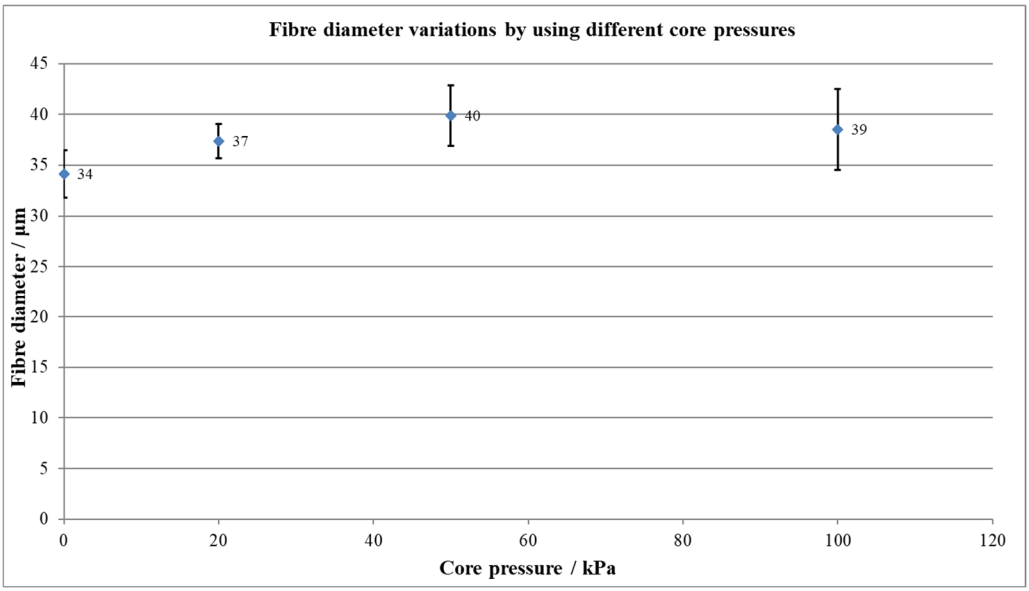

Figure 38: *Average fibre diameters at fixed process settings while changing only the core pressure, as well as the standard deviations. The exact values of the measured fibres can be found in Appendix B, Table 5.*

As explained before, the size of the nozzle is considerably larger compared to standard MEW setups, leading to a thicker melt jet that is less likely to spin and showed a weaker Taylor cone formation. Hence, it has been hypothesised that a lower shell pressure could overcome the mixing effect by having a more stabilised cone and less movement, especially in the regions where the collector changes its direction.

Nonetheless, the two materials kept mixing, even by applying less material through the core syringe, which made the characterisation difficult due to an insufficient fluorescence signal. It has also been tried to use a higher pressure for the shell material to surround the charges in the core with a thicker insulating barrier. However, the materials mixed.

An overview of the fibre diameters that have been attained with different shell pressures while keeping the core pressure constant at 100 kPa can be seen in Figure 39.

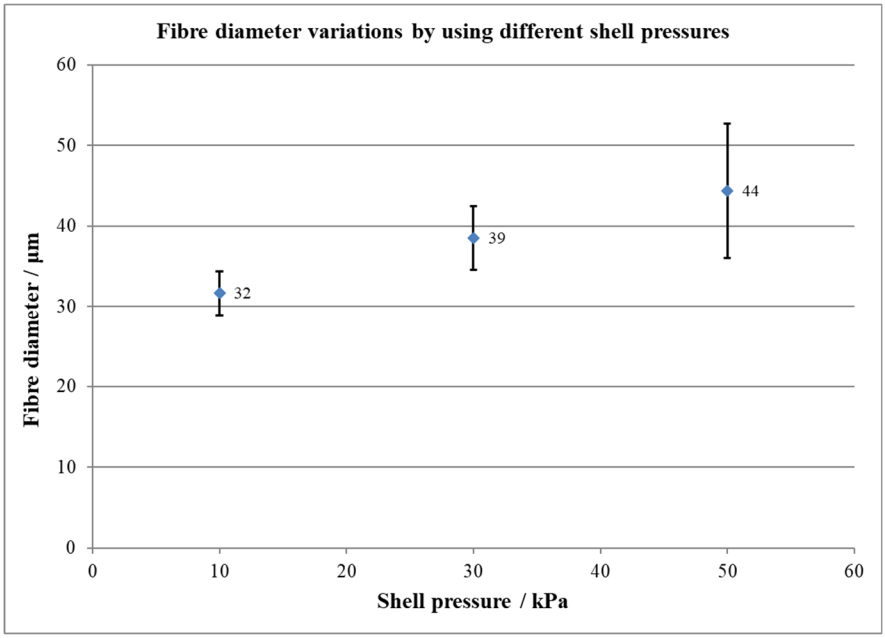

Figure 39: *Average fibre diameters at fixed process settings while changing only the shell pressure, as well as their standard deviations. The exact values of the measured fibres can be found in Appendix B, Table 6.*

Due to the higher mass flow, the average diameters of the fibres increased with an increasing pressure applied to the outer syringe. While it has been discussed before that a higher amount of fluorophore ions could have caused inconsistencies in the fibre diameters, this effect also occurred for fibres that have been printed with a high shell pressure of 50 kPa while keeping the inner pressure constant. Hence, the latter contained much less ions than fibres that have been attained with a shell pressure of only 10 kPa. This increase of the standard deviations could be explained with the presumption that the higher mass flow with less additional charges causes the outer electric field to have less impact on the jet.

4.3.2.5 Temperature

In order to allow a low enough viscosity of the polymer a heater temperature of 80 ºC was chosen for both, the heating of the nozzle and the syringe containers. The nozzle was embedded into fireproof cement, which has been done in order to provide thermal insulation. The heater demanded a stabilisation time of approximately 5 min to reach the set temperature, so a significant overshooting for the nozzle was detected at the beginning of the heating process. Figure 40 shows the temperature profile of the nozzle that has been heated up to 80 ºC for 25 minutes with the measured temperature varying from 78 to 97 ºC (Figure 40 A), as well as the temperature profile for the heating of the block (Figure 40 B). The latter has been found to be more consistent; this is most likely due to the fact that it is made of aluminium, which has a good thermal conductivity [133] and therefore has been expected to be more efficient than the cement. Also, the block contained much more thermal mass compared to the fire cement embedding, which leads to having an improved storing of the heat [134]. Except for the overshooting at the beginning the nozzle temperature got stabilised to the greatest possible extent and varied between 78 and 82 °C, which was managed by adjusting the embedding procedure as presented in Appendix B.

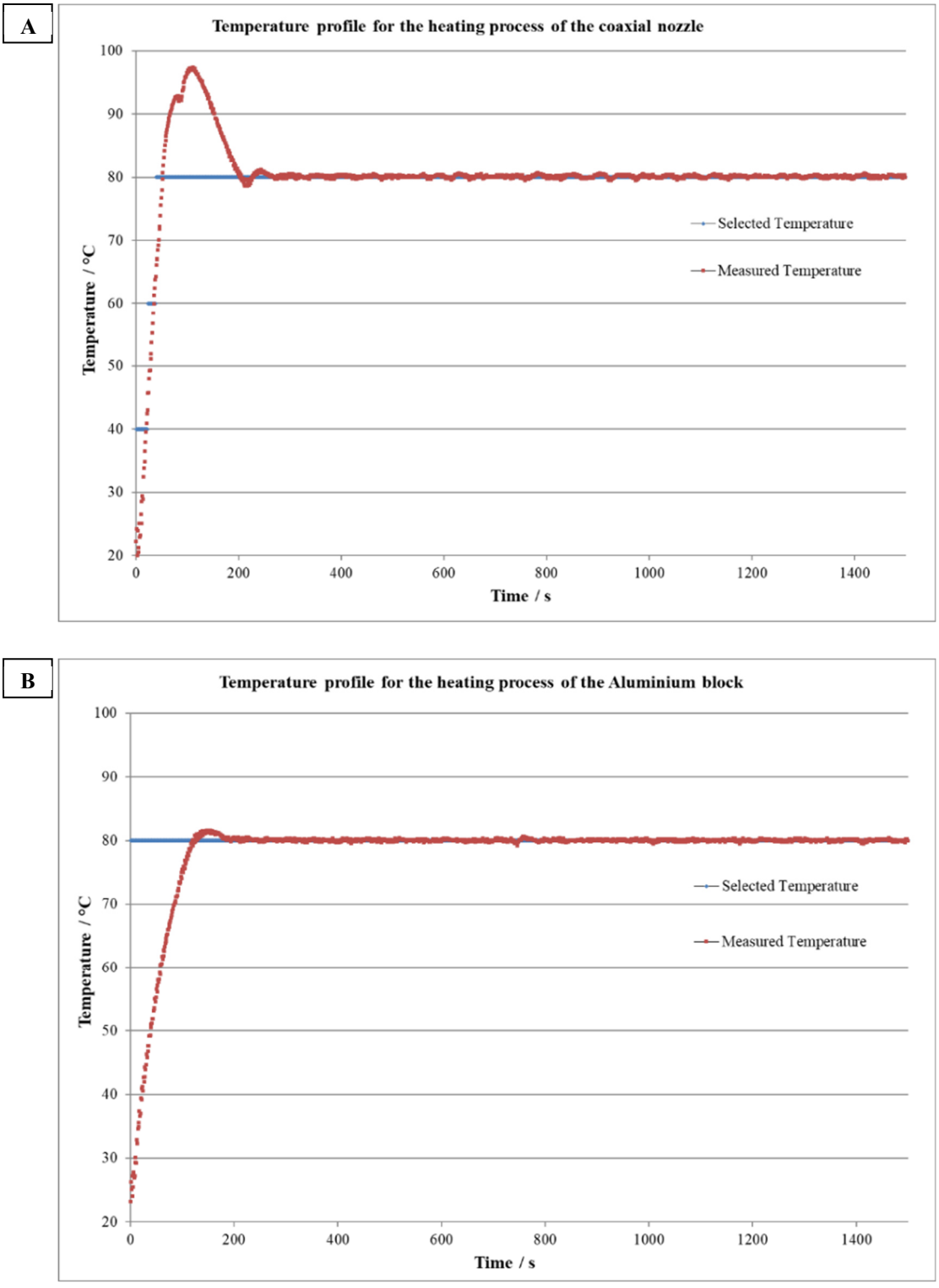

Figure 40: *Progression of the set (blue) and measured (red) temperatures during the heating of the coaxial nozzle (A) and the heating block (B).*

In Section 4.2.1 only the heat stability of the dyes was investigated. While many polymers are prone to a thermal degradation, which means a change in viscosity due to chain scission while being exposed to heat and strain, PCL is known to retain consistent properties, especially with an increasing chain length as investigated by Pitt *et al.* [135].

It has been considered that the viscosity was the reason for the mixing of the materials. Compared to SES, the viscosity of melts is considerably higher, hence the comparatively higher mass flow presumably established a certain amount of inertia towards a stabilisation of the Taylor cone. By this, a mixing of the materials inside of the cone could have been enabled, especially when the collector changed its direction. However, using a heater temperature of 120 °C did not prevent the materials from mixing.

At the same time, it was possible that the melt temperature could have been too high instead, preventing the shell material from cooling down quick enough to be a barrier for the core material. Using a heater temperature of 70 °C led to having a temperature of only 61 °C at the exposed nozzle tip, which is quite low for the extrusion of PCL. Still, it was possible to get a stable print out of this with a mixing of the materials.

4.3.2.6 Fluorophore loading

In the previous study it was only the core that has been loaded with DiI [103]. Multiple variations of the fluorophore types, their concentrations and their application to either the core or shell syringes were tested as shown in Table 4, which also gives an overview of the resulting difficulties regarding the detection of the fluorescence.

Table 4: *Overview of fluorophore concentrations and combinations in the coaxial setup up.*

Shell	Core
Rhodamine B (0.17 wt%)	PCL
PCL	Rhodamine B (0.17 wt%)
Rhodamine B (0.17 wt%)	DiOC18 (0.0011 wt%)
Rhodamine B (0.017 wt%, almost no signal)	DiOC18 (0.0011 wt%)
PCL	DiOC18 (0.0011 wt%)
DiI (different c, almost no signal)	DiOC18 (different c, sufficient signals)

It was not possible to attain core-shell structures in a reproducible, consistent way for either of these material combinations. Still, occasionally there were regions visible that resembled core-shell formations before being mixed completely. This happened for example by using a combination of DiI and DiOC18 with concentrations in the same magnitude (around 0.022 wt%), which is shown in Figure 41.

There was insufficient fluorescence signal for the outer material, as a result of thermal degradation of DiI as shown in Section 4.2.1. For this reason, the contrast settings for the red channel were set to relatively higher values, which caused a strong background noise (Figure 41 B) but also allowed a colouring of the shell in the overlay (Figure 41 D) of the two fluorescent channels and the brightfield image (Figure 41 C). A fading core structure is perceptible in the green channel (Figure 41 A); nonetheless, a spreading of the core material into the shell was visible, which in the consecutive printing process led to a full mixing of the materials as shown before.

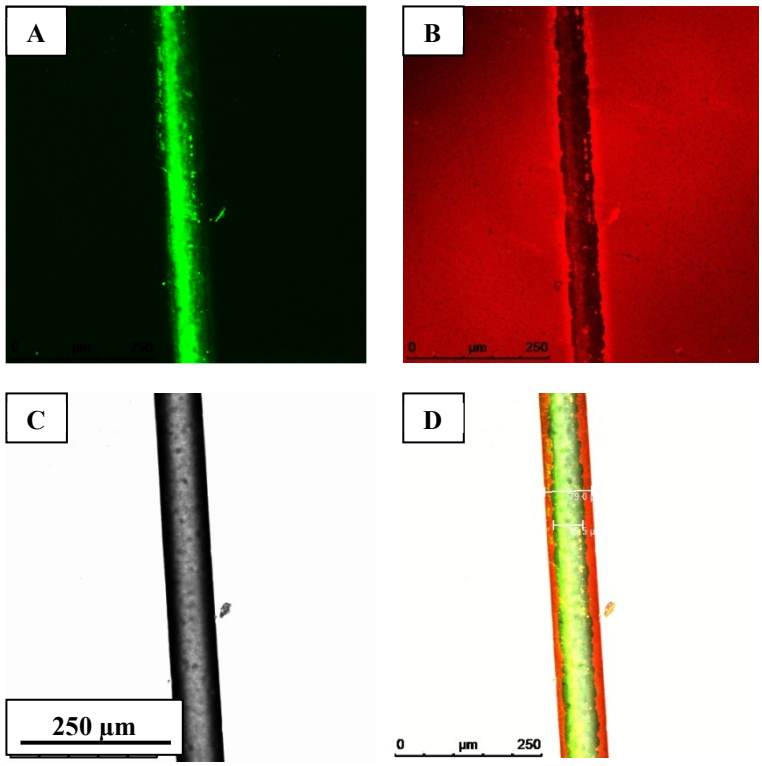

Figure 41: *Confocal microscopy imaging of fibres containing DiI and DiO with the green (A), red (B) and brightfield image (C) as well as the overlay of all 3 channels (D).*

4.3.3 Displaced coaxial MEW process of PCL with different fluorophore loadings in the inner and outer syringes

In initial printing tests, the nozzle and needle were aligned in the x/y plane in order to allow concentricity, as well as in the z plane. An offset in the z plane was tested by cutting the nozzle, making the needle protrude out slightly. Offsets with a value of 0.1 and 0.2 mm have been tested and did not result in core-shell structures but a mixing instead. The fully aligned nozzle and needle can be seen in Figure 42.

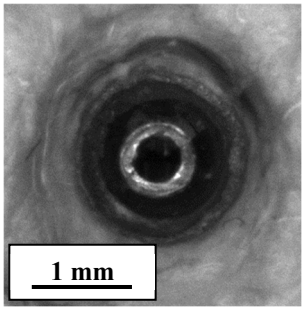

Figure 42: *Concentric alignment of the coaxial nozzle and the 26G needle.*

Also, a displacement of the needle in the x/y plane as shown in Figure 43 A has been investigated, although this has not been done for the investigation on core-shell fibres but Janus fibres instead. The nozzle has been designed with internal support structures in order to guarantee a concentric alignment. Still, this support cannot compensate for slight bends in the needle that enable the fabrication of gradient fibres. Figure 43 B shows a schematic of the Taylor cone that is presumed to be involved in the production of Janus fibres.

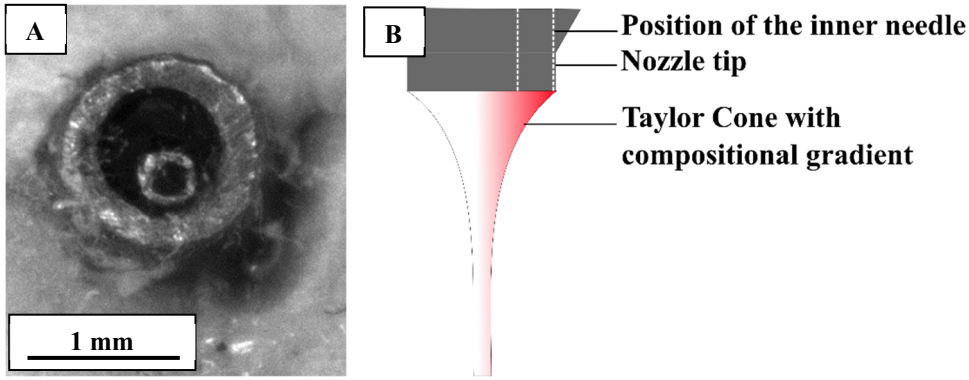

Figure 43: *Nozzle and needle position for the production of Janus structures (A) and a schematic of the resulting Taylor cone (B).*

Figure 44 displays a Janus fibre that has been attained with an outer pressure of 30 kPa (neat PCL) and a pressure of 100 kPa applied to the inner needle (PCL with Rhodamine B). A distinction between dyed and undyed regions is visible (red and blue arrows) and the overall composition differs from the microscopic imaging of fully mixed fibres as shown before. It can be assumed that the electrical potential that affected the additional charges in the dyed material – which is now close to the surface of the cone – generated a stabilising force by causing a strong drag on the dye and preventing the ions from immediately infiltrating the neat polymer in its entirety.

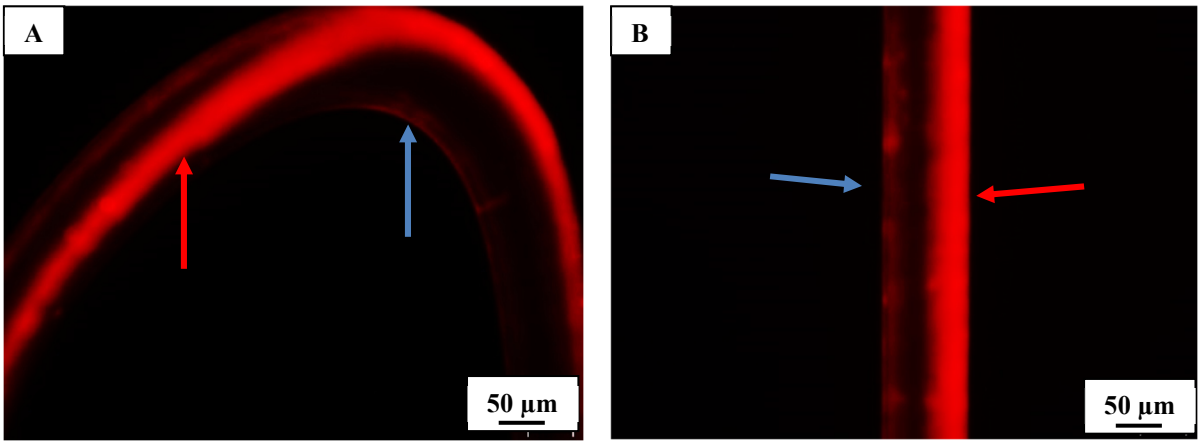

Figure 44: *Janus structure with direction change (A) and straight regions (B) in a fibre that has been fabricated with a displacement of the inner needle, applying an outer pressure of 30 kPa and an inner pressure of 100 kPa to syringes containing neat PCL and PCL containing Rhodamine B, respectively. The arrows mark the borders of the fibre parts containing neat PCL (blue) and dyed PCL (red).*

Due to the way the collector moved, the fluorescent material kept being located on one side of the straight regions and in the direction changes of the collector it was dragged across the fibre, which is indicated in Figure 44 A. The feasibility on Janus structures was also reproducible for a coaxial print of PCL containing two different dyes as shown in Figure 45.

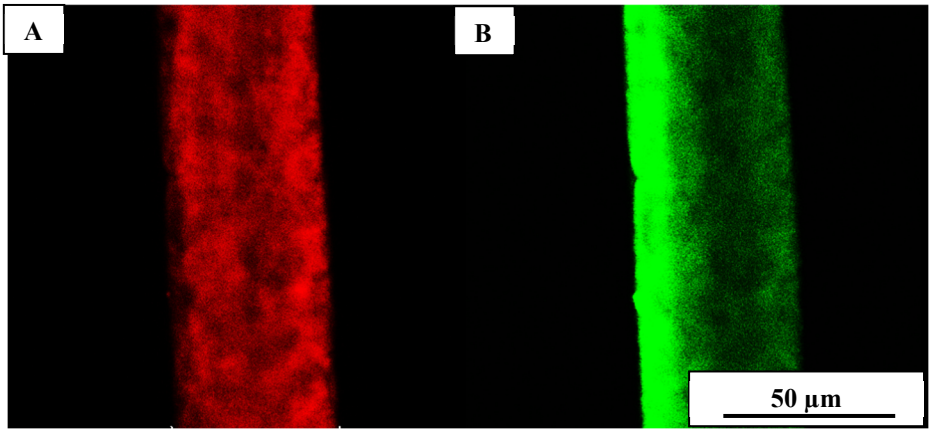

Figure 45: *Janus structure in a fibre that has been fabricated with a displacement of the inner needle, applying an outer pressure of 30 kPa and an inner pressure of 100 kPa to syringes containing neat PCL containing Rhodamine B and PCL containing DiOC18, respectively. The straight fibre has been made visible in the red (A) and green channel (B) using confocal microscopy.*

Compared to earlier confocal microscopy investigations on PCL containing the same amount of DiOC18 the fluorescent signal in the green channel (Figure 45 B) is much stronger. The high concentration of Rhodamine B has already been discussed to cause a low amount of green signal and it can be concluded that in the presented fibre the weak green glow of Rhodamine B and DiOC18 are adding up, resulting in a much stronger green signal.

However, this distinction of the materials was not stable, it was found that in different printing processes after a few lines the fibres were mixed again, as shown in Figure 46, leading to the assumption that the stabilisation by the ions cannot overcome the movements in the cone region.

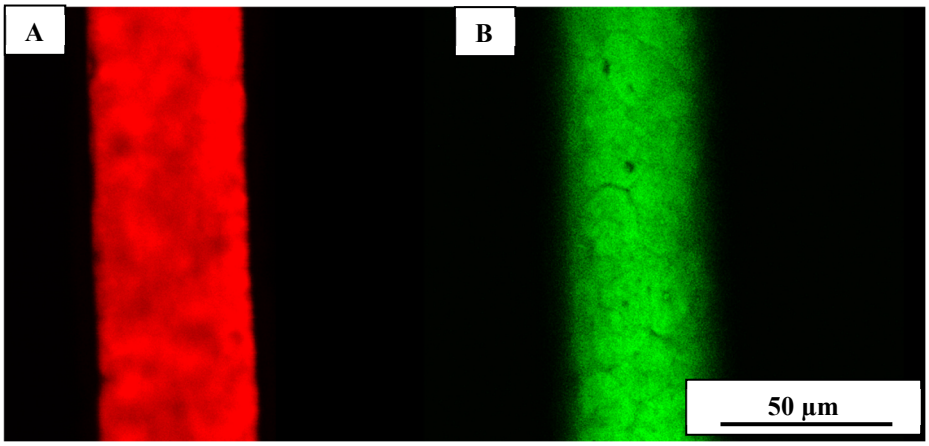

Figure 46: *Mixed structure in a fibre that has been fabricated with a displacement of the inner needle, while applying an outer pressure of 30 kPa and an inner pressure of 100 kPa to syringes containing neat PCL containing Rhodamine B and PCL containing DiOC18, respectively. The straight fibre that shows a mixing has been made visible in the red (A) and green channel (B) using confocal microscopy.*

4.3.4 Concentric coaxial MEW process of PCL in only the outer syringe

The effects that occur during the coaxial MEW of two materials have been discussed in the previous sections. The following section focusses on printing just one material in the shell, while applying air through the core syringe. For this investigation a fully aligned geometry of the nozzle and 26G needle were used.

The air insertion (Figure 47 A) has been done by pulsing the applied inner air pressure since continuous pressures even as low as 1 kPa caused the jet to deform and break, as shown in Figure 47 B.

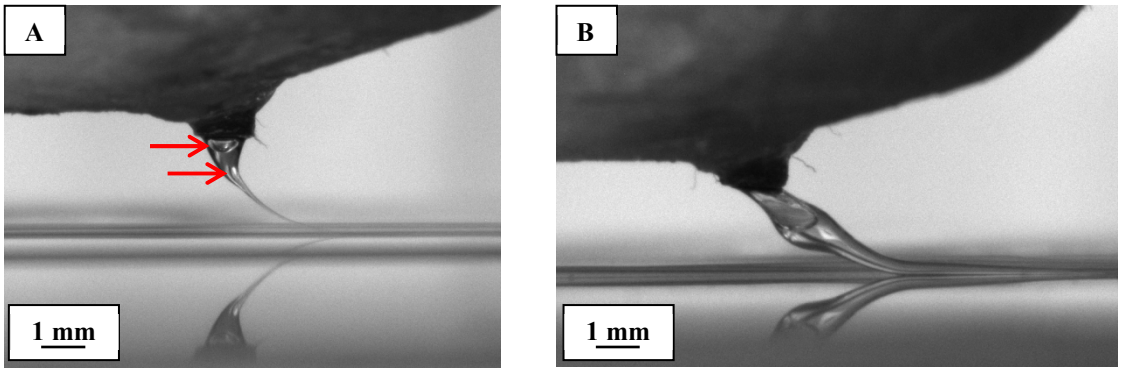

Figure 47: *Insertion on air into the jet (A) causing visible air bubbles in the melt (red arrows) and a jet breakage caused by a continuous appliance of air into the jet (B).*

Neat PCL was used as the sheath component, which makes the exact location of the hollow channel complex due to shadows in the brightfield imaging that caused the cross-section to become distorted as shown in later results. However, this approach was chosen in order to guarantee that the fabrication of hollow channels was not promoted by the additional charges of the dye ions.

While the insertion of air into the melt was reproducible it was not controllable yet, leading to having fibres with outer diameters as low as 10 µm with a channel size of 2 µm as well as outer diameters as big as 90 µm with a 25 µm channel as shown in Figure 48 A and Figure 48 B, respectively. The thick fibre in Figure 48 B could be detected using a 40X objective, for the thin fibre in Figure 48 A it was necessary to zoom, which explains the blurry edges. The variations in the diameters are most likely due to the pulsing of the air pressure and the aforementioned temperature variations in this setup that impacted the viscosity.

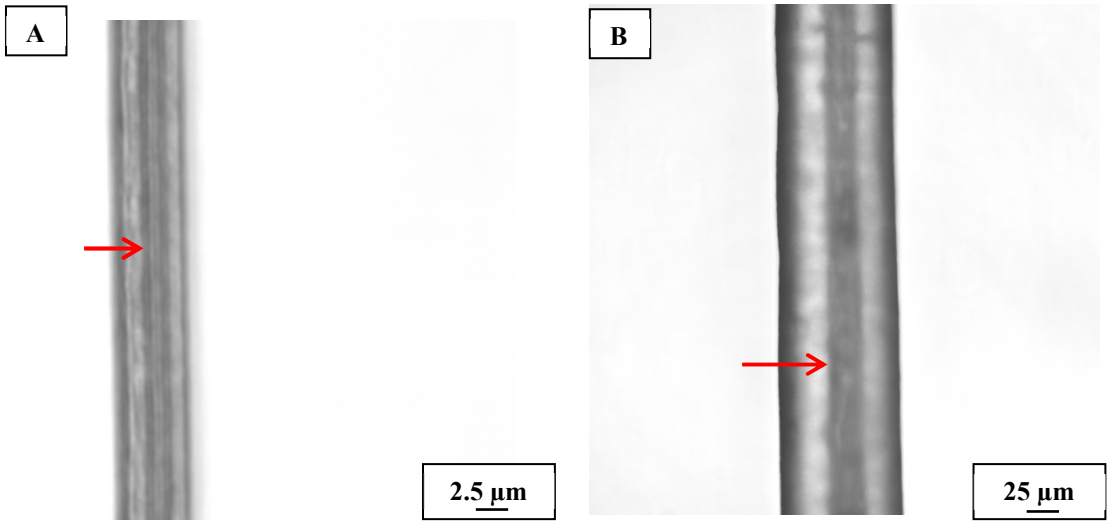

Figure 48: *Confocal microscopy brightfield imaging of hollow regions (red arrows) in fibres that have been fabricated with a shell pressure of 30 kPa while pulsing the core pressure at a value of 20 kPa.*

Also, the hollow regions could not be brought to a continuous level yet, instead hollow parts were followed by dense regions, as seen in Figure 49, which additionally caused variations in the fibre diameters.

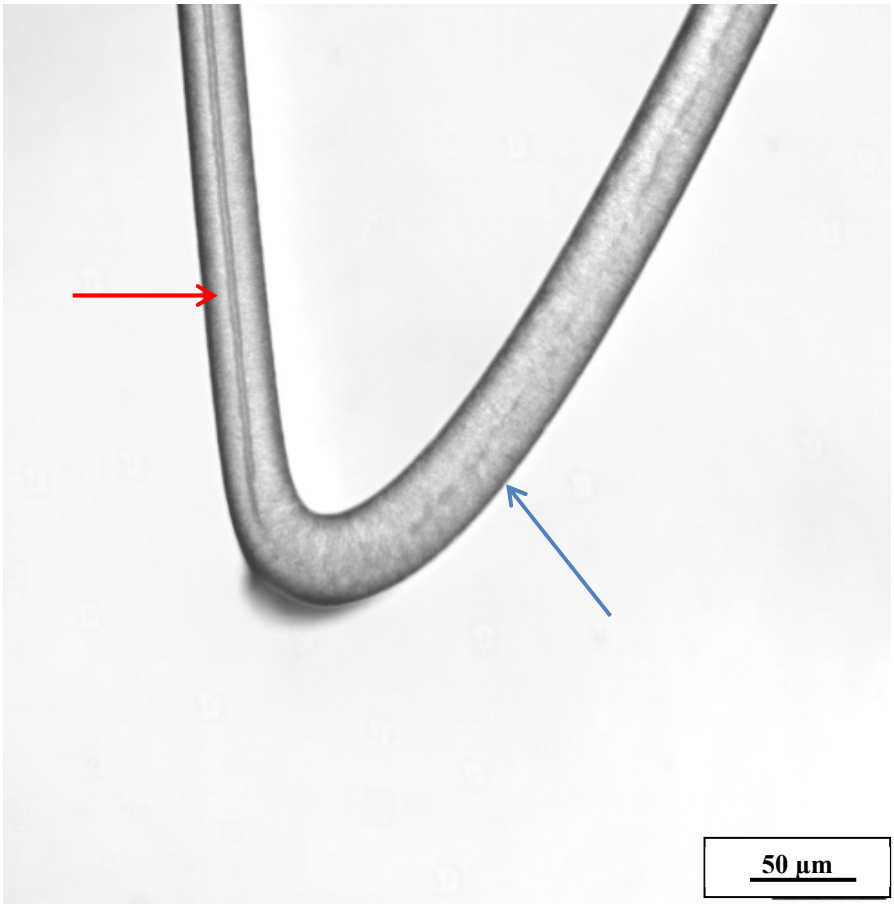

Figure 49: *Confocal microscopy brightfield imaging of a hollow region (red arrow) being followed by a dense structure (blue arrow).*

The characterisation of the exact location of the hollow channels in confocal microscopy using just the brightfield channel was not possible due to distortions in the cross-sections as shown in Figure 50.

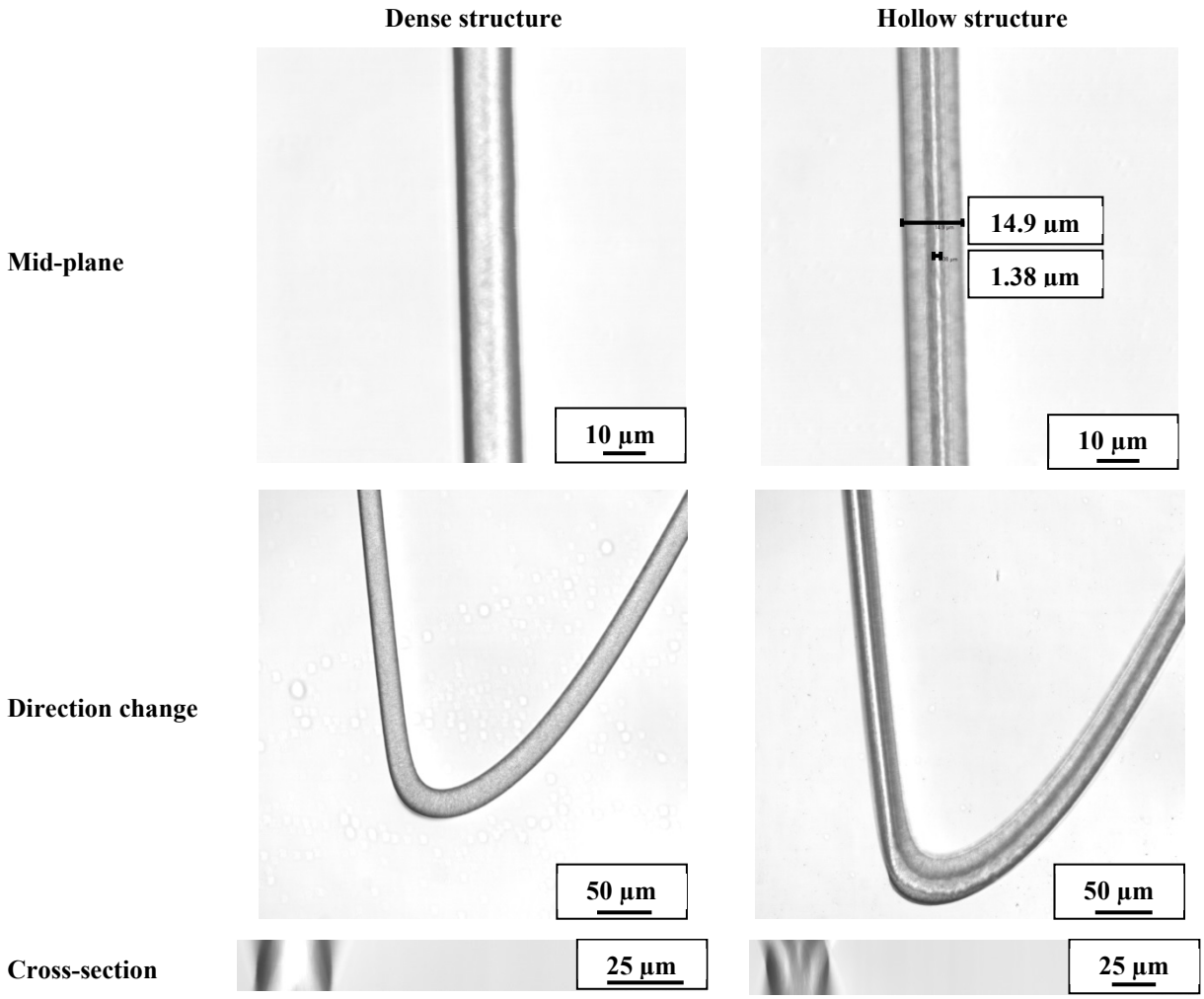

Figure 50: *Confocal microscopy brightfield imaging of hollow and dense regions in straight fibres, direction changes and the cross-sections with a section thickness of 0.25 µm for mid-plane, direction change and cross-section, respectively.*

By applying the air pressure for a longer period of time, it was possible to further inflate the Taylor cone as shown in Figure 51 A.

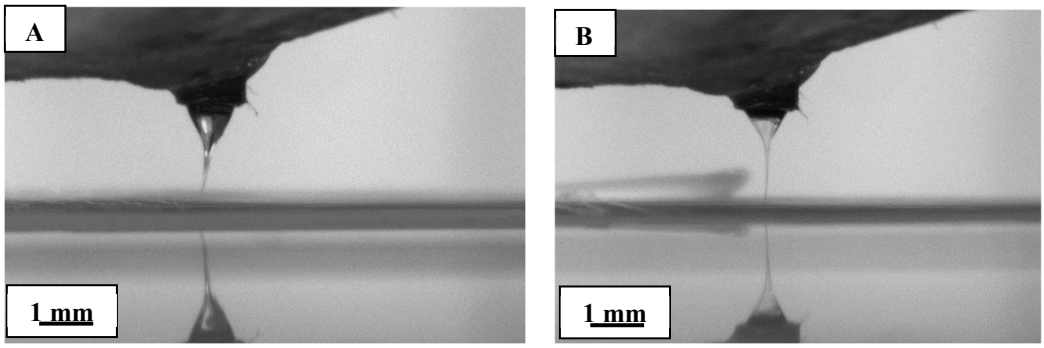

Figure 51: *Fully inflated Taylor cone (A) and the resulting cone geometry after the excessive melt was dragged down (B).*

After the excessive sheath material was dragged down, a different Taylor cone formation became accessible with a visibly low sheath and fibre diameter, as shown in Figure 51 B. This formation was stable over up to 5 straight lines (which equals a distance of approximately 25 cm) in the printing process before the next accumulation of dense material touched the collector. Here it has to be noted that the wall thickness was too thin to form continuous hollow regions over the mentioned distance covered, instead the structure collapsed quickly. Yet, it was this exact Taylor cone formation that allowed the fabrication of the 10 µm fibre that was shown in Figure 48 A.

In order to ensure the existence as well as the concentric location of the hollow region, which could not be determined via the confocal microscopic imaging shown before, additional SEM imaging was done on the cross-section of a fibre, which can be seen in Figure 52.

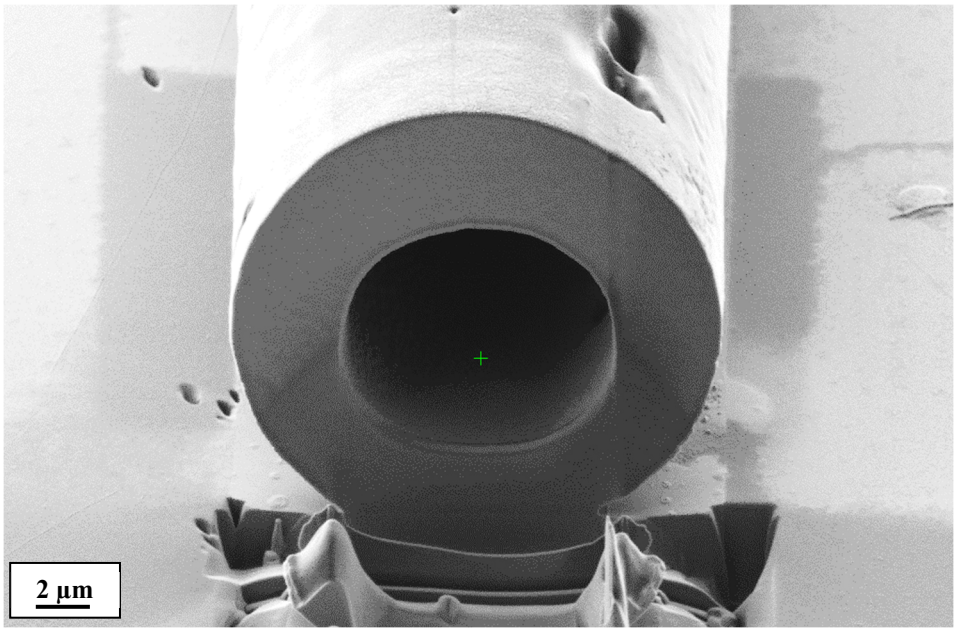

Figure 52: *SEM imaging of the cross-section of a hollow fibre showing a concentric alignment of the hollow channel and the sheath.*

4.3.5 Summary

A multitude of parameter variations have been performed in order to investigate the feasibility of core-shell structures in the coaxial MEW setup. It has been found through this body of work that variations in operating parameters did not prevent mixing of the core and shell materials. The most likely reason for this event is the comparatively high mass flow in combination with a high viscosity that causes the jet to develop an inertia towards a stabilisation by the external electric field and therefore induces the jet to move in the cone region rather than being still. Another aspect that needs to be taken into consideration is the electrohydrodynamics background of the MEW process, since other studies have shown a mixing of liquid components by just applying high voltages without any movement. Also, the nozzle geometry might have caused the two melts to develop a turbulent flow movement that caused the mixing. It is important to note that while the temperature variations for the heating of

the coaxial nozzle could be minimised, they were still present and might impact the viscosity of the melts in a way that counteracts the attempts of fabricating fibres with continuous compositions. It should be considered to switch to a more accurate heating element that does not cause overshooting, such as a proportional-integral-derivative controller. Also, the thermal insulation of the nozzle and the heating block should be adapted by using for example ceramics and high-performance plastics such as PEEK.

MEW is a 3D printing technique with an immense number of parameter combinations, allowing the assumption that core-shell structures might be possible under certain conditions, since they were also identified occasionally with the shown parameter variations. By changing the position of the inner needle and fixing it at the nozzle wall Janus fibres of the two materials became accessible; this was done by bending the needle slightly. Here, it has to be noted that these bends will cause a higher strain to the polymer while being extruded, which is why the given nozzle geometry might not be ideal for this kind of fibre fabrication since it may impact the flow behaviour of the melt. Also, the Janus structure was not exactly reproducible and in multiple attempts after a few lines of printing, the materials were mixed again.

When applying air instead of a second material into the sheath polymer, hollow fibres were shown accessible and reproducible. Usually, hollow fibres are attained by printing core-shell structures and later dissolving the core material away. This is necessary for applications such as FFF with a high mass flow in which the amount of molten material cannot be cooled down quick enough and by applying air to the surrounding material the structures will probably collapse rather than producing hollow structures. In SES, the viscosity is comparatively low, which leads to the assumption that by applying air pressure into the jet this will lead to its breakage. MEW fibres have a diameter that is sufficiently low enough to let the melt cool down quickly and also the viscosity of melts seems to be high enough to keep the air inside of the fibres.

5. Conclusions and Future Directions

Coaxial MEW has been shown to pose interesting opportunities such as the formation of core-shell, Janus and hollow fibres for the fabrication of novel multi-material structures with outer dimensions well below 100 µm. By using a custom-built coaxial nozzle connected to a prototyping pneumatically fed MEW system, challenges such different accelerations within materials containing conductive fillers as well as a mixing of coaxially processed PCL containing different fluorophores were observed. However, the accessibility of hollow channels in a one-step approach were substantiated as well as temporarily available Janus and core-shell structures.

The in-process-mixing of the materials could be interesting for polymers and composites that are prone to a thermal degradation and chain scission. If it is necessary to combine two materials for a desired use they could be spared the additional strain and high temperatures that would be caused by a compounding process before the printing. Also, by varying the flow rates during the print the fabrication of a gradient along the fibre becomes accessible. The further investigation of coaxial MEW should be done with separate heaters for the two syringes, which is also an approach that will probably become necessary for the successful printing of reproducible core-shell fibres from two different materials. If the mixing of the materials is in fact due to the electrohydrodynamics of the process, the employment of two dissimilar polymers that differ in their viscosities or chemical properties can be of interest. Another factor that should be looked into is the nozzle since its geometry might cause a turbulent flow of the two melt components. Hence, a re-design could be useful although an estimation of the melt behaviour using simulation techniques can be challenging due to too many unpredictable factors such as the electric field.

In order to achieve a reliable multi-material MEW process in further studies the following strategies are proposed:

First of all, filled materials should not be held in reservoirs at temperatures in excess of their melting point to avoid agglomeration. Additionally, a preparation of the process materials in a feedstock format such as filament can be of use in order to gradually melt the material. Also, for the coaxial fibre fabrication this would allow the geometry and composition of the filament being defined on a macro-scale using conventional melt extrusion processes, which would work for core-shell and Janus constitutions. Hence, the uniaxial MEW process would merely draw down the final intended coaxial structures such as core-shell or Janus. Furthermore, the use of a filament would enable the integration of readily available FFF hardware such as electrically isolated hot end systems and modified low speed stepper motor feed mechanisms. Hence, the feed-rate could be matched to the mass flow rate of the jet. This addition could limit process instabilities which result from variations in the pneumatic material supply method.

Second, for the coaxial formation of hollow channels the instabilities and variations in the fibre composition could be mitigated by controlled low volume continuous application of gas via a syringe pump mechanism. This approach would require balancing of the gas feed rate so that an initial pressure within a hollow cavity within the Taylor cone could be accumulated, and the feed rate subsequently reduced to match the volume of the hollow core.

6. References

1. Lee, S.J., J.J. Yoo, and A. Atala, *Biomaterials and Tissue Engineering*, in *Clinical Regenerative Medicine in Urology*. 2018, Springer. p. 17-51.
2. Ventola, C.L., *Medical applications for 3D printing: current and projected uses.* Pharmacy and Therapeutics, 2014. **39**(10): p. 704.
3. Brown, T.D., P.D. Dalton, and D.W. Hutmacher, *Direct writing by way of melt electrospinning.* Advanced Materials, 2011. **23**(47): p. 5651-5657.
4. O'brien, F.J., *Biomaterials & scaffolds for tissue engineering.* Materials today, 2011. **14**(3): p. 88-95.
5. Gholipourmalekabadi, M., et al., *Oxygen-generating biomaterials: a new, viable paradigm for tissue engineering?* Trends in biotechnology, 2016. **34**(12): p. 1010-1021.
6. Hutmacher, D.W., T.B. Woodfield, and P.D. Dalton, *Scaffold design and fabrication*, in *Tissue Engineering (Second Edition)*. 2015, Elsevier. p. 311-346.
7. Killi, S.W., *Additive Manufacturing: Design, Methods, and Processes*. 2017: CRC Press.
8. Tofail, S.A., et al., *Additive manufacturing: scientific and technological challenges, market uptake and opportunities.* Materials Today, 2017.
9. Chua, C.K., C.H. Wong, and W.Y. Yeong, *Standards, quality control, and measurement sciences in 3D printing and additive manufacturing*. 2017: Academic Press.
10. Bikas, H., P. Stavropoulos, and G. Chryssolouris, *Additive manufacturing methods and modelling approaches: a critical review.* The International Journal of Advanced Manufacturing Technology, 2016. **83**(1-4): p. 389-405.
11. Jones, R.A., *Soft condensed matter*. Vol. 6. 2002: Oxford University Press.
12. Malkin, A.Y., V. Goncharenko, and V. Malinovskii, *Barus effect in polymer flows through cylindrical and flat dies.* Polymer Mechanics, 1976. **12**(3): p. 439-444.
13. Brown, T.D., P.D. Dalton, and D.W. Hutmacher, *Melt electrospinning today: An opportune time for an emerging polymer process.* Progress in Polymer Science, 2016. **56**: p. 116-166.
14. Petcu, E.B., et al., *3D printing strategies for peripheral nerve regeneration.* Biofabrication, 2018. **10**(3): p. 032001.
15. Ramakrishna, S., et al., *Electrospun nanofibers: solving global issues.* Materials today, 2006. **9**(3): p. 40-50.
16. Pant, H.R., et al., *Fabrication of highly porous poly (ε-caprolactone) fibers for novel tissue scaffold via water-bath electrospinning.* Colloids and Surfaces B: Biointerfaces, 2011. **88**(2): p. 587-592.
17. Yoshimoto, H., et al., *A biodegradable nanofiber scaffold by electrospinning and its potential for bone tissue engineering.* Biomaterials, 2003. **24**(12): p. 2077-2082.
18. Abdal-hay, A., et al., *Electrospun biphasic tubular scaffold with enhanced mechanical properties for vascular tissue engineering.* Materials Science and Engineering: C, 2018. **82**: p. 10-18.
19. Zhang, S., *Fabrication of novel biomaterials through molecular self-assembly.* Nature biotechnology, 2003. **21**(10): p. 1171.
20. Nam, Y.S. and T.G. Park, *Porous biodegradable polymeric scaffolds prepared by thermally induced phase separation.* Journal of biomedical materials research, 1999. **47**(1): p. 8-17.
21. Pham, Q.P., U. Sharma, and A.G. Mikos, *Electrospun poly (ε-caprolactone) microfiber and multilayer nanofiber/microfiber scaffolds: characterization of scaffolds and measurement of cellular infiltration.* Biomacromolecules, 2006. **7**(10): p. 2796-2805.
22. AK S, S.P. and K. Chatterjee, *Fabrication of poly (Caprolactone) nanofibers by electrospinning.* J Polym Biopolym Phys Chem, 2014. **2**(4): p. 62-66.
23. Zein, I., et al., *Fused deposition modeling of novel scaffold architectures for tissue engineering applications.* Biomaterials, 2002. **23**(4): p. 1169-1185.
24. Hrynevich, A., et al., *Dimension‐Based Design of Melt Electrowritten Scaffolds.* Small, 2018. **14**(22): p. 1800232.
25. Hochleitner, G., et al., *Additive manufacturing of scaffolds with sub-micron filaments via melt electrospinning writing.* Biofabrication, 2015. **7**(3): p. 035002.
26. Li, D. and Y. Xia, *Electrospinning of nanofibers: reinventing the wheel?* Advanced materials, 2004. **16**(14): p. 1151-1170.
27. Nayak, R., *Review of Literature: Melt Electrospinning*, in *Polypropylene Nanofibers*. 2017, Springer. p. 9-39.
28. Ferreira, J.L., et al., *Electrospinning polycaprolactone dissolved in glacial acetic acid: Fiber production, nonwoven characterization, and in vitro evaluation.* Journal of Applied Polymer Science, 2014. **131**(22).

29. Zhou, F.L., R.H. Gong, and I. Porat, *Needle and needleless electrospinning for nanofibers.* Journal of applied polymer science, 2010. **115**(5): p. 2591-2598.
30. Basu, S., A.K. Agrawal, and M. Jassal, *Concept of minimum electrospinning voltage in electrospinning of polyacrylonitrile N, N‐dimethylformamide system.* Journal of Applied Polymer Science, 2011. **122**(2): p. 856-866.
31. Ghorani, B. and N. Tucker, *Fundamentals of electrospinning as a novel delivery vehicle for bioactive compounds in food nanotechnology.* Food Hydrocolloids, 2015. **51**: p. 227-240.
32. Leach, M.K., et al., *Electrospinning fundamentals: optimizing solution and apparatus parameters.* J Vis Exp, 2011. **47**.
33. Rayleigh, L., *On the capillary phenomena of jets.* Proc. R. Soc. London, 1879. **29**(196-199): p. 71-97.
34. Ki, M., et al., *Dye-Sensitized Solar Cells Based on Polymer Electrolytes: Solar Cells–Dye-Sensitized Devices, ed. LA Kosyachenko*. 2011, Intech Publications, Rijeka.
35. Reneker, D.H. and A.L. Yarin, *Electrospinning jets and polymer nanofibers.* Polymer, 2008. **49**(10): p. 2387-2425.
36. Clasen, C., et al., *'Gobbling drops': the jetting–dripping transition in flows of polymer solutions.* Journal of fluid mechanics, 2009. **636**: p. 5-40.
37. Hohman, M.M., et al., *Electrospinning and electrically forced jets. I. Stability theory.* Physics of fluids, 2001. **13**(8): p. 2201-2220.
38. Agarwal, S., J.H. Wendorff, and A. Greiner, *Use of electrospinning technique for biomedical applications.* Polymer, 2008. **49**(26): p. 5603-5621.
39. Zeng, J., et al., *Biodegradable electrospun fibers for drug delivery.* Journal of controlled release, 2003. **92**(3): p. 227-231.
40. Khil, M.S., et al., *Electrospun nanofibrous polyurethane membrane as wound dressing.* Journal of Biomedical Materials Research Part B: Applied Biomaterials: An Official Journal of The Society for Biomaterials, The Japanese Society for Biomaterials, and The Australian Society for Biomaterials and the Korean Society for Biomaterials, 2003. **67**(2): p. 675-679.
41. Uyar, T., et al., *Molecular filters based on cyclodextrin functionalized electrospun fibers.* Journal of Membrane Science, 2009. **332**(1-2): p. 129-137.
42. Hwang, T.H., et al., *Electrospun core–shell fibers for robust silicon nanoparticle-based lithium ion battery anodes.* Nano letters, 2012. **12**(2): p. 802-807.
43. Formo, E., et al., *Functionalization of electrospun TiO2 nanofibers with Pt nanoparticles and nanowires for catalytic applications.* Nano Letters, 2008. **8**(2): p. 668-672.
44. Khorshidi, S., et al., *A review of key challenges of electrospun scaffolds for tissue‐engineering applications.* Journal of tissue engineering and regenerative medicine, 2016. **10**(9): p. 715-738.
45. Brown, T.D., *Melt electrospinning writing*. 2015, Queensland University of Technology.
46. Dalton, P.D., et al., *Electrospinning of polymer melts: phenomenological observations.* Polymer, 2007. **48**(23): p. 6823-6833.
47. Joo, Y.L. and H. Zhou, *Apparatus and method for elevated temperature electrospinning*. 2008, Google Patents.
48. Hutmacher, D.W. and P.D. Dalton, *Melt electrospinning.* Chemistry–An Asian Journal, 2011. **6**(1): p. 44-56.
49. Yan, X., et al., *Portable melt electrospinning apparatus without an extra electricity supply.* RSC Advances, 2017. **7**(53): p. 33132-33136.
50. Shin, Y., et al., *Electrospinning: A whipping fluid jet generates submicron polymer fibers.* Applied physics letters, 2001. **78**(8): p. 1149-1151.
51. Zhou, H., T.B. Green, and Y.L. Joo, *The thermal effects on electrospinning of polylactic acid melts.* Polymer, 2006. **47**(21): p. 7497-7505.
52. Nazari, T. and H. Garmabi, *The effects of processing parameters on the morphology of PLA/PEG melt electrospun fibers.* Polymer International, 2018. **67**(2): p. 178-188.
53. Taylor, G.I., *Electrically driven jets.* Proc. R. Soc. Lond. A, 1969. **313**(1515): p. 453-475.
54. Sun, D., et al., *Near-field electrospinning.* Nano letters, 2006. **6**(4): p. 839-842.
55. Di Camillo, D., et al., *Near-field electrospinning of light-emitting conjugated polymer nanofibers.* Nanoscale, 2013. **5**(23): p. 11637-11642.
56. Bisht, G.S., et al., *Controlled continuous patterning of polymeric nanofibers on three-dimensional substrates using low-voltage near-field electrospinning.* Nano letters, 2011. **11**(4): p. 1831-1837.
57. Xu, J., et al. *Accuracy Improvement of Nano-fiber Deposition by Near-Field Electrospinning*. in *IWMF 9th International Workshop on Microfactories*. 2014.
58. Hochleitner, G., et al., *Fibre pulsing during melt electrospinning writing.* BioNanoMaterials, 2016. **17**(3-4): p. 159-171.

59. Lyons, J., C. Li, and F. Ko, *Melt-electrospinning part I: processing parameters and geometric properties.* Polymer, 2004. **45**(22): p. 7597-7603.
60. Hochleitner, G., et al., *Melt electrospinning writing of defined scaffolds using polylactide-poly (ethylene glycol) blends with 45S5 bioactive glass particles.* Materials Letters, 2017. **205**: p. 257-260.
61. Larrondo, L. and R. St. John Manley, *Electrostatic fiber spinning from polymer melts. I. Experimental observations on fiber formation and properties.* Journal of Polymer Science: Polymer Physics Edition, 1981. **19**(6): p. 909-920.
62. Bubakir, M.M., et al., *Advances in Melt Electrospinning.* 2018.
63. Fang, J., et al., *Needleless melt-electrospinning of polypropylene nanofibres.* Journal of nanomaterials, 2012. **2012**: p. 16.
64. Detta, N., et al., *Melt electrospinning of polycaprolactone and its blends with poly (ethylene glycol).* Polymer international, 2010. **59**(11): p. 1558-1562.
65. Brown, T.D., et al., *Melt electrospinning of poly (ε-caprolactone) scaffolds: Phenomenological observations associated with collection and direct writing.* Materials Science and Engineering: C, 2014. **45**: p. 698-708.
66. Deng, R., et al., *Melt electrospinning of low‐density polyethylene having a low‐melt flow index.* Journal of Applied Polymer Science, 2009. **114**(1): p. 166-175.
67. Hochleitner, G., et al., *High definition fibrous poly (2-ethyl-2-oxazoline) scaffolds through melt electrospinning writing.* Polymer, 2014. **55**(20): p. 5017-5023.
68. Brown, T.D., et al., *Design and fabrication of tubular scaffolds via direct writing in a melt electrospinning mode.* Biointerphases, 2012. **7**(1-4): p. 1-16.
69. Dalton, P.D., et al., *Direct in vitro electrospinning with polymer melts.* Biomacromolecules, 2006. **7**(3): p. 686-690.
70. Blount, M.J. and J.R. Lister, *The asymptotic structure of a slender dragged viscous thread.* Journal of Fluid Mechanics, 2011. **674**: p. 489-521.
71. Chiu-Webster, S. and J. Lister, *The fall of a viscous thread onto a moving surface: a 'fluid-mechanical sewing machine'.* Journal of Fluid Mechanics, 2006. **569**: p. 89-111.
72. HUTMACHER, D.W., *Design and fabrication of scaffolds via melt electrospinning for applications in tissue engineering.* Electrospinning: Principles, Practice and Possibilities, 2015: p. 100.
73. Hochleitner, G., et al., *Melt electrowriting below the critical translation speed to fabricate crimped elastomer scaffolds with non-linear extension behaviour mimicking that of ligaments and tendons.* Acta Biomaterialia, 2018.
74. Groll, J., et al., *Biofabrication: reappraising the definition of an evolving field.* Biofabrication, 2016. **8**(1): p. 013001.
75. Anderson, J.M., A. Rodriguez, and D.T. Chang. *Foreign body reaction to biomaterials*. in *Seminars in immunology*. 2008. Elsevier.
76. Dondossola, E., et al., *Examination of the foreign body response to biomaterials by nonlinear intravital microscopy.* Nature biomedical engineering, 2017. **1**(1): p. 0007.
77. Jones, K.S. *Effects of biomaterial-induced inflammation on fibrosis and rejection*. in *Seminars in immunology*. 2008. Elsevier.
78. Sternberg, K., et al., *Implant-associated local drug delivery systems based on biodegradable polymers: customized designs for different medical applications.* Biomedizinische Technik/Biomedical Engineering, 2013. **58**(5): p. 417-427.
79. Malikmammadov, E., et al., *PCL and PCL-based materials in biomedical applications.* Journal of Biomaterials Science, Polymer Edition, 2018. **29**(7-9): p. 863-893.
80. Klosterhoff, B.S., et al., *Implantable sensors for regenerative medicine.* Journal of biomechanical engineering, 2017. **139**(2): p. 021009.
81. Chung, J.H., et al., *3D hybrid printing platform for auricular cartilage reconstruction.* 2020. **6**(3): p. 035003.
82. Chung, J.H., et al., *A bioprinting printing approach to regenerate cartilage for microtia treatment.* 2018. **12**: p. e00031.
83. Amini, A.R., J.S. Wallace, and S.P. Nukavarapu, *Short-term and long-term effects of orthopedic biodegradable implants.* Journal of long-term effects of medical implants, 2011. **21**(2).
84. Azimi, B., et al., *Poly (ε-caprolactone) fiber: an overview.* J Eng Fibers Fabr, 2014. **9**(3): p. 74.
85. Labet, M. and W. Thielemans, *Synthesis of polycaprolactone: a review.* Chemical Society Reviews, 2009. **38**(12): p. 3484-3504.
86. Woodruff, M.A. and D.W. Hutmacher, *The return of a forgotten polymer—polycaprolactone in the 21st century.* Progress in polymer science, 2010. **35**(10): p. 1217-1256.

87. Champion, J.A., A. Walker, and S. Mitragotri, *Role of particle size in phagocytosis of polymeric microspheres.* Pharmaceutical research, 2008. **25**(8): p. 1815-1821.
88. Anderson, J.M., *Biocompatibility and bioresponse to biomaterials*, in *Principles of Regenerative Medicine*. 2011, Elsevier Inc.
89. Maruotti, N., et al., *Macrophages and angiogenesis in rheumatic diseases.* Vascular cell, 2013. **5**(1): p. 11.
90. Elpek, G.Ö., *Angiogenesis and liver fibrosis.* World journal of hepatology, 2015. **7**(3): p. 377.
91. Sauter, K.A., et al., *Macrophage colony-stimulating factor (CSF1) controls monocyte production and maturation and the steady-state size of the liver in pigs.* American Journal of Physiology-Gastrointestinal and Liver Physiology, 2016. **311**(3): p. G533-G547.
92. Naebe, M. and K. Shirvanimoghaddam, *Functionally graded materials: a review of fabrication and properties.* Applied Materials Today, 2016. **5**: p. 223-245.
93. Hofmann, D.C., et al., *Compositionally graded metals: A new frontier of additive manufacturing.* Journal of Materials Research, 2014. **29**(17): p. 1899-1910.
94. Mahamood, R.M. and E.T. Akinlabi, *Types of functionally graded materials and their areas of application*, in *Functionally Graded Materials*. 2017, Springer. p. 9-21.
95. Gilbert, C., et al., *Digital Engineering of Bio-Adaptable Dental Implants*, in *Implant Dentistry-A Rapidly Evolving Practice*. 2011, InTech.
96. Taylor, A.C., et al., *System and process development for coaxial extrusion in fused deposition modelling.* Rapid Prototyping Journal, 2017. **23**(3): p. 543-550.
97. Cornock, R., et al., *Coaxial additive manufacture of biomaterial composite scaffolds for tissue engineering.* Biofabrication, 2014. **6**(2): p. 025002.
98. Chen, H., et al., *Nanowire-in-microtube structured core/shell fibers via multifluidic coaxial electrospinning.* Langmuir, 2010. **26**(13): p. 11291-11296.
99. McCann, J.T., M. Marquez, and Y. Xia, *Melt coaxial electrospinning: a versatile method for the encapsulation of solid materials and fabrication of phase change nanofibers.* Nano letters, 2006. **6**(12): p. 2868-2872.
100. Murphy, J.P., et al., *Fabrication of optically active fiber mats via melt electrospinning.* MRS Communications, 2018. **8**(3): p. 1098-1103.
101. Fujii, T., Y. Mizutani, and K. Nakane, *Melt‐electrospun fibers obtained from polypropylene/poly (ethylene‐co‐vinyl alcohol)/polypropylene three‐layer films.* Journal of Applied Polymer Science, 2018. **135**(25): p. 46393.
102. Lee, J.K., et al., *Manufacturing and characterization of encapsulated microfibers with different molecular weight poly (ε-caprolactone)(PCL) resins using a melt electrospinning technique.* Materials Research Express, 2016. **3**(2): p. 025301.
103. Eberle, F., *Design of a Melt Electrowriting Printer containing an Additively Manufactured Metal Coaxial Nozzle.* 2018(unpublished master's thesis).
104. Huang, Z.M., et al., *Encapsulating drugs in biodegradable ultrafine fibers through co‐axial electrospinning.* Journal of Biomedical Materials Research Part A: An Official Journal of The Society for Biomaterials, The Japanese Society for Biomaterials, and The Australian Society for Biomaterials and the Korean Society for Biomaterials, 2006. **77**(1): p. 169-179.
105. Fultz, B. and J.M. Howe, *Transmission electron microscopy and diffractometry of materials*. 2012: Springer Science & Business Media.
106. Li, D. and Y. Xia, *Direct fabrication of composite and ceramic hollow nanofibers by electrospinning.* Nano letters, 2004. **4**(5): p. 933-938.
107. Schiestel, T., et al., *Hollow fibre perovskite membranes for oxygen separation.* Journal of Membrane Science, 2005. **258**(1-2): p. 1-4.
108. Kling, S. and T. Czigany, *A comparative analysis of hollow and solid glass fibers.* Textile research journal, 2013. **83**(16): p. 1764-1772.
109. Khoddami, A., C. Carr, and R. Gong, *Effect of hollow polyester fibres on mechanical properties of knitted wool/polyester fabrics.* Fibers and Polymers, 2009. **10**(4): p. 452-460.
110. Cheung, T.W. and L. Li, *A review of hollow fibers in application-based learning: from textiles to medical.* Textile Research Journal, 2017: p. 0040517517741164.
111. Diban, N. and D. Stamatialis, *Polymeric hollow fiber membranes for bioartificial organs and tissue engineering applications.* Journal of Chemical Technology & Biotechnology, 2014. **89**(5): p. 633-643.
112. Whitesides, G.M., *The origins and the future of microfluidics.* Nature, 2006. **442**(7101): p. 368.
113. Bhaskar, S. and J. Lahann, *Microstructured materials based on multicompartmental fibers.* Journal of the American Chemical Society, 2009. **131**(19): p. 6650-6651.

114. Chen, G., et al., *Structure-tunable Janus fibers fabricated using spinnerets with varying port angles.* Chemical Communications, 2015. **51**(22): p. 4623-4626.
115. Yu, D.-G., et al., *High-quality Janus nanofibers prepared using three-fluid electrospinning.* Chemical Communications, 2017. **53**(33): p. 4542-4545.
116. Jeong, B. and A. Gutowska, *Lessons from nature: stimuli-responsive polymers and their biomedical applications.* Trends in biotechnology, 2002. **20**(7): p. 305-311.
117. Ionov, L., et al., *Reversibly Actuating Solid Janus Polymeric Fibers.* ACS applied materials & interfaces, 2016. **9**(5): p. 4873-4881.
118. ZABER. *(Legacy) A-LSQ150B-E01: Motorized linear stage, integrated motor encoder and controller, 150 mm travel, medium resolution, medium speed* 23.08.2020]; Available from: https://www.zaber.com/products/linear-stages/A-LSQ-E/details/A-LSQ150B-E01.
119. Nagle, A.R., et al., *A direct 3D suspension near-field electrospinning technique for the fabrication of polymer nanoarrays.* 2019. **30**(19): p. 195301.
120. ThermoFisher. *Lipophilic Tracers - DiI, DiO, DiD, DiA, and DiR*. 2008 13.06.2018]; Available from: https://assets.thermofisher.com/TFS-Assets/LSG/manuals/mp00282.pdf.
121. Sabnis, R.W., *Handbook of biological dyes and stains: synthesis and industrial applications*. 2010: John Wiley & Sons.
122. Hutson, L.D., D.S. Campbell, and C.-B. Chien, *Analyzing axon guidance in the zebrafish retinotectal system*, in *Methods in cell biology*. 2004, Elsevier. p. 13-35.
123. Elouahabi, A., et al., *Calorimetry of cationic liposome–DNA complex and intracellular visualization of the complexes*, in *Methods in enzymology*. 2003, Elsevier. p. 312-332.
124. Kumar, C.V., *Nanoarmoring of Enzymes: Rational Design of Polymer-wrapped Enzymes*. Vol. 590. 2017: Academic Press.
125. SigmaAldrich. *Rhodamine B*. 22.08.2018]; Available from: https://www.sigmaaldrich.com/catalog/product/sigma/83689?lang=en&region=AU.
126. Prausnitz, J.M., R.N. Lichtenthaler, and E.G. de Azevedo, *Molecular thermodynamics of fluid-phase equilibria*. 1998: Pearson Education.
127. Beyler, C.L. and M.M. Hirschler, *Thermal decomposition of polymers*. SFPE handbook of fire protection engineering. Vol. 2. 2002. 111-131.
128. Diaspro, A., *Nanoscopy and multidimensional optical fluorescence microscopy*. 2010: Chapman and Hall/CRC.
129. Zhang, H., N. Ong, and Y. Lam, *Mold surface roughness effects on cavity filling of polymer melt in micro injection molding.* The International Journal of Advanced Manufacturing Technology, 2008. **37**(11-12): p. 1105-1112.
130. Wallace, W., L.H. Schaefer, and J. Swedlow, *A workingperson's guide to deconvolution in light microscopy.* Biotechniques, 2001. **31**(5): p. 1076-1097.
131. Marín, Á.G. and D. Lohse, *Building water bridges in air: Electrohydrodynamics of the floating water bridge.* Phys. Fluids, 2010. **22**(12): p. 122104.
132. Hochleitner, G., et al., *Melt Electrowriting of Thermoplastic Elastomers.* Macromolecular rapid communications, 2018: p. 1800055.
133. Mandal, N.R., *Aluminium welding*. 2001: Woodhead publishing.
134. Zalba, B., et al., *Review on thermal energy storage with phase change: materials, heat transfer analysis and applications.* Applied thermal engineering, 2003. **23**(3): p. 251-283.
135. Pitt, C., et al., *Aliphatic polyesters. I. The degradation of poly (ϵ‐caprolactone) in vivo.* J. Appl. Polym. Sci., 1981. **26**(11): p. 3779-3787.

Appendix A

Supplementary pictures and data for the uniaxial MEW setup

- MEW device

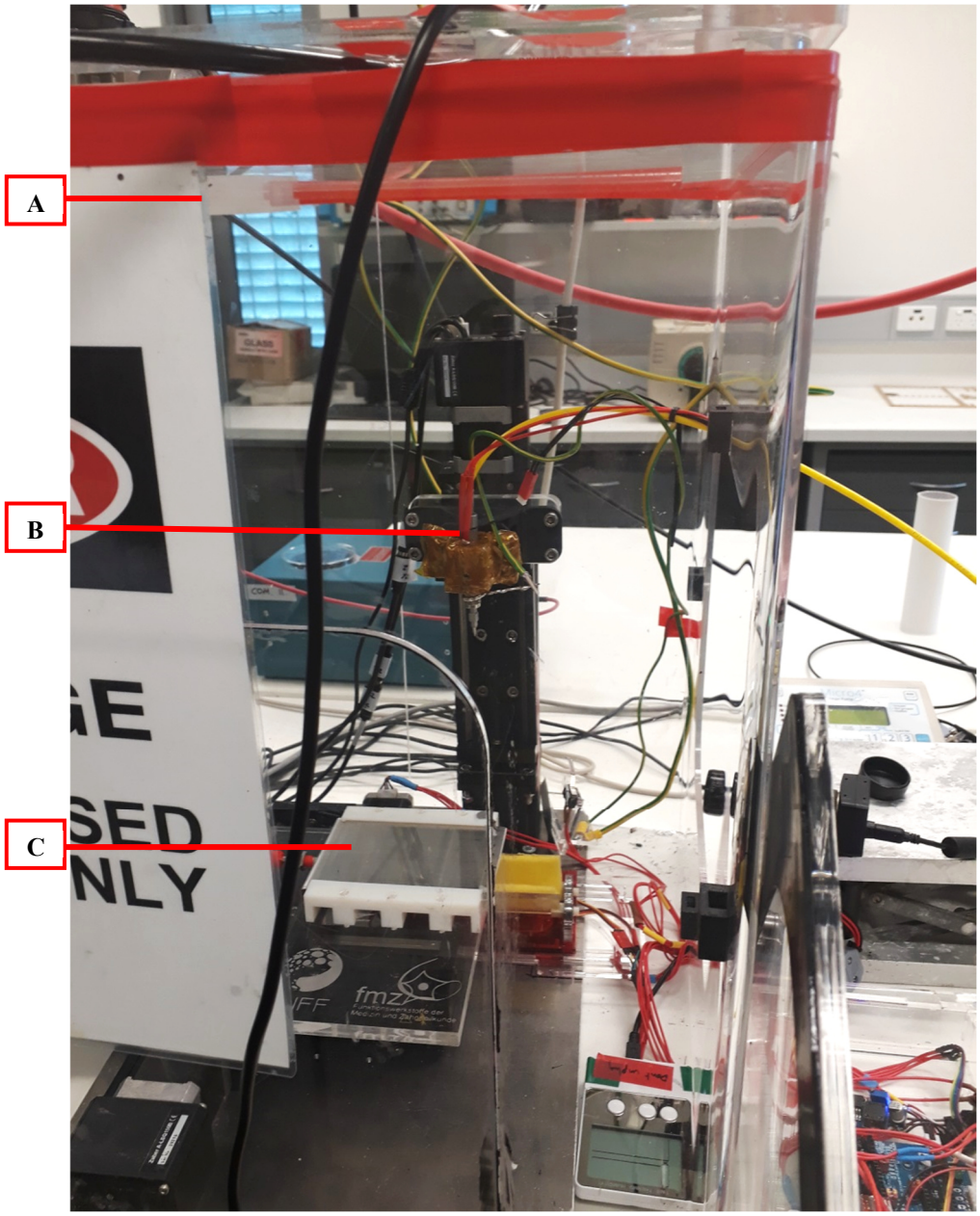

Figure 53: *Assembled MEW device with plexiglass box (A), tool head (B) and collector (C).*

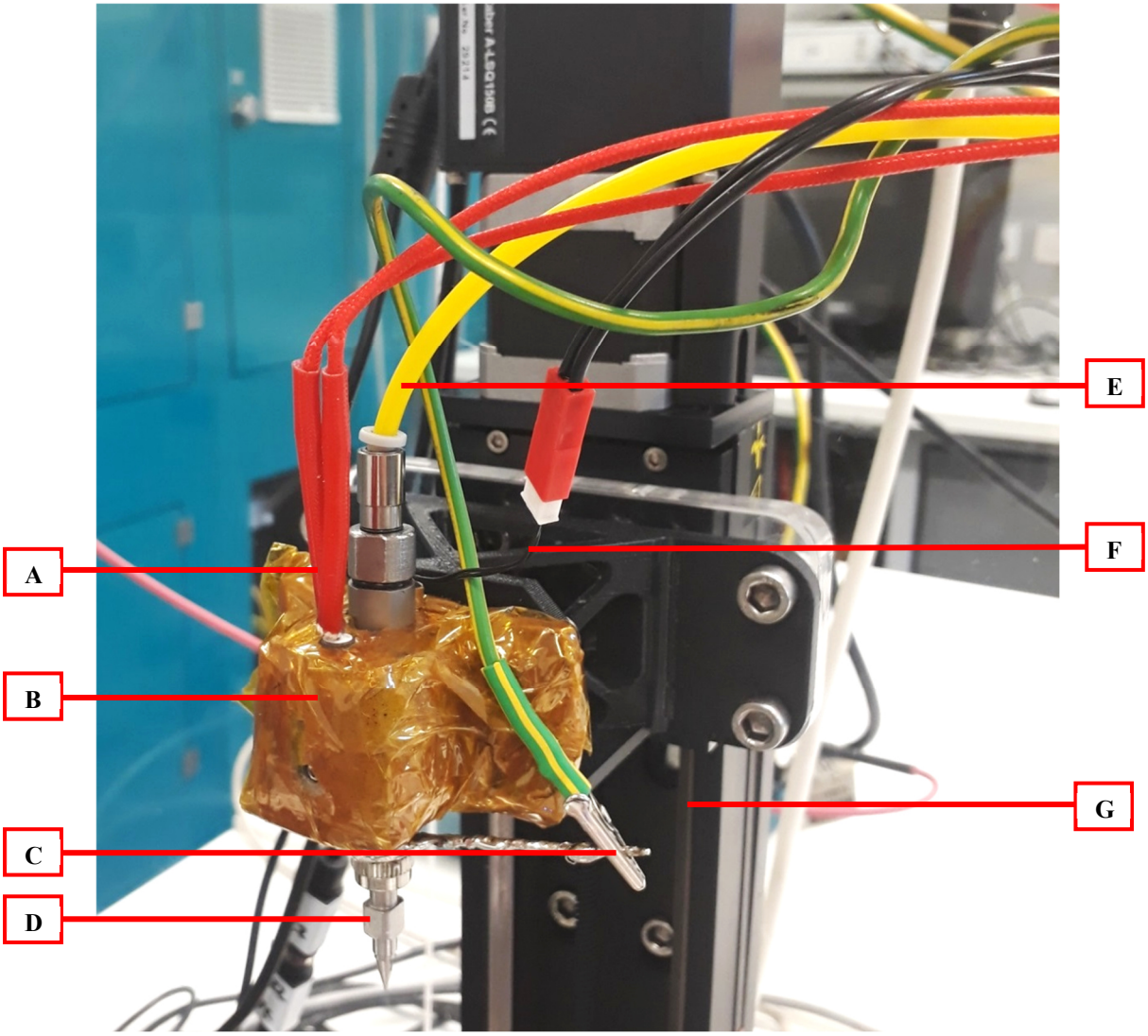

Figure 54: *Tool head with heating element (A), heating block (B), grounding (C), nozzle connected to syringe (D, the upper part of the syringe is usually covered with a Calcium Magnesium Silicate Sheet), air pressure supply (E), temperature sensor (F) and stage Z-axis (G).*

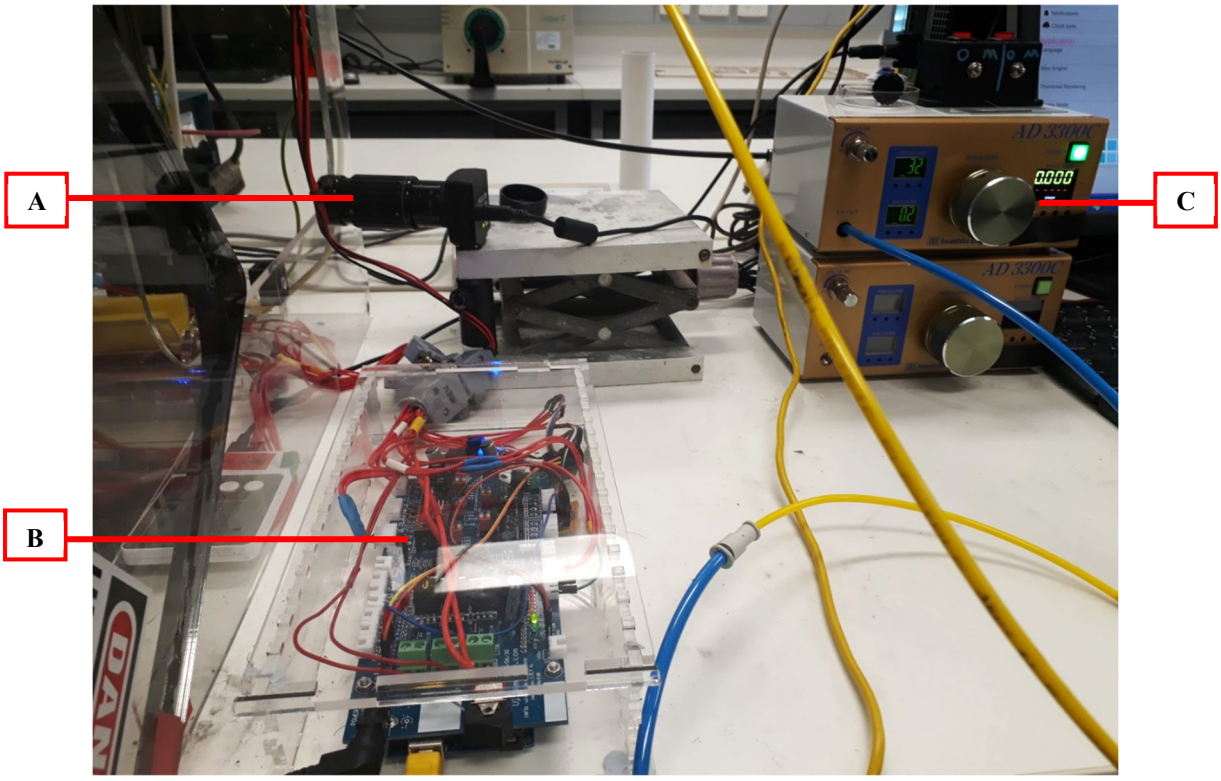

Figure 55: *MEW device control with camera (A), board (B) and pneumatic feeding system (C).*

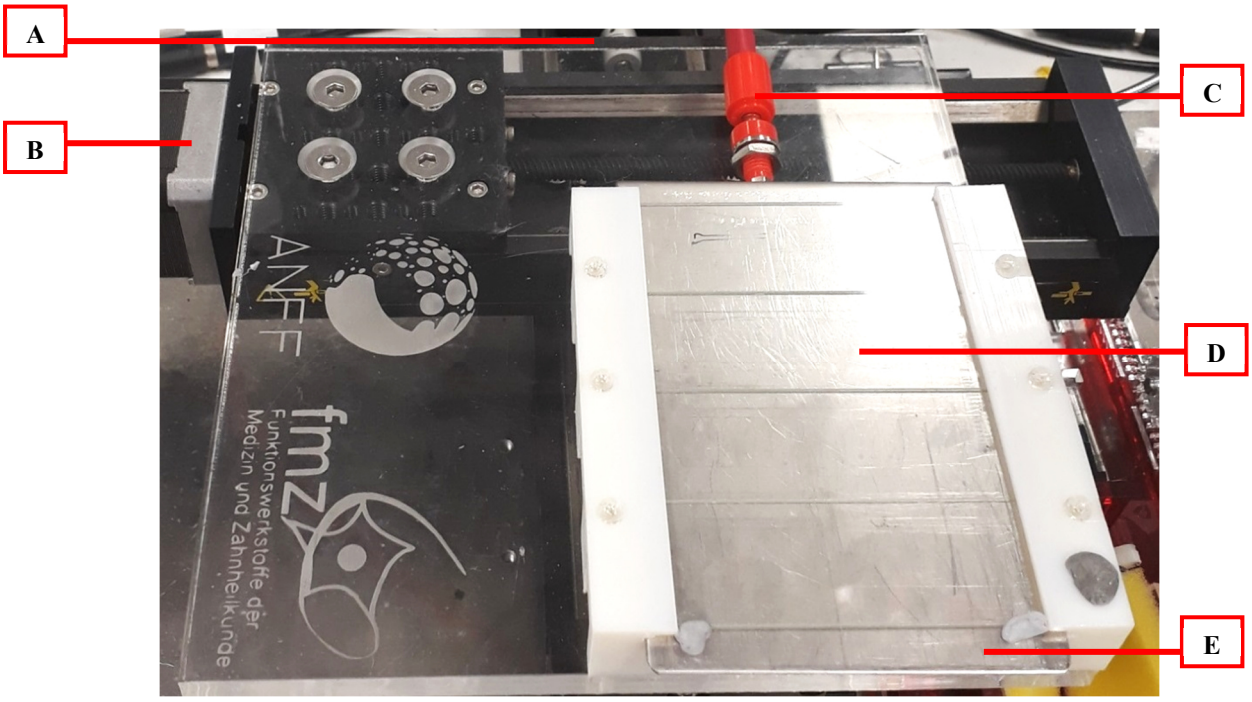

Figure 56: *Collector with stage Y-axis (A), X-axis (B), voltage supply (C), glass slides (D) and metal plate (E).*

- G-Code generation

	A	B	C	D	E	F	G	H	I	J	K	L
1	G code generator for MEW printer					Y span	78.00					
2						X span	57.00					
3		Origin				Step size	0.75	mm				
4		X	Y			ymin	72.00	mm				
5		40.00	150.00			Xmin	97.00			G Code		
6												
7	Vertical lines	40.00	150.00			Z Working	135.00			G0 F5 X40 Y150 Z135		
8	Vertical lines	95.00	150.00							G0 F5 X95 Y150 Z135		
9	Vertical lines	95.00	149.25							G0 F5 X95 Y149.25 Z135		
10	Vertical lines	40.00	149.25							G0 F5 X40 Y149.25 Z135		
11	Vertical lines	40.00	148.50			Do not change				G0 F5 X40 Y148.5 Z135		
12	Vertical lines	95.00	148.50			Change				G0 F5 X95 Y148.5 Z135		
13	Vertical lines	95.00	147.75			Auto Updating				G0 F5 X95 Y147.75 Z135		
14	Vertical lines	40.00	147.75							G0 F5 X40 Y147.75 Z135		
15	Vertical lines	40.00	147.00							G0 F5 X40 Y147 Z135		
16	Vertical lines	95.00	147.00			0.75				G0 F5 X95 Y147 Z135		
17	Vertical lines	95.00	146.25							G0 F5 X95 Y146.25 Z135		
18	Vertical lines	40.00	146.25			128.00				G0 F5 X40 Y146.25 Z135		
19	Vertical lines	40.00	145.50		Working areas per slide					G0 F5 X40 Y145.5 Z135		
20	Vertical lines	95.00	145.50			X min	X max	Y min	Y max	G0 F5 X95 Y145.5 Z135		
21	Vertical lines	95.00	144.75		Slide 1	53.00	110.00	138.00	150.00	G0 F5 X95 Y144.75 Z135		
22	Vertical lines	40.00	144.75		Slide 2	53.00	110.00	110.00	130.00	G0 F5 X40 Y144.75 Z135		
23	Vertical lines	40.00	144.00		Slide 3	53.00	110.00	85.00	105.00	G0 F5 X40 Y144 Z135		
24	Vertical lines	95.00	144.00		Slide 4	53.00	110.00	60.00	80.00	G0 F5 X95 Y144 Z135		
25	Vertical lines	95.00	143.25							G0 F5 X95 Y143.25 Z135		
26	Vertical lines	40.00	143.25							G0 F5 X40 Y143.25 Z135		
27	Vertical lines	40.00	142.50			Speeds		mm/s		G0 F5 X40 Y142.5 Z135		
28	Vertical lines	95.00	142.50			Slide Calibration		5.00		G0 F5 X95 Y142.5 Z135		
29	Vertical lines	95.00	141.75			Slide 1		10.00		G0 F5 X95 Y141.75 Z135		
30	Vertical lines	40.00	141.75			Slide 2		15.00		G0 F5 X40 Y141.75 Z135		
31	Vertical lines	40.00	141.00			Slide 3		20.00		G0 F5 X40 Y141 Z135		
32	Vertical lines	95.00	141.00							G0 F5 X95 Y141 Z135		
33	Vertical lines	95.00	140.25							G0 F5 X95 Y140.25 Z135		
34	Vertical lines	40.00	140.25							G0 F5 X40 Y140.25 Z135		
35	Vertical lines	40.00	139.50							G0 F5 X40 Y139.5 Z135		
36	Vertical lines	95.00	139.50							G0 F5 X95 Y139.5 Z135		
37	Vertical lines	95.00	138.75							G0 F5 X95 Y138.75 Z135		
38	Vertical lines	40.00	138.75							G0 F5 X40 Y138.75 Z135		
39	Vertical lines	40.00	138.00							G0 F5 X40 Y138 Z135		
40	Horizontal Lines	95.00	138.00							G0 F5 X95 Y138 Z135		

Figure 57: *G-Code generation for single fibres via a Microsoft Excel spreadsheet with adjustable Z-height (red) and collector speeds (green) for all 4 glass slides.*

Appendix B

Supplementary pictures and data for the coaxial MEW setup

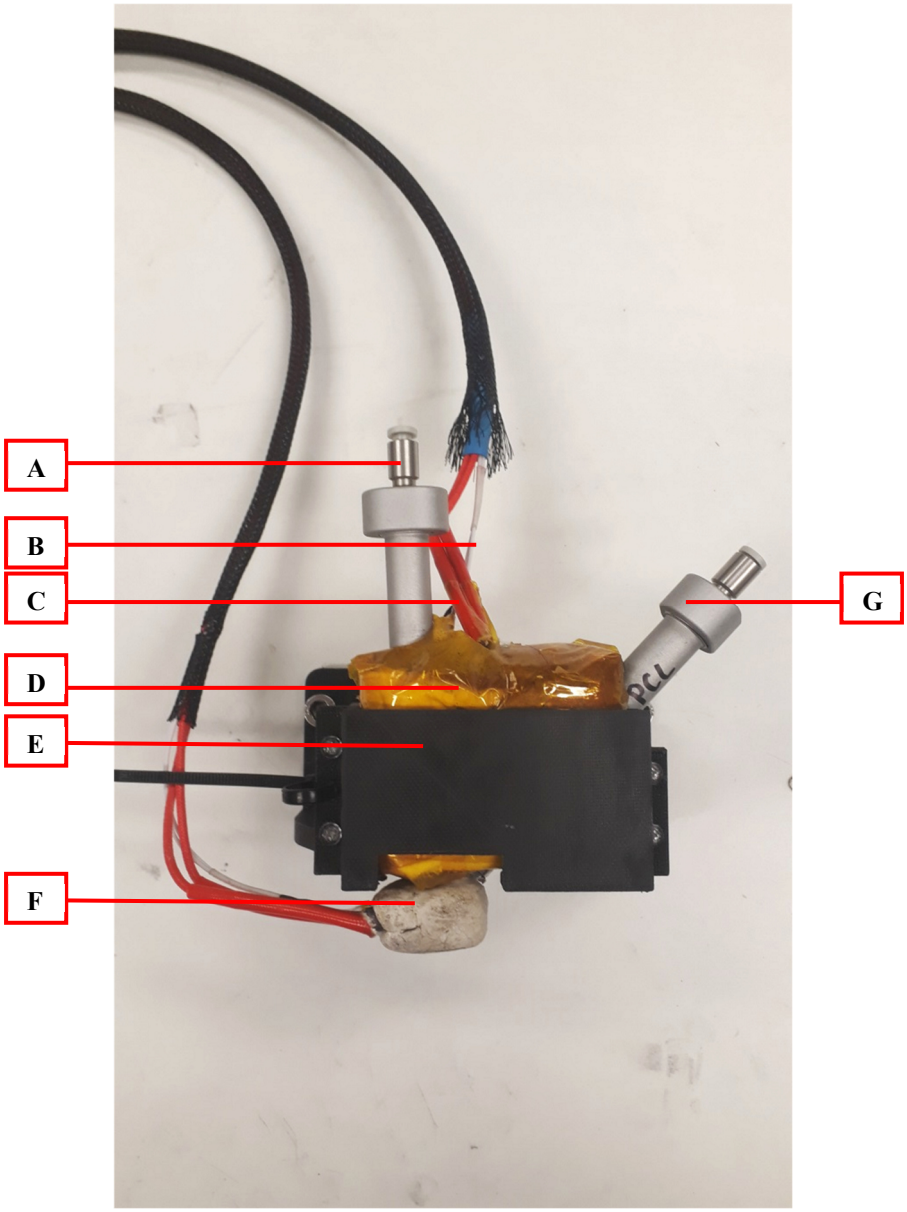

Figure 58: *Assembly of the coaxial tool head with pneumatically controlled core syringe (A), temperature sensor and heater (B and C, respectively) for the heating block (D) that is wrapped in Kapton tape and rockwool and inserted in a bracket made of Onyx (E), the grounded and heated coaxial nozzle that is embedded in fire cement (F), as well as the shell syringe (G).*

- Heater and nozzle embedding in fireproof cement

After the initial overshooting, the heating of the nozzle was found to be stable and vary between 78 and 82 °C as presented in Section 4.3.2.5. To achieve this steadiness, the embedding process had to be adapted, since earlier investigations showed a constant overshooting of the nozzle temperature in a range of 15 ºC. Initially, a dummy heating element was placed into the wet cement to spare a cavity for the actual heating element during the drying process. This way the hole was narrow enough to prevent any air flow during the heating that might cause a thermal insulation of the heater, forcing it to heat up to higher temperatures. Yet, this also resulted in having a thin cement wall between the heater and the nozzle. For the study presented in Section 4.3, the cavity for the heating element was hand-drilled instead after the cement has been dried completely, which led to a removal of parts of the cement that covered the nozzle; this way, a physical contact between the heater and the metal was enabled and therefore resulted in a more consistent heating. Also, the cavity for the temperature sensor was hand-drilled far enough to allow the sensor to touch the nozzle. The cavities as well as the assembly can be seen in Figure 59.

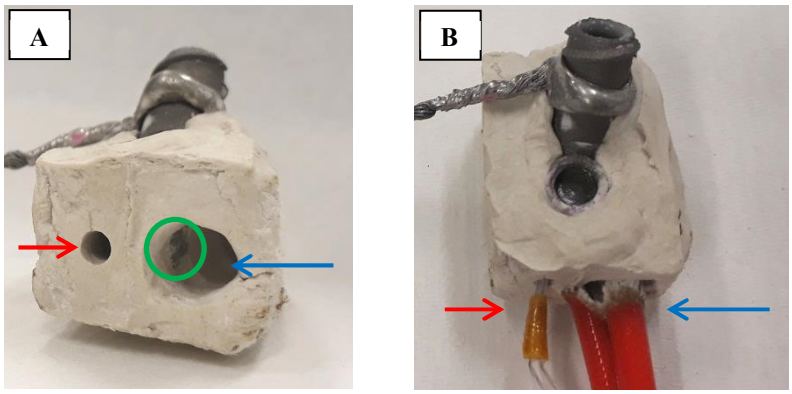

Figure 59: *The coaxial nozzle embedded in fire cement with the cavities for the heat sensor (red arrow), the heating element (blue arrow) and the part of the nozzle that is exposed to the heater (green circle) (A) and a demonstration of the heater and sensor positions in relation to the nozzle after placing them into the cement (B).*

It is evident that this hand-crafted embedding process is not reproducible; thus, the temperature profiles will vary for every new embedding of the nozzle in this prototyping coaxial system.

- Measured fibre dimensions

Table 5: *Fibre dimensions that belong to Figure 38, variation of the core pressure pc, F1-15 describe 15 different fibres taken from three independent printing processes.*

pc [kPa]	F1 [µm]	F2 [µm]	F3 [µm]	F4 [µm]	F5 [µm]	F6 [µm]	F7 [µm]	F8 [µm]	F9 [µm]
100	38.24	35.59	38.29	39.17	39.22	36.64	48.06	37.67	41.84
50	41.84	42.73	43.62	40.95	46.29	38.31	36.54	40.09	34.76
20	39.2	38.31	39.2	37.43	37.55	35.7	34.72	38.27	36.49
0	35.6	36.49	32.93	33.82	34.71	31.15	34.71	32.04	36.5
pc [kPa]	**F10 [µm]**	**F11 [µm]**	**F12 [µm]**	**F13 [µm]**	**F14 [µm]**	**F15 [µm]**	**Average [µm]**	**Standard deviation [µm]**	
100	33.81	35.65	45.39	37.98	34.28	35.76	38.506	4.032009	
50	39.2	40.1	38.62	40.09	36.38	38.61	39.87533	3.067865	
20	40.98	37.12	37.87	35.64	37.12	34.9	37.36667	1.640705	
0	39.2	35.65	34.19	31.93	31.19	31.93	34.136	2.319362	

Table 6: *Fibre dimensions that belong to Figure 39, variation of the shell pressure ps, F1-15 describe 15 different fibres taken from three independent printing processes.*

ps [kPa]	F1 [µm]	F2 [µm]	F3 [µm]	F4 [µm]	F5 [µm]	F6 [µm]	F7 [µm]	F8 [µm]	F9 [µm]
50	33.04	38.37	36.59	41.92	59.64	62.31	51.63	39.17	36.5
30	38.24	35.59	38.29	39.17	39.22	36.64	48.06	37.67	41.84
10	34.76	35.65	31.2	30.31	36.54	32.98	33.87	29.42	31.17
ps [kPa]	**F10 [µm]**	**F11 [µm]**	**F12 [µm]**	**F13 [µm]**	**F14 [µm]**	**F15 [µm]**	**Average [µm]**	**Standard deviation [µm]**	
50	41.84	42.33	42.38	45.31	50.51	43.83	44.358	8.68552	
30	33.81	35.65	45.39	37.98	34.28	35.76	38.506	4.032009	
10	25.83	31.19	28.97	31.19	30.45	31.19	31.648	2.860711	

Table 7: *Fibre dimensions that belong to Figure 34, variation of the collector speed for PCL containing Rhodamine B in the core syringe, F1-15 describe 15 different fibres taken from three independent printing processes.*

v [mm/s]	F1 [µm]	F2 [µm]	F3 [µm]	F4 [µm]	F5 [µm]	F6 [µm]	F7 [µm]	F8 [µm]	F9 [µm]
5	51.59	44.47	37.37	57.83	46.28	57.84	51.65	57.92	51.7
10	38.24	35.59	38.29	39.17	39.22	36.64	48.06	37.67	41.84
20	23.12	23.19	24.08	26.81	27.63	32.07	34.7	40.06	33.9
30	38.29	28.47	36.5	20.48	25	30.29	29.4	25.85	25.8
40	22.24	18.68	19.57	22.31	24.97	27.59	21.36	18.91	25.81

v [mm/s]	F10 [µm]	F11 [µm]	F12 [µm]	F13 [µm]	F14 [µm]	F15 [µm]	Average [µm]	Standard deviation [µm]
5	46.28	42.38	42.55	48.28	38.61	53.5	48.55	6.86201
10	33.81	35.65	45.39	37.98	34.28	35.76	38.506	4.032009
20	26.74	25.24	23.77	21.54	25.42	27.51	27.71867	5.407052
30	41.8	22.29	25.29	31.22	25.29	29.4	29.02467	6.168983
40	26.74	27.63	28	32.29	22.39	23.86	24.15667	4.032766

Table 8: *Fibre dimensions that belong to Figure 34, variation of the collector speed v for PCL in the core syringe, F1-15 describe 15 different fibres taken from three independent printing processes.*

v [mm/s]	F1 [µm]	F2 [µm]	F3 [µm]	F4 [µm]	F5 [µm]	F6 [µm]	F7 [µm]	F8 [µm]	F9 [µm]
5	51.62	58.76	56.1	51.65	54.32	55.21	56.98	54.32	52.59
10	42.69	43.72	43.62	40.06	39.14	40.06	40.06	40.92	38.25
20	32.91	30.25	34.7	36.48	39.13	34.69	35.58	36.47	35.58
30	26.7	26.7	24.92	21.36	22.25	22.24	23.12	24.01	23.12
40	20.46	19.57	20.46	19.57	18.68	20.46	19.65	18.76	17.81

v [mm/s]	F10 [µm]	F11 [µm]	F12 [µm]	F13 [µm]	F14 [µm]	F15 [µm]	Average [µm]	Standard deviation [µm]
5	51.7	45.29	48.26	47.52	51.99	53.48	52.65267	3.624962
10	39.14	38.67	39.41	40.9	40.86	41.74	40.616	1.702522
20	36.48	28.96	33.41	34.15	34.9	31.93	34.37467	2.600681
30	24.01	22.27	20.05	26.73	20.8	26	23.61867	2.207328
40	18.68	18.56	18.58	17.83	18.58	17.09	18.98267	1.024852

Appendix C

Processing EFG-loaded PCL via uniaxial MEW

Adding conductive particles such as salts to solutions is a common practice in SES in order to further accelerate the materials in the jet stream from a Taylor cone so that finer fibres can be achieved. Hence, addition of similar particles could be expected to also have a strong impact on the MEW process. Edge-functionalised graphene (EFG) is a proprietary material under investigation in the University of Wollongong. It has previously been utilised as a conductive filler material in PCL and processed through FFF. The same composite material is examined here under MEW process conditions.

The MEW minimum printing temperature for a 1 wt% EFG-loaded PCL was found to be 95 °C. This temperature value was 10 to 15 °C higher than the temperature that has been used for the melt extrusion of pure PCL with the same setup. Filler contents are known to increase the viscosity of melted polymers, so this effect had been expected. As mentioned before, lower viscosities result in finer fibre diameters. Nevertheless, temperatures above 95 °C have not been investigated for this material, on the one hand to prevent the polymer from degrading too quickly but on the other hand to not cause any excess flowing of the low viscosity PCL, leaving the EFG particles behind.

The EFG-PCL composite (approx. 1 g in chopped pellet form) was loaded into a 3 cc metal syringe and set up in the uniaxial MEW system configuration. Preliminary tests were used to identify initial system operating parameters. A 400 µm stainless steel nozzle was used. For the determination of suitable applied potential differences, a range of 1 to 5 kV was investigated. The working distance between the tip and the metal collector plate was varied between 5 mm and 2 mm. The material was heated to 95 °C and allowed to stabilise. Appearance of molten PCL at the nozzle tip under a small applied pressure (20 kPa) indicated that the material was ready for testing to begin. 1 mm thick glass slides (4x) were located side by side on top of the collector plate so that produced fibres could be collected for analysis. With an offset of 3.5 mm between the tip and the surface of the glass slides, selected to prevent electrical arcing, it was found that applied voltages below 2 kV did not draw material from the nozzle. Jetting was observed between applied voltages of 2 kV and 4 kV. At applied voltages above 4 kV it was observed that the jet would be unstable and intermittently break. For these reasons initial values of 3 kV (the midpoint in observed jetting), an offset of 3.5 mm from the glass slide surface, and zero applied pneumatic pressure due to an observed pulsing when continuously applying even small pressures, were set for initial testing of the EFG-PCL composite and a moving collector stage.

As outlined in Section 1.2.3, the critical translation speed (CTS) is a key parameter to be investigated with any material being processed through MEW and is typically in the mm/s range. To perform a CTS study and determine a specific velocity value for the CTS, the nozzle should be translating over the collector plate at incrementally fixed velocities and the resultant fibres examined for their structure and form as outlined in the introduction.

The CTS of the EFG-PCL was found to be 5 mm/s. The determination of this MEW-specific value that describes the necessary collector speed to draw straight fibres in a controlled way was further explained in Section 4.2.2. Different collector speeds above the CTS were investigated, the most uniform fibres with an average diameter of 7 µm were obtained with a collector speed of 10 mm/s. Figure 60 shows the fibres at two different magnifications.

At this point, and with the resolution of the stereo microscope used for imaging, EFG particles were not visible within the produced fibres.

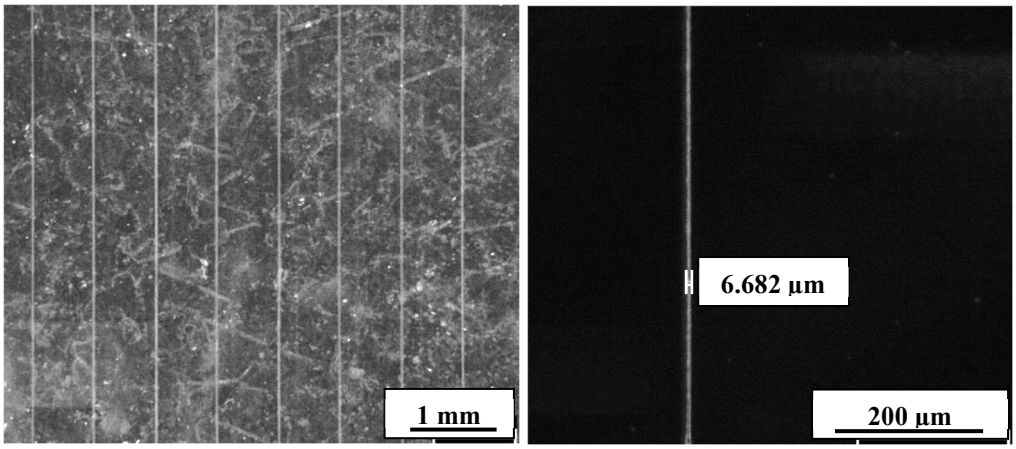

Figure 60: *EFG-PCL fibres that have been printed at 95 °C, 10 mm/s, 3 kV, 4.5 mm and 0 bar, 22 °C ambient temperature and 44% relative humidity.*

Over time, it was observed that the characteristics of the printing behaviour of the EFG-PCL would change, therefore being unstable. Closer optical analysis was performed on the material at the tip of the nozzle. It was seen that the dispersion of EFG within the PCL carrier was not homogenous as it was jetted from the nozzle. This is highlighted in Figure 61. In Figure 61 A, at the beginning of a MEW test a small number of EFG particles (indicated by the red arrow) could be seen leaving the nozzle along with the polymer. However, after an extended time of this material batch being held in the metal reservoir and after being exposed to 4 melting and cooling cycles there was a dramatic increase in the quantity of visually apparent particles within the melt, Figure 61 B.

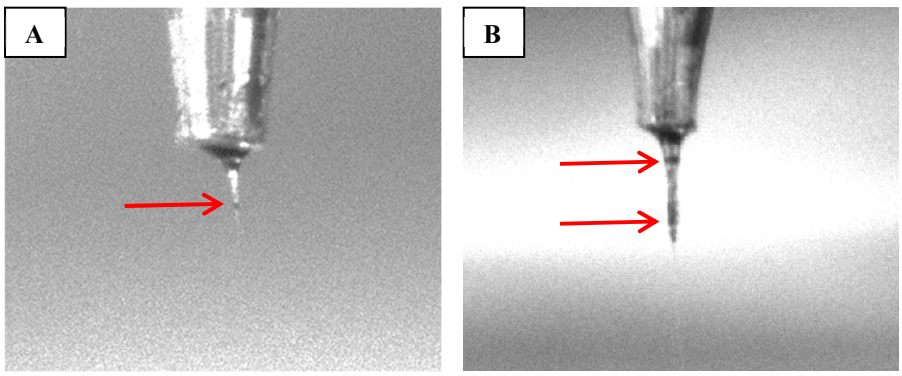

Figure 61: *The Taylor cone containing EFG particles (red arrow) a few hours after starting the material tests (A) and after multiple heating and cooling cycles of the same batch of material (B).*

It has to be assumed that in the beginning of the printing with fresh material an excess flowing of the polymer happened. The comparatively high but necessary processing temperature of 95 °C has lowered the viscosity of PCL, making it flowing out of the nozzle while carrying only few particles. Over time, the residual material contained a higher percentage of particles that visibly agglomerated and were finally deposited. These agglomerations could be observed throughout the later printing processes, leading to changes in fibre diameter and breakages of the jet, which can be seen in Figure 62.

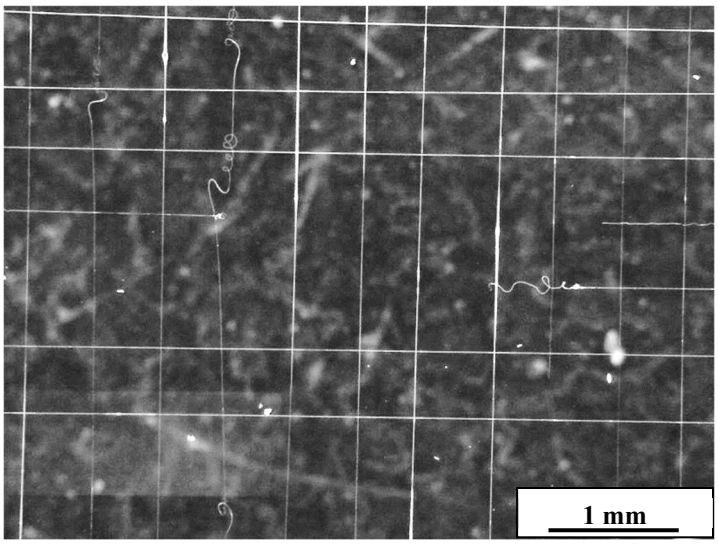

Figure 62: *Lattice structure made of EFG-PCL with agglomerates causing a change in fibre diameters and even jet breakages.*

Resistance measurements delivered no valid results for the fine fibres that have been printed with the settings described before. By trying to determine bulk filament conductivity through extrusion printing of the material at an air pressure of 230 kPa, thick fibres with outer diameters above 100 µm were accessible that contained visibly more particles as presented in Figure 63. However, there was no conductive behaviour found for these structures either.

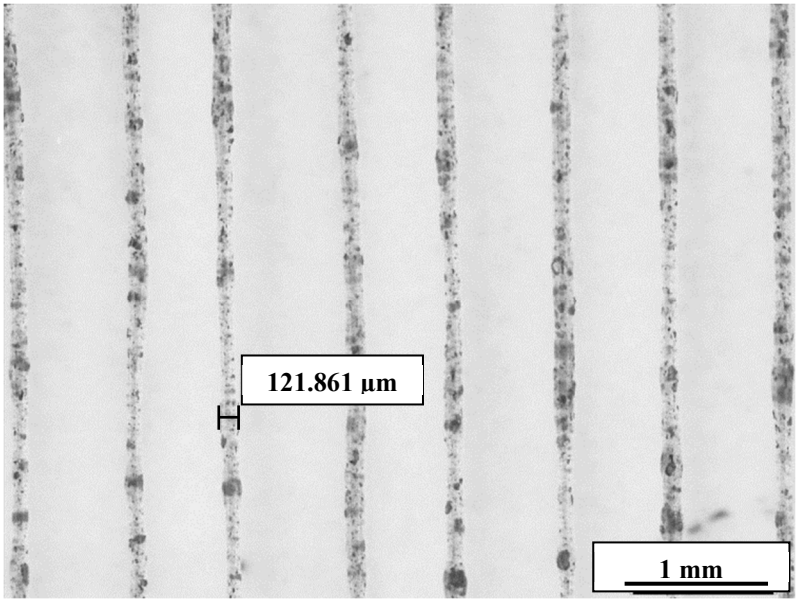

Figure 63: *Fibres made of EFG-PCL printed with a feeding pressure of 230 kPa.*

At this point the EFG-PCL composite was discounted as a candidate material for further testing within the coaxial MEW arrangement due to its lack of stability when jetting, non-homogenous and changing filler distribution, and propensity to cause blockages or discontinuations at the nozzle.

Appendix D

4th semester report conducted in Germany

PLEASE NOTE:

The following section contains confidential data of the enterprises SKZ – KFE gGmbH and Headmade Materials GmbH.

This work may only be available to the first and second reviewers and authorized members of the board of examiners. Any publication and duplication of this final thesis – even in part – is prohibited.

An inspection of this work by third parties requires the expressed permission of the author and the respective companies.